Study on Limiting Behavior of Smoldering Using Low Pressure

（低圧場を用いたくん焼の限界挙動に関する研究）

January, 2020

Doctor of Philosophy (Engineering)

Takuya Yamazaki

Toyohashi University of Technology

Abstract

Experimental study on limiting behavior of smoldering combustion, the transition to extinction or flaming from smoldering, was conducted with high reproducibility to clarify their precise mechanisms systematically. The considered ambient conditions in this study were $1.0 - 100$ kPa in absolute pressure varying oxygen concentrations within $0.20 - 1.0$ in mass fraction of oxygen. A 2-mm-rod-shaped biomass stick (incense stick) was considered as the test specimen as representative general charring fuels having bulk density and porosity similar to general wooden materials.

The smoldering behavior of the thin-rod biomass stick at low pressures and various oxygen concentrations was experimentally investigated for the vertically- and horizontally-oriented cases, aiming to examine the influence of a low-pressure environment on smoldering behaviors. In a low-pressure environment, the smoldering rates, the peak temperatures, and the thermal structures inside the biomass sticks were found to be nearly identical for both vertical and horizontal cases. This fact implies that role of the natural convection on combustion process was effectively suppressed using low pressure, suggesting that the effect of buoyancy-induced flow on the smoldering region becomes sufficiently small. In this way, the low-pressure method for examination for both extinction limit and transition to flaming from smoldering was verified.

The smoldering behavior near the extinction limit was then studied using the low-pressure

method with the thin-rod biomass stick. It was found that the extinction limits were clearly

affected by the imposed oxygen concentration. Having lower oxygen concentration below

0.4, the limit was achieved at certain smoldering rate. This limit was expected to be well-

controlled by the transport (so-called transport-controlled regime) since oxygen transport to

the smoldering region by natural convection was adequate for smoldering combustion, while

the heat losses are more effective to lead to extinction. Having higher oxygen concentration

above 0.4, on the other hand, the limit appeared at sufficiently low pressure where the

transport process is severely suppressed. This limiting behavior is equivalent to one observed

in the oxygen-limited regime, indicating that the oxygen-deficient condition limited the

oxidation reaction. The extinction limit in the oxygen-limited regime showed a strong

dependency on the imposed pressure, which is first ever observed/confirmed by this work.

The transition from downwardly (reverse) smoldering to flaming in a low-pressure

environment was investigated to determine the dominant factor in the critical condition of the

transition. The reverse smoldering progressed steadily, although the lengths of the luminous

region slowly increased with time under the conditions in which the partial pressure of

oxygen is above 30 kPa. Introducing an image processing method, it was revealed that the

luminous length at the point of transition showed strong dependency with the imposed partial

pressure of oxygen. To examine their relationship, a simple ignition model referred by

Semenov's theory was developed. It was confirmed that the predicted critical lengths when transition to flaming occurs were in good agreement with the experimental data, implying that the occurrence of the transition is mainly controlled by the heat balance between the heat release rate by oxidation reaction of the pyrolysis gases and the heat loss from the hot pyrolysis gases to the surrounding area when the concentrations of pyrolysis gases are enough to ignite.

Table of Contents

Nomenclature

Symbol	Description	Unit
A	Pre-exponential factor	1/s
b	Width	m
c	Specific heat	$J/kg \cdot K$
c_p	Specific heat at constant pressure	$J/kg \cdot K$
d	Diameter	m
d_{pm}	Mean pore size of the porous media	m
D_e	effective diffusion coefficient	m^2/s
D_{iK}	Knudsen diffusion coefficient	m^2/s
E	Activation energy	kJ/mol
g	Gravitational acceleration	m/s^2
h	Heat transfer coefficient	$W/m^2 \cdot K$
h_a	Height	m
k	Thermal conductivity	$W/m \cdot K$
K	Permeability	m^2
k_{chem}	Rate constant of a chemical reaction	
K_{Pi}	Equilibrium constant of chemical reaction of i species	-
L	Characteristic length	m
M	Molecular weight	g/mol
p	Total pressure	Pa
P_0	Ambient pressure	Pa
P_i	Partial pressure of i species	Pa
Q	Heating value	kJ/g

Q^*	Non-dimensional heat release	-
r	Radial	m
R	Universal gas constant	$J/mol\ K$
S	Surface area	m^2
T	Temperature	K
$\bar{T}$	Average temperature	K
T_o	Ambient temperature	K
u_d	Darcian velocity	m/s
u_s	Smoldering velocity	mm/s
v	Velocity	m/s
v_0	Characteristic velocity	m/s
V	Volume	m^3
X	Mole fraction	-
y	y-coordinate in cartesian coordinate system	m
Y	Mass fraction	-
z	Axial coordinate in cylindrical coordinate system	m
Z	Conversion of mass	-

Greek symbols

β	Non-dimensional activation energy	-
$\bar{\beta}$	Volume expansion ratio	$1/K$
δ	Thickness of the boundary layer	m
θ	Azimuthal coordinate	rad
	or Non dimensional temperature	or -
Λ	Non-dimensional Damkohler number	-

μ	Viscosity	$Pa \cdot s$
ρ	Density	kg/m^3
ρ_c	Averaged (volumetric) density	kg/m^3
$\bar{\rho}$	Density at mean temperature	kg/m^3
σ_{ij}	Collision diameter	Å
τ	Tortuosity	-
φ	Porosity	-
Ω	Collisional integral	-

Subscripts

a	Altitude
c	Char
g	Gas
ini	Initial
o	Oxygen
r	Radial coordinate
s	Solid
w	Wall or Wall surface
z	Axial coordinate
∞	Infinity
θ	Azimuthal coordinate

Acknowledgements

I would like to thank my advisor Prof. Yuji Nakamura at first. You took your time to discuss my thesis and make small talk anytime. You have given me opportunities on that I want to treat challenging problems. Your philosophy is always beside me.

To Prof. Tsuneyoshi Matsuoka, my mentor since I was in master's course. You are the first key person who showed what is the academic world.

To Prof. Kozo Saito, Prof. Ahamad A. Salaimeh, Prof. Nelson Akafuah, Dr. John M. Stencel and the other members, members of the Institute of Research for Technology Development (IR4TD). They warmly invited me into IR4Td and kindly supported my research project during my short-term visiting there. The project during the short-term visiting was funded by Japan Society for the Promotion of Science.

To my thesis committee, Prof. Yanada, Prof. Oguchi, and Prof. Kuwana. Your comments and advices were insightful. These comments improved my thesis. Especially, my thanks go to Prof. Kuwana, who is a coauthor in the article in which I participated as the first author. Thank you for your kind support and giving many comments through the work.

To my parents and brother and sister. If there were no help from you, I couldn't achieve anything in doctoral course. Your support makes me encouraged to go the way I am.

To Kirara. You have warmly supported me with your words of encouragement throughout this entire process.

Chapter 1

1. Introduction

1.1. Fires

Fire has provided a rich life for us as a source of heat and power. However, a fire can become life-threatening everywhere such as homes, offices, vehicles, and forests [1]. The words "a fire" and "fire" have physical ambiguity since fire is a process and can take many forms, of which involve a chemical reaction between combustible substance and oxygen [2]. According to the major dictionaries, the definition of "fire" can be found as follows:

- *Fire - "A process in which substances combine chemically with oxygen from the air and typically give out bright light, heat, and smoke; combustion or burning." –Oxford dictionary* [3]

- *A fire - "A destructive burning of something" –Oxford dictionary* [3]

- *"the flames, light and heat, and often smoke, that are produced when something burns", "flames that are out of control and destroy buildings, trees, etc." – Oxford Advanced Learner's Dictionary* [4]

- *"(material that is in) the state of burning that produces flames that send out heat and light, and might produce smoke:" – Cambridge dictionary* [5]

Based on these conventional descriptions, we define that a fire is a process producing heat

and light emission, and being out of control and destroys buildings, trees, etc.

Fires are one of the causes of death and kill over 120,000 people in the world. Figure

1.1 shows the comparison with the mortality estimates of road injuries, the number of

deaths by fire, heat, and hot substances. The death threat of fires is one-tenth of that of

road injuries. However, fires possess not only a threat to kill and injure people, but also

hazards to damage and destroy living properties (e.g. houses, buildings) and natural

resources, which causes negative economic and environmental impacts.
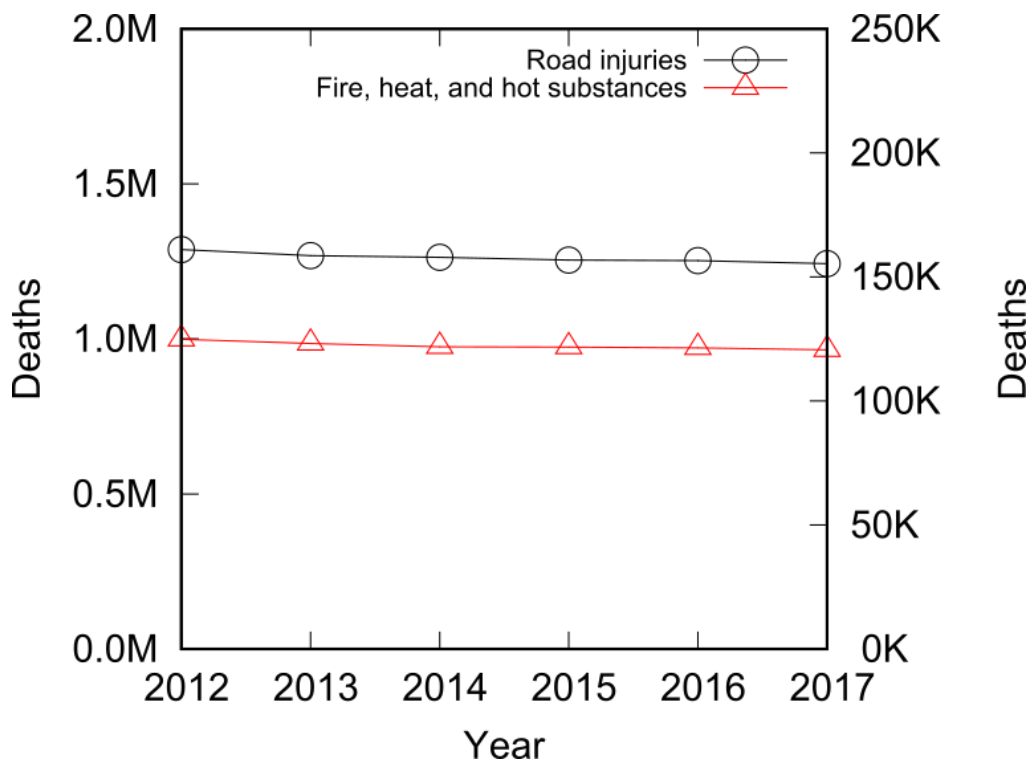
Fig.1.1. Mortality estimates of road injuries and fire, heat, and hot substances in the world [6].

Table 1.1 shows the comparison of the economic impact between fires and car crashes in the U.S. These costs include total property damage cost and present and future medical costs due to injuries. The economic loss by fires is larger than that of motor vehicle crashes, even though the number of motor vehicle crashes is 10 times larger than fires as a large number of the mortality estimates of road injuries are shown in Fig.1.1. This is because a scale of each fire is larger than a motor vehicle crash.

Table 1.1. Comparison of economic impact between fires and car crashes in the U.S.

Cause	Total cost in billion U.S. dollars	Reference
Fire in 2014	328.5	[7]
Motor vehicle crashes in 2010	242.0	[8]

Fire causes in Japan and United States are shown in Fig.1.2. For fire causes in Japan, cigarette is the 1st cause of fires, bonfire is the 2nd cause, and cooking is the 3rd cause. For fire causes in the U.S., cooking is the 1st cause of fires, heating is the 2nd cause, and unintentional carelessness is the 3rd cause. In fire causes, one of the important processes during a fire is a flameless-burning; this is called "smoldering". Smoldering is slow, low temperature burning (solid oxidation) process without flame. A feature of smoldering (which will be explained in detail later) is smoky to emit unburned fuel matters into a

firing atmosphere. The fire's causes related to smoldering fires are smoking, bonfire, open

burning and heating.
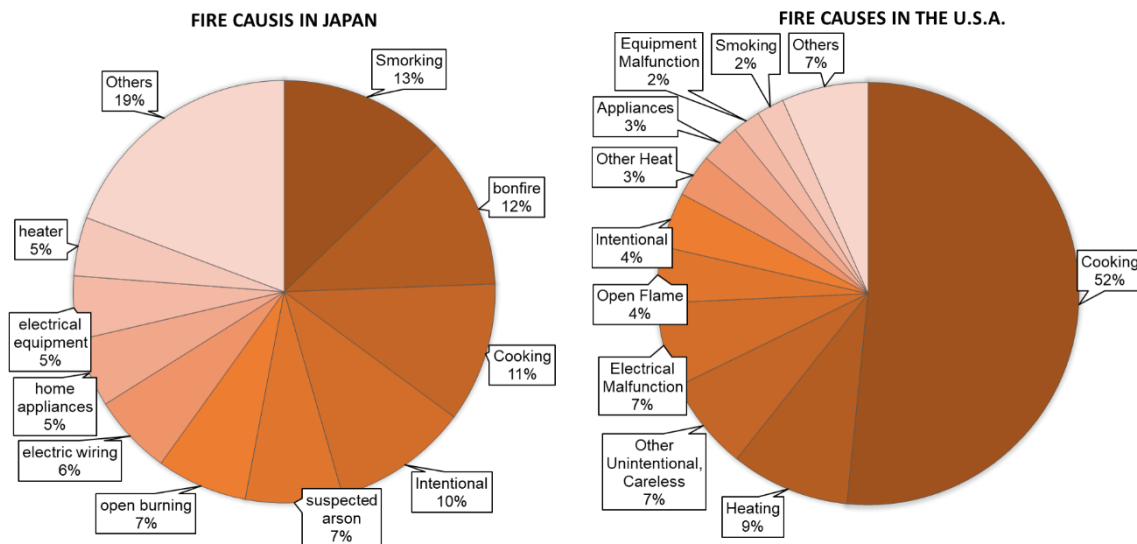
Fig.1.2. Fire causes in Japan [1] and United States [9].

There are three types of fires in fire protection shown in Fig.1.3. One is structural fires

that happen in buildings, enclosed structures, vehicle vessels or like properties [10]

(Fig.1.3 (a)). The others are wildland-urban interface (WUI) fires and wildland fires

which burn forests, crops, plantations, grass, or farmland. Over the past 30 years, the

number of wildfires exceeding 50,000 acres has increased, consequently, challenges,

related to WUI fires, of managing wildlands are on the increase [11].

(a) Structural fires

(b) Wildland-Urban interface fires

(c) Wildland fires

Fig.1.3. Three types of fire. (a) a structural fire in Illinois [12], (b) wildland-urban interface fires in JN 'Ding' Darling National Wildlife Refuge and (c) wildland fires [11].

1.2. Wildfires

A Wildland fire has a larger economic impact on large areas of forests and residence. Approximately 9,000 homes have been lost to wildfires across the US during 1985-2011 [13]. Table 1.2 shows cost estimates caused by wildland fires. A wildland fire (e.g. Indonesia during 1997-1998) costs equivalent to 6 % of the total cost of all fire in 2014 in the U.S. On the other hand, recent studies have revealed that wildland fires release a vast amount of greenhouse gases [14].

Table 1.2. The economic impact of wildfires.

Fires	Cost Estimates in million U.S. dollars	Reference
Wildfire in Indonesia during 1997-1998	20,100	[15]
Wildfire in Florida in 1998	880	[13]
Wildfires in San Diego County in 2003	2,450	[13]
Wildfire in Indonesia in 2015	16,100	[16]

Figure1.4 shows hotspots detected over the previous 24 hours on October 26, 2019, obtained from NASA's Fire Information for Resource Management System (FIRMS) [17]. Active fire data (including a location of a detected hotspot) is provided in FIRMS from NASA's Moderate Resolution Imaging Spectroradiometer (MODIS) and Visible Infrared Imaging Radiometer Suite (VIIRS) instruments generally within three hours of a satellite observation [18]. There is a large number of fires happened just for one day.
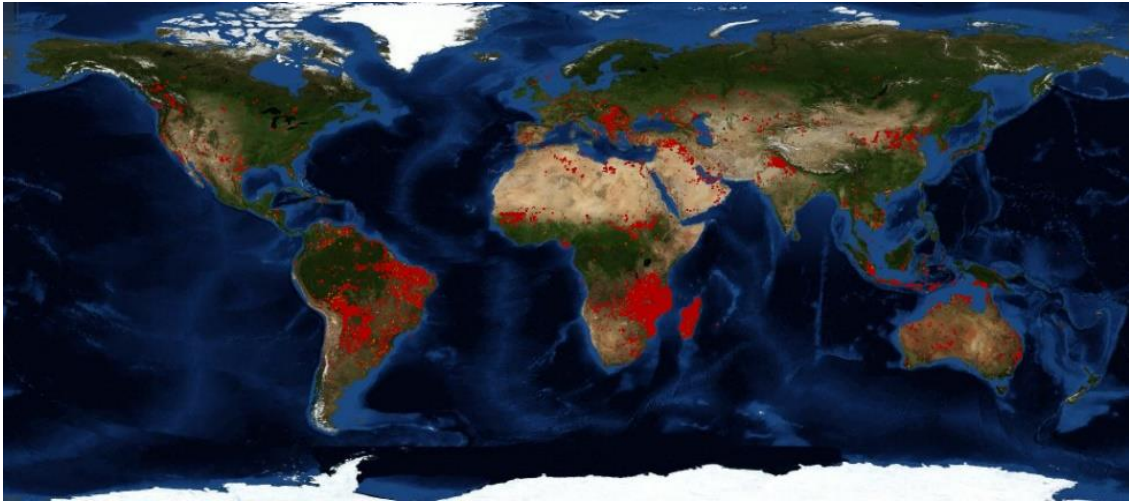
Fig.1.4. FIRMS Fire Map image from October 26, 2019. Each red dot indicates a hotspot detected over the previous 24 hours [17].

Figure 1.5 shows the schematics of the wildfire diagram. There are two major causes of wildfires. One is for natural causes such as lightning strikes, volcanic activity, sparks from rockfalls and spontaneous combustion. The other is for human causes including a campfire, smoking, debris burning, and incendiary. Once fires are ignited by the fire source, flaming fires or smoldering fires occur. When flaming fires are suppressed by firefighting or falling rain, a flame is extinguished but smoldering fires can sustain. By keeping suppression of the fire, the smoldering fire is completely extinguished. However, the suppression is insufficient to extinguish the smoldering fire, it can revive to the flaming fire via transition to flaming.

Natural causes
- Lightning strike
- Volcanic activity
- Sparks from rock falls
- Spontaneous combustion

Human causes
- Campfire
- Smoking
- Debris burning
- Incendiary (arson)

Flaming fires

Smoldering fires

Fire suppression
- Fire fighting
- Rain

Extinguished
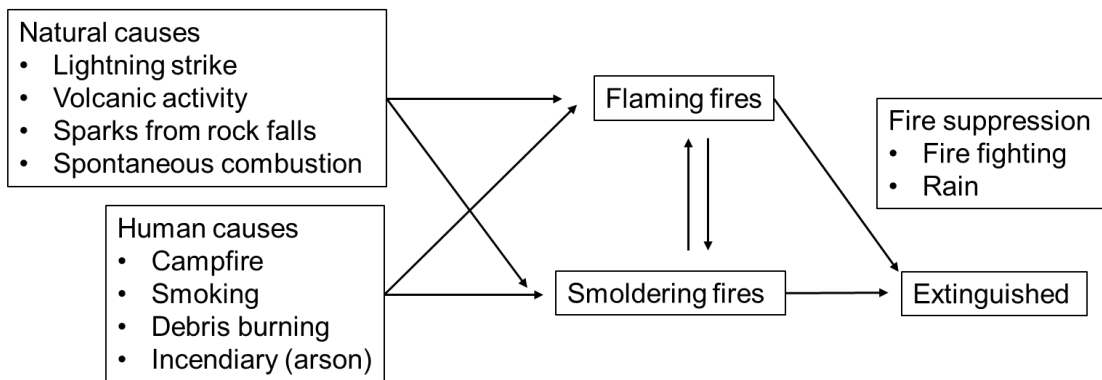
Fig.1.5. Schematics of wildfire diagram [19,20,21].

Wildland fires and coal mine fires involve smoldering fires on a large scale. Once a ton of porous combustibles in the ground starts to smolder, smoldering fires spread out not only over the ground of combustibles but below the ground. In the peatland and vegetation fire in Indonesia during 1997, for instance, it was estimated that 91.5 % of the area of peatland had burned. The amount of released carbon dioxide (CO_2) through the fires in Indonesia was estimated for $0.81 – 2.57$ gigatons of carbon and is equivalent to $13 – 40$ % of the mean annual global carbon emissions from fossil fuels [14]. Peat fires on a large scale contribute not only to the increase in greenhouse gases but also to the release of air pollution into the atmosphere. Smoke haze caused by smoldering fires has an impact on regional air quality [22]. The particle matter from vegetation and peat fires are considered as harmful substances to human health [23]. In smoldering wildfires in peatlands, smoldering fires keep advancing for weeks even years. During smoldering fires, surface

fires spread over the ground burning natural fuels such as leaves, needles, twig, bark, and

firebrands [24], interacting with the smoldering [25]. Table 1.3 shows the amount of

carbon dioxide released from wildland fires and the combustion of fossil fuels in 2014.

The CO_2 Emissions from wildland fires were estimated to be from 0.128 to 2.57 G ton

per year. These are equivalent to 0.2 – 5 % of the average annual global carbon emissions

from fossil fuels in 2014. The contributions of CO_2 emissions from wildland fires cannot

be neglected.

Table 1.3. CO₂ Emissions

Cause	Total amount	Reference
Global CO₂ Emissions from the combustion of fossil fuels in 2014	48.9 Giga (G)-ton / year	[26]
Fires		
Forest fires in Indonesia during 1997	0.81 ~ 2.57 G ton	[14]
Average fire emissions from Indonesia, Malaysia, and Papua New Guinea during 2000–2006	0.128 G ton	[27]
Average global fire carbon emissions during 1997–2001	2.0 G ton / year	[28]
Average global fire carbon emissions during 2002–2007	2.1 G ton / year	[28]

Coal mine fires around the world also contribute to grovel warming and air pollution.

Some fires have been still burning in coal-producing countries including China, the

United States, India, and Indonesia [29]. The smoke from the fires containing noxious

gases and particulate matter is likely to increase risks of respiratory disease and force

entire communities to abandon their homes [30]. In Centralia coal fire in the U.S.,

Residents of Centralia burned a garbage dump in 1962, and then the fire ignited the Buck

Mountain coal bed [31]. Extinguishing the coal fire have been attempted many times,

however, these attempts were unsuccessful. The fire in Centralia is still advancing

approximately 20 m/year.   In smoldering fires on a large scale, smoldering combustion

plays a key role to sustain wildland fires because smoldering fires can survive when

surface fires are extinguished or suppressed. To prevent the progress of wildland fires,

dominant factors of limiting behavior of smoldering combustion must be clarified.

1.3. Smoldering Fires
1.3.1. What Is Smoldering Combustion?

  As pointed out already, smoldering plays a very important role in various kinds of fires

as seen in Sec 1 1 and Sec 1.2. Let us explain the detail of smoldering and summarize its

features and potential hazard. Smoldering is one of burning processes and defined as self-

sustaining, flameless, propagating exothermic reaction wave sustained by the heat

evolved when oxygen directly attacks the surface of a condensed-phase fuel [32,33]. The

smoldering has unique characteristics such as flameless burning and emitting smoke and

toxic gases. In general, the temperature in a smoldering region is relatively lower than

flame (< 1000 °C) and smoldering velocity is very slow (< 1 mm/s) at normal atmospheric conditions. The typical examples of smoldering processes are burning porous materials of biomass Fig.1.6 (a) and smoldering cigarette Fig.1.6 (b).
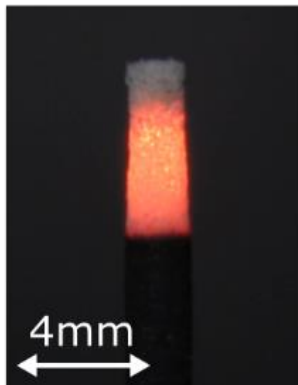
Fig.1.6 Actual images of smoldering combustion. (a) Smoldering biomass stick. (b) Smoldering cigarette.

From the viewpoint of fire safety, there are two main reasons why smoldering combustion is a significant fire hazard. One is the emitting gases from a smoldering region which consists of harmful/toxic and combustible gaseous components. Table1.4 shows the products from flaming or smoldering fires of pine needles or sagebrush or mixed fuel simulating forest-floor, ground fires; crown fires; broadcast burns, and slash pile burns [34]. In smoldering combustion, the emissions include toxic gases such as carbon monoxide (CO), carbon dioxide (CO_2), ammonia (NH_3), formaldehyde (H_2CO), and Hydrogen Cyanide (HCN).

Table 1.4. Emission factors for flaming and smoldering combustion and for the total fire (mole/kg dm (x 100)) measured by Yokelson et al. [34]

Material	Mode	Smol. Percent	Gas (Flaming)				(Smoldering)				(Pyrolysis/Distillation)					
			H_2O	CO_2	NO	NO_2	CO	CH_4	C_2H_6	NH_3	C_2H_4	C_2H_2	Acetic acid	Methanol	Formic acid	HCN
Pine needles	F[a]	22.60%	5933	4173	10.6	1.14	40.36	4.64	0.58	0.09	0.56	0.96	0.41	0.11	1.25	-
	S		3570	3334	0.84	-	656.8	126	17.9	12.8	10.8	2.96	17.1	6.69	3.63	-
Broadcast (duff, pine needles, twigs, wood)	F	25.10%	5684	3701	6.56	1.89	41.45	2.9	0.56	0.6	1.02	0.88	0.02	0.32	1.43	-
	S		2109	3215	1.67	0.19	463.1	44.3	6.08	10.6	4.85	1.55	2.19	3.01	2.91	-
Ground 2 (duff, twigs, pine needles)	Both	NA	5514	3476	5.61	3.12	212.4	23.4	3.58	7.29	4.09	2.12	4.57	2.51	5.96	-
Crown (twigs and needles, wood, pine needles, green needles and twigs)	Both	NA	6404	3279	5.14	1.43	324.5	56	6.64	6.53	11.3	4.96	11.5	9.93	9.18	0.91

[a]F, flaming; S, smoldering

12

When a smoldering fire happens in a highly enclosed environment (e.g., space habitats, closed rooms and buildings), the concentration of carbon monoxide in a closed space increase [35,36]. Exposure to carbon monoxide causes to starve the body of oxygen [36], which means that the emitting gases are an immediate danger to any life. The other reason is that the intensity of smoldering combustion is very weak yet acts as an invisible hot spot, which is enough trigger for a sudden transition to flaming combustion. Once the combustion mode changes from smoldering to flaming, the burning velocity becomes more than 10 times faster to help grow the firing zone. To prevent the transition and subsequent flaming, extinguishing smoldering in the early stage is highly demanded. However, the smoldering is hard to detect due to its weakness [37] then the area of smoldering could enlarge accordingly. Eventually, the complete suppression becomes more difficult (e.g. [38]). For example, it has been reported that the extinguishing smoldering coal required a substantial amount of water in the range from 1 to 2l of water per kg of burning fuel [39].

Many materials could smolder once the condition is fulfilled. Most of the smoldering materials are natural porous matters like wood, biomass, peat, and coal. Besides, various types of synthetic polymers can also smolder such as polyurethane foam and charring polymers. Smoldering materials need to have pore geometry to facilitates the

heterogeneous reaction by transporting heat and oxygen through porous media. At the same time, the aggregate structure provides thermal insulation that helps slow heat loss, which allows smoldering propagation despite lower heat release rates.

1.3.2.Hazards of Smoldering Fires

Figure 1.7 shows three stages of fire development of forest fires in Kalimantan, Indonesia observed by Usup et al [40]. In the first stage, the surface vegetation such as trees, leaves, and twigs are burned. The surface fires spread out through bush vegetation and ignite organic soils such as peat and muck [41]. The flaming fires generate a strong fire plume of black or dark grey color with a high concentration of soot [2]. In the second stage, the smoldering fires spread through the peat soil below 20 cm in-depth and then extended into deeper peat layers of 20-50 cm in depth (the third stage). Once smoldering fires occur, the subsequent slow-burning through organic soils continues for hours or days and they ignite other vegetation regions again [33]. The smoldering fires generate smoke plumes that remain close to the ground due to their weak buoyancy. Since the burning process of the smoldering sustains in a deeper layer of organic soils, it is hard to detect the exact location and area of smoldering fires and predict the timing of the transition from smoldering to flaming (massive) fires. Depending on the fuel, the smoldering fires can penetrate many meters below the ground and last for months. The smoke plume

emitting from the smoldering region causes not only the regional haze for long periods, but also bring a negative impact on respiratory and general health to people exposed to haze experienced [42]. With this respect, the smoldering fires can be regarded as a serious" silent killer" to cause substantial deaths and injuries.
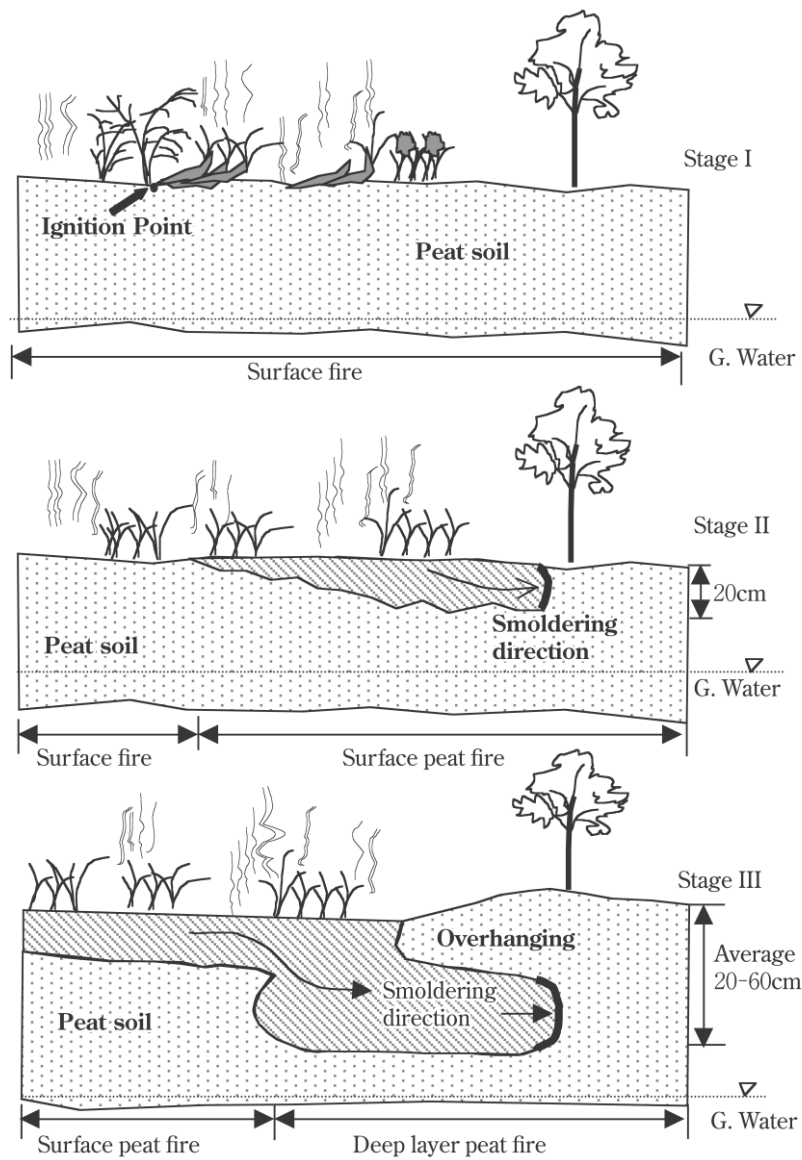
Fig.1.7. Fire development in tropical peatland of Central Kalimantan [40].

Smoldering fires are the leading cause of serious fires. In Japan, smoking cigarettes is the 1st cause for ten years at least except for arson and the number of fires caused by smoking is 3,414 (9.0 %) [1]. In the U.S., during 2012-2016, an estimated annual average of 18,100 (5 %) reported home structure fires started by smoking materials [43]. The smoldering fires start by dropping smoking materials on beds, upholstered furniture, or carpets, or in trash boxes and last for hours or days. Smoldering upholstered furniture (e.g. chairs, mattresses) produces toxic smoke in fire situations [36,44]. The major toxic products are carbon monoxide (CO), carbon dioxide (CO2), Hydrogen Cyanide (HCN), hydrochloric acid (HCl), and nitric oxide (NO) and depletion of oxygen also has a toxic effect [45]. In a typical compartment fire, acrolein is the major component of smoke and is responsible for incapacitation, whereas inhalation of Carbon monoxide is the main reason for death and injuries [46]. CO forms carboxyhemoglobin (COHb) by binding to hemoglobin in the red blood cells. COHb prevents the red blood cells from carrying oxygen to cells due to the decrease of binding sites for oxygen [47,48]. Table 1.4 shows the associated symptoms caused by exposure to CO.

Table 1.4 CO concentrations, COHb levels, and associated symptoms [47]

CO concentration [ppm]	COHb level [%]	Signs and symptoms
35	< 10	Headache and dizziness within 6 to 8 h of constant exposure
100	> 10	Slight headache in 2 to 3 h
200	20	Slight headache within 2 to 3 h; loss of judgment
400	25	Frontal headache within 1 to 2 h
800	30	Dizziness, nausea, and convulsions within 45 min; insensible within 2
1,600	40	Headache, tachycardia, dizziness, and nausea within 20 min; death in less than 2 h
3,200	50	Headache, dizziness, and nausea in 5 to 10 min; death within 30 min
6,400	60	Headache and dizziness in 1 to 2 min; convulsions, respiratory arrest, and death in less than 20 min
12,800	> 70	Death in less than 3 min

The hazard of smoldering fires is not only the sources of toxic gases to cause death to residents, but also trigger of serious fires. Figure 1.9 (a) shows the flames over the pile of clothes ignited by smoldering fires. When the intensity of smoldering fires increases to attain the critical conditions (e.g. wind enhances the sufficient oxygen supply to smoldering regions), flames suddenly appear and spread out with higher velocities. At the moment of transition from smoldering to flaming, a gas-phase ignition occurs. The reactants of the gas-phase reactions are gaseous fuel such as volatiles, CO, and hydrocarbons and the heat source is the smoldering fires that produce the gaseous fuel.

Figure 1.9 (b) shows an experiment to reproduce a firing process in bedding products conducted by Sapporo City Fire Bureau [49]. At first, a smoldering fire started from the center of the bedding product with a weak heat source (a smoking cigarette). Once the fires proceeded, the carbonized region on the comforter is enlarged for one and a half hours. Then, flames suddenly appeared over the carbonized region. Since the weak and slow fires can happen in bedding rooms or furniture such as a couch, they can lead to serious fires to cause fire-related deaths and injuries.

(a) In forced flow

Smoldering

Flames

Air blowing

Air blowing

Transition

Clothes

(b) In natural convection

0 s
Bedding
Cigarette
札幌市消防科学研究所

5591 s 00:30:11
Smoldering
札幌市消防科学研究所

5592 s 01:30:12
Smoldering
札幌市消防科学研究所

5594 s 01:33:14
ついに炎を上げて燃え始めた
Flaming
Smoldering
札幌市消防科学研究所

5603 s 01:33:23
Flaming
Smoldering
札幌市消防科学研究所
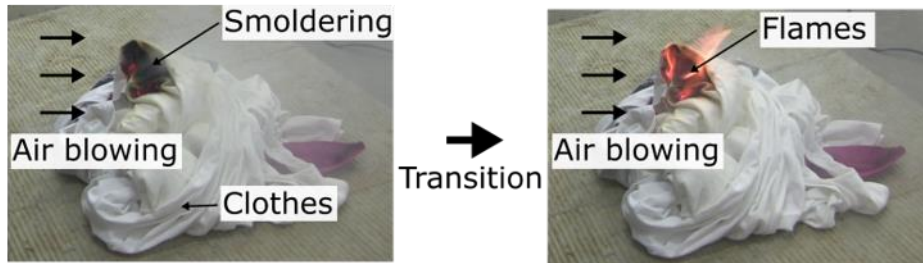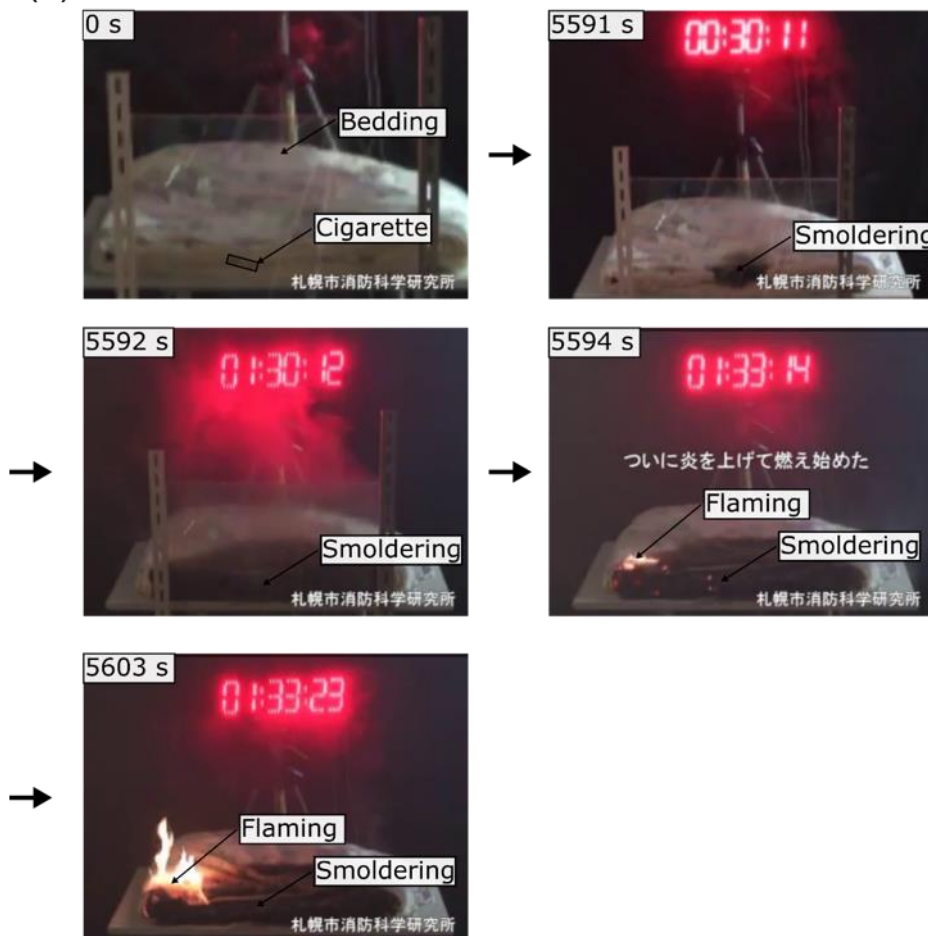
Fig.1.9. Experiment to reproduce a firing process from smoldering to flaming. (a) in the pile of clothes under conditions of forced flow. (b) in the bedding products in natural convection [49].

1.3.3. Transition to Flaming or Extinction

Critical ambient conditions in which transition from smoldering to flaming or extinction occurs have been examined and mechanisms of transition to flaming or extinction for smoldering have been discussed by some researchers.

Sato and Sega examined transient behavior of smoldering to extinction or flaming with varying oxygen concentrations with cellulosic cylinders [50]. The limits of smoldering were summarized by oxygen concentrations. Moussa investigated transient smoldering for cylindrical cellulosic material by varying pressure and oxygen concentrations [51]. Extinction limits and the limits of transition to flaming were summarized in combinations of oxygen mole fraction and partial pressure. Ortizz-Molina et al. mentioned that the oxygen transport rate to the char surface is an important factor to determine the transition behavior because the char reaction generates adequate heat flux to the pyrolysis region. Ohlemiller observed forced flow smoldering and the transition to flaming. When the smoldering direction is the same as airflow and the flow velocity is above a certain critical value, transition to flaming was observed. He suggested that both kinetics and oxygen supply rates play substantial roles in the transition to flaming. Chao and Wang examined the mechanism of the transition from smoldering to flaming combustion of a horizontally oriented polyurethane foam under natural convection [52]. They found that the occurrence of transition from smoldering to flaming and the transition time is determined

by the oxidation of the residual char left by the smoldering. Bar-Ilan et al. investigated the transition from smoldering to flaming in small polyurethane foam samples by varying oxygen supply velocity, oxygen concentrations, and radiation heat flux to reduce the heat losses to the surroundings due to the small size of samples [53]. The scale analysis developed based on the experimental results shows that the transition to flaming can be treated as a gas-phase ignition process. However, it cannot be predicted where the transition to flaming occurs. Consequently, the transition time when the transition to flaming occurs has not been summarized well. Figure 1.10 shows the transition time in the experiment for the transition to flaming from smoldering polyurethane foam obtained by Chao and Wang and Bar-Ilan et al. The transition times seem to be dispersed and have no error bars, which means that conventional experiment methods have low reproducibility. To clarify mechanisms to control the transition to flaming, an experiment with better reproducibility is needed.

For the transition to extinction, mechanisms of extinction of smoldering have been investigated through theoretical analysis. Schult et al. [54] and Decker and Schult [55] examined critical conditions to cause smoldering in polyurethane foam to extinguish through theoretical analysis under an assumption of a one-step reaction of solid fuel. Their prediction provided that the extinction occurs when the mass flux of the forced gas is

sufficiently high. Lozinski and Buckmaster examined the limit conditions in which the transition to extinction occurs [56]. These predictions were validated to experimental results in the extinction limit in which the oxidizer supply was sufficiently large, but the case for little oxidizer supply was not validated because experiment without natural convection is hardly conducted. Thus, it is inferred that mechanisms of smoldering extinction caused by insufficient oxygen supply have not examined well. Since an environment of deficient oxygen supply is supposed to be subsurface smoldering fires in deep layers of ground, a more comprehensive understanding transition to extinction from smoldering is needed to develop suppression technology for smoldering fires.

(a) Transition time varying oxygen concentration, flow velocity, and heat flux [53]
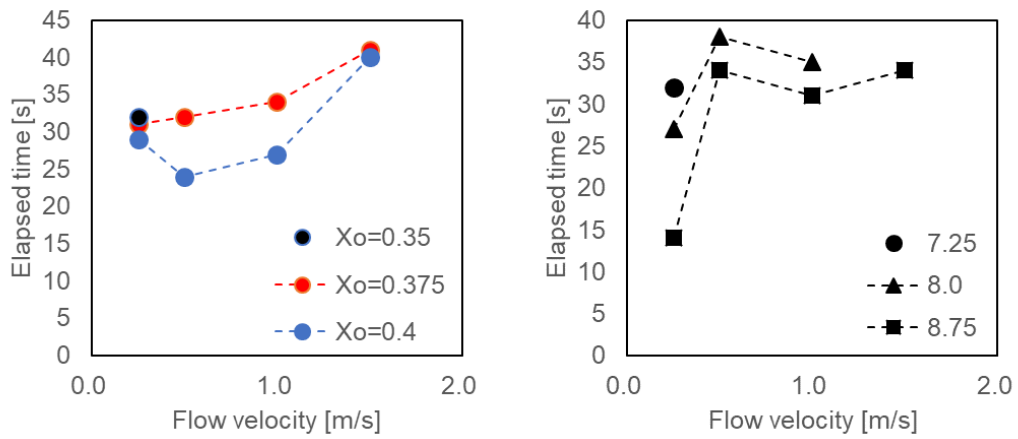
(b) Transition time varying ignition power and sample length under natural convection [52]
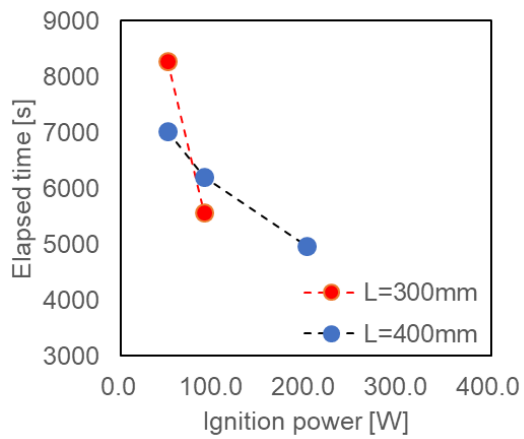
Fig.1.10. Transition time in the experiment for the transition to flaming.

1.4. Target and Objective of This Study

The target of this study is the following:

· Mechanisms of smoldering extinction caused by insufficient oxygen supply have not examined well because experiment without natural convection is hardly conducted.

· Early experiment for the transition to flaming from smoldering has low reproducibility of time or position at that transition occurs to clarify mechanisms to control the transition to flaming

The objective of this study is to develop a new experimental method for examination of transition to extinction or flaming from smoldering with high reproducibility and to clarify mechanisms to cause the transition from smoldering. Smoldering combustion plays a key role in a trigger of transition to flaming because smoldering fires can survive when surface fires are extinguished or suppressed. Examination of the transition behavior of smoldering to extinguish or to flaming and elucidation of mechanisms of transition to flaming from smoldering fires for various combustibles are quite important in fire safety. A part of the fundamentals of transition to flaming or extinction has been understood well. However, there is still much scope for discussion about mechanisms to cause the transition to flaming or extinction. For the transition to flaming, the transition phenomena

to flaming have been still uncontrollable and there are fewer experimental studies for natural materials such as wood, cellulosic material, and biomass. For the transition to extinction, a more comprehensive understanding transition to extinction from smoldering is needed because theoretical predictions of transition to extinction from smoldering in an environment of deficient oxygen supply have not been validated with experimental results due to experiments under natural convection.

2. Literature Review

This section provides a short review of early research on smoldering combustion.

2.1. Fundamentals of Smoldering Combustion

The characteristics of smoldering have been investigated by many researchers. In the early stage of research on smoldering combustion, the experiment was conducted under natural convection as shown in Fig.2.1 (a). Cohen and Luft investigated burning behavior for some types of powdered combustibles such as coal dust, sawdust, metal powder, Sulphur and identified smoldering materials [57]. Palmer investigated the smoldering behaviors of the dust of cork, deal wood, and grass and wood fiber insulation board [58]. He found that the minimum depth of dust layer for smoldering is a function of the mean particle diameter of dust and smoldering sustained inside deposits of dust up to 85 cm deep. For smoldering cigarettes, an experimental method of smoldering combustion in the cylinder was adapted as in Fig. 2.1 (b). Egerton et al. studied the mechanism of smoldering in cigarettes using an x-ray method to measure the temperature history of hot gases and the surface of solid [59]. During the puff, both temperatures are high, the surface reaction temperatures reaching 1200 ℃. Gugan predicted the combustion zone shape on a diffusion-controlled model and the smoldering temperature using the calorific value [60].

(a) Smoldering combustion in unconfined conditions

Unburned fuel
(ex. Natural fuel)
Pyrolysis
Ash
Char oxidation
Smoldering
(ex. Natural fuel)
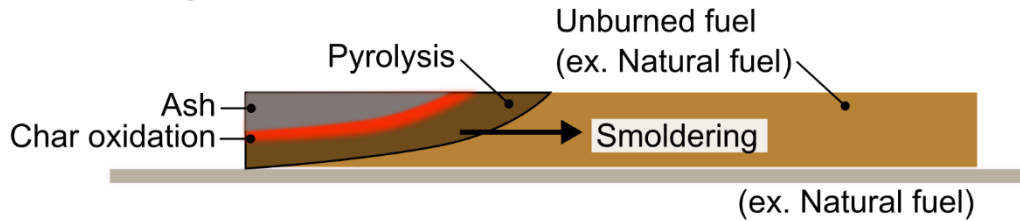
(b) Smoldering combustion confined in duct

Pyrolysis
Char oxidation
Residual char
Unburned fuel
(ex. Synthetic fuel)
Oxidizer
Smoldering
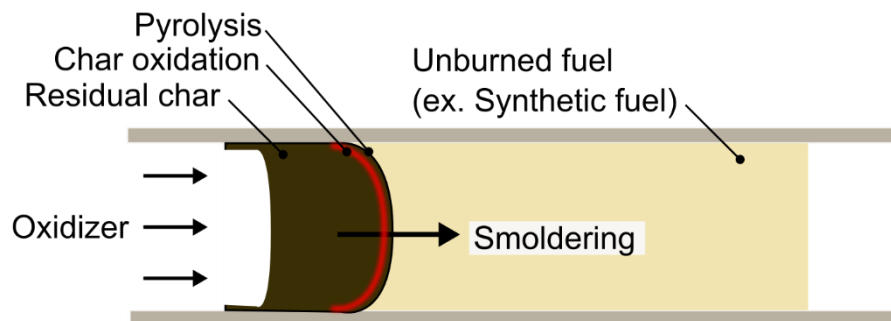
Fig.2.1. Conventional experimental methods.

In the late 1970s, research on smoldering behavior of polyurethane foam has attracted

much attention to preventing home fires because bedding products, upholstered furniture,

and sofas commonly used in most residential buildings include flexible polyurethane

foam. Smoldering fires can initiate in polyurethane foams with a cigarette or weak heat

source. Salig studied smoldering in flexible polyurethane foam with a cigarette and fabric

[61]. He found that smoldering fires are enhanced by a convective airflow when the

crevice is formed by the horizontal and vertical components of the polyurethane foams

(Fig.2.2). Rogers et al. investigated smoldering combustion of flexible polyurethane foam

and fabric with or without flame retardants [62]. The experimental results and developed kinetic model inferred that effective retardants against the foam suppress the char formation from degraded foam or char oxidation.
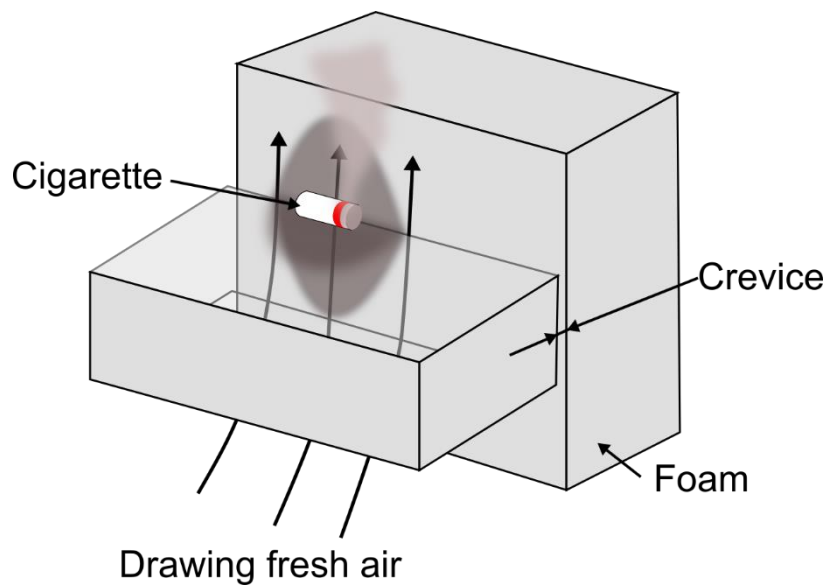
Fig.2.2. Airflow through the crevice between the two foams drawing fresh air.

Research on fundamentals of smoldering combustion in the 1970s or earlier provided knowledge that the flow of oxygen supplied to a smoldering region plays an important role in smoldering behavior. After the late of the 1970s, the experimental methods of confined smoldering as shown in Fig.2.1 (b) have been frequently adapted to examine smoldering behavior. Ohlemiller and Rogers established a 1-D smoldering experiment and examined the influence of heat loss and oxygen supply on forward smoldering of

polyurethane foams with low or high permeability [63]. The competition in degradation to a smolder-suppressing tar or a smolder-enhancing char was influenced by products such as water and retardants and physical factors like heating rate and smoldering configuration. Ohlemiller et al. developed the two major overall reaction model of char formation and char oxidation. The comparison between the model solutions and experimental results showed that the smoldering process of flexible polyurethane foams is oxygen-limited [64]. Ohlemiller and Lucca conducted an experimental comparison of forward and reverse smoldering propagation with two types of fuels, cellulosic insulation, and polyisocyanurate. The schematic of the experimental apparatus for forward and reverse smoldering is shown in Fig.2.3. It is found that reverse smoldering quickly reaches a steady propagation rate determined by heat transfer processes, that forward smolder propagation is unsteady, and that both smoldering modes are limited by the rate of oxygen supply [65]. Torero et al. carried out an experimental study of the effect on the reverse smoldering through a forced oxidizer flow and for analyzing the potential effect of buoyancy in the process using polyurethane foam [56]. These observations indicated that buoyancy has a significant role in the smoldering process because buoyancy-induced flow can influence the weak smoldering process even though the oxygen supplies are small.
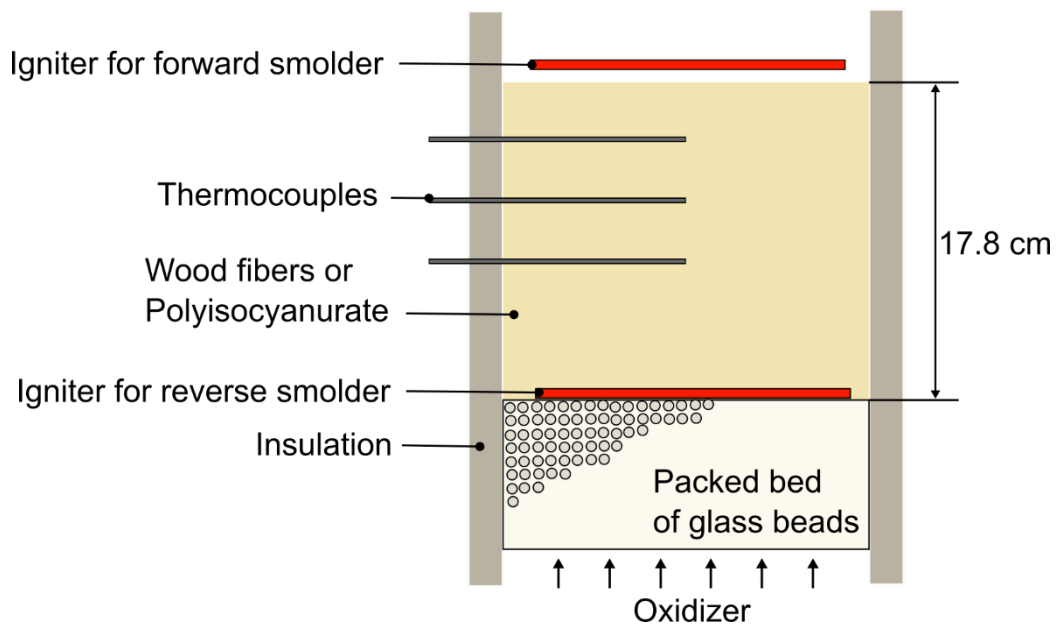
Fig.2.3. Schematic of smoldering experimental apparatus.

During the period from the 1990s to 2000s, several limited experiments to investigate the influence of gravity on smoldering combustion for fire safety in the confined cabins of spacecraft and knowledge of smoldering behavior without natural convection. Stocker et al. [66] and Walther et al. [67] have investigated forward and opposed smoldering through flexible polyurethane foam in both micros- and normal gravity environments. These results showed that gravity plays an important role in the transport of oxidizer to sustain the smoldering. Bar-Ilan et al. have investigated the forward smoldering through flexible polyurethane foam in both micros- and normal gravity [68]. In microgravity, the reduced heat loss by the less buoyancy-induced flow promotes secondary char oxidation,

which causes the consumption of a large amount of oxygen and inhabitation of smoldering due to insufficient oxygen. Bar-Ilan et al. also investigated the reverse smoldering through flexible polyurethane foam in both micro- and normal gravity [69]. In the case of opposed smoldering under micro- and normal gravity, the effect of gravity on smoldering was found to be the opposite trend, namely, that the range of extinction limit becomes wider in microgravity.

2.2. Smoldering Structure

As shown in Fig.2.1, two types of experimental geometry have been used for the investigation of smoldering combustion. One is unconfined geometry used for reproducing a real phenomenon such as cigarette or charcoal burning. The other is confined geometry often applied to experimental apparatus that porous combustible is packed in the duct and gaseous oxidizer is passed through the combustible to discuss the simple structure of smoldering. Moreover, there are two ways in which smoldering combustion can proceed based on the relationship between the directions of smoldering propagation and oxidizer flow. The two smoldering modes are shown in Fig.2.4. One is "forward smoldering combustion". For 1-D forward smoldering combustion in (Fig.2.4 (a)), the smoldering front propagates through the porous combustible in the same

direction as the oxidizer flow. The hot gases like volatiles and combustion gases flow over the fuel and heat the unburned region. Due to the heating the unburned fuel from hot gases, smoldering velocity is accelerated gradually. According to the experimental result obtained by Egerton et al, the temperature of the surface reaction reaches 1200 ℃ for a smoldering cigarette during the puff [59]. Since the high temperature in smoldering is attained in forward smoldering, the transition to flaming from smoldering can be observed.

The other is "reverse smoldering combustion" in Fig.2.4 (b). In reverse smoldering combustion, the oxidizer flow is supplied against the smoldering propagation direction, for instance, smoldering an incense stick [70]. When an incense stick is set vertically and ignited on the top of the stick, smoldering proceeds downwardly. That configuration produces steady smoldering propagation because the hot gases from the smoldering region do not affect the unburned region. When smoldering combustion is in a steady-state, a steady flame structure can be obtained. Mathematically, the smoldering rate is given as an eigenvalue of the two-boundary problem, just as with the 1-D premixed flame theory or the flame spread theory.

(a) Forward Smoldering through a combustible

Char oxidation
Residual char
Unburned fuel
(ex. Polyurethane foam)

Oxidizer ⟶

Smoldering

Igniter

Pyrolysis

(b) Reverse Smoldering through a combustible

Unburned fuel
(ex. Polyurethane foam)

Residual char
Char oxidation

Oxidizer ⟶

Smoldering ⟵

Igniter

Pyrolysis
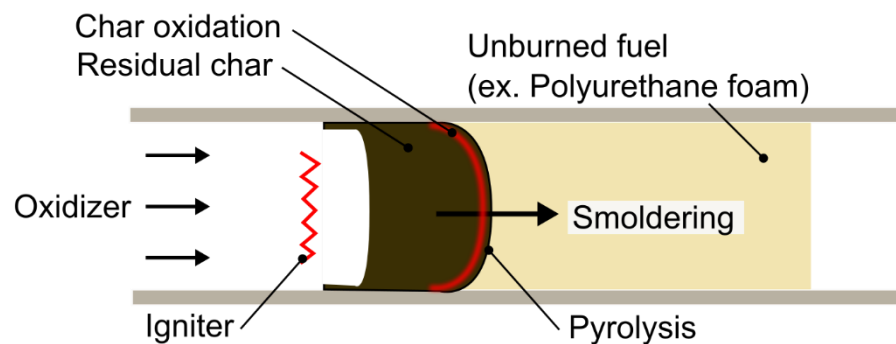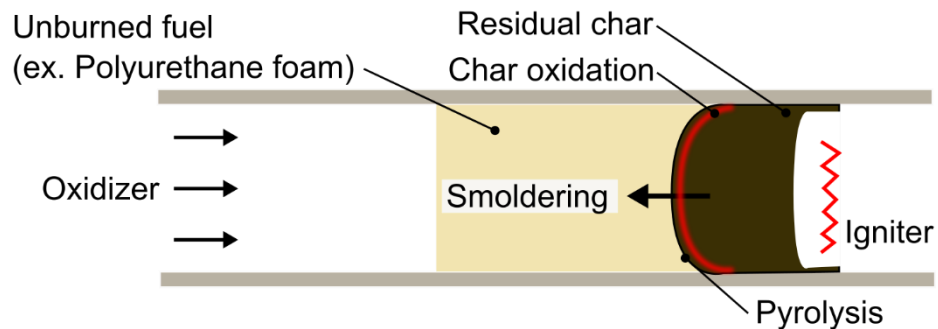
Fig.2.4. Forward and reverse smoldering combustion.

The analytical methods frequently used for flame spread studies [71] can be applied to the forward and reverse smoldering combustion. Dosanjh et al. applied activation energy asymptotic to forward smoldering in polyurethane foam to conduct a parametric investigation [72]. They successfully obtained steady the smoldering rates and found that the smoldering rate is linearly depending on the mass flux of oxidizer. Fatehi and Kaviany applied activation energy asymptotic to reverse smoldering in a packed bed of wood particles. Their predictions in the oxygen-limited regime are in good agreement with the

33

experimental results [73]. Roy et al. [74] and Roy and Nakamura [75] developed a

universal model of reverse and forward smoldering in a steady and unsteady state.

2.3. Chemical Kinetics

Chemical kinetics in smoldering combustion are quite complex. To handle the chemical

reactions, many models have been proposed. The simple reaction systems were provided

by Ohlemiller [32]. The schematic diagram of the reaction paths is shown in Fig.2.5. One

is char-forming pyrolysis and oxidative pyrolysis reactions and the other a char oxidation

reaction. In general, the global reactions approximated by the two chemical pathways,

pyrolysis, and oxidation, can be expressed in the following equations [39].

Pyrolysis:
$$\text{Fuel (solid)} + \text{Heat} \rightarrow \text{Pyrolyzate(gas)} + \text{Char (solid)} + \text{Ash (solid)} \tag{2.1}$$
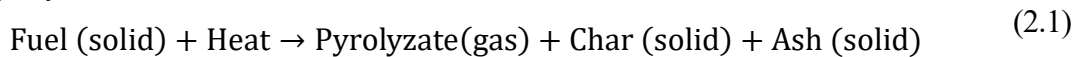
Heterogeneous oxidation:
$$\text{Char (solid)} + O_2 \text{ (gas)} \rightarrow \text{Heat} + CO_2 + H_2O + \text{other gases} + \text{Ash (solid)} \tag{2.2}$$

Gas-phase oxidation:
$$\text{Pyrolyzate (gas)} + O_2 \text{ (gas)} \rightarrow \text{Heat} + CO_2 + H_2O + \text{other gases} \tag{2.3}$$
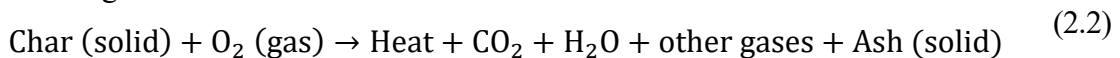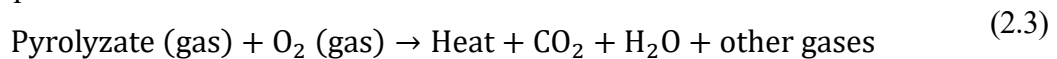
A solid fuel pyrolyzes by heating and produces pyrolyzate, char, and ash. Char oxidation

is a heterogeneous reaction and takes place on the char produced by the pyrolysis reaction

generating heat. Gas-phase oxidation of pyrolyzate takes place in the gas phase with heat

release. Char is a carbon-rich porous material with a high surface-to-volume ratio and high heat release of reaction. Although it depending on fuel, for example, pyrolyzate contains carbon monoxide (CO), carbon dioxide (CO_2), methane (CH_4), hydrogen (H_2), and light hydrocarbons such as ethene (C_2H_6), propene (C_3H_8), and nitrous compounds in biomass pyrolysis [76]. When the combustibles include an inorganic material (such as silica (SiO_2), calcium oxide (CaO), and potassium oxide (K_2O) [77]), the combustion residual is left after the smoldering combustion and acts as a thermal insulator and catalytic reaction [76].

Multistep reaction models have been also developed extensively to represent experimental observations [78,79]. Applying such a multistep reaction model, the kinetic study focus on peat fire has been also developed [80].
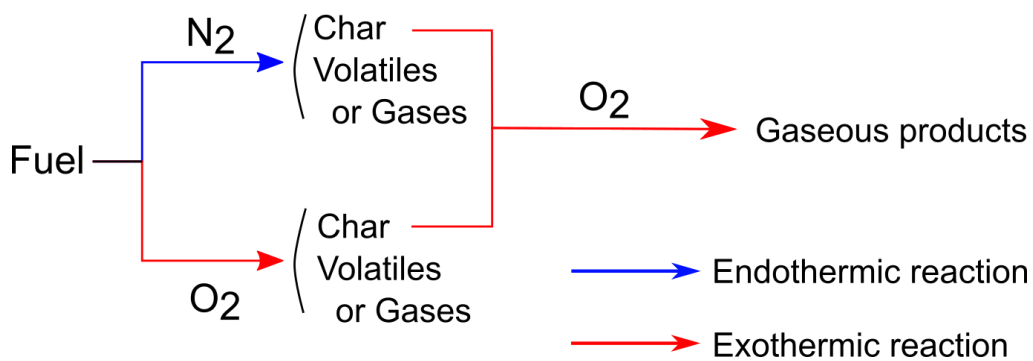
Fig.2.5. Three-step reaction model proposed by Ohlemiller [32].

2.4. Extinction of Smoldering

Sato and Sega used two kinds of cylinder-shaped fuels as specimens (namely, cardboard and filter papers) [50]. The schematics of the experiment are shown in Fig.2.6. They examined the points of extinction and transition to flaming by varying the imposed oxygen concentration. Although the extinction point has been experimentally identified, the mechanism leading to the extinction was discussed little.
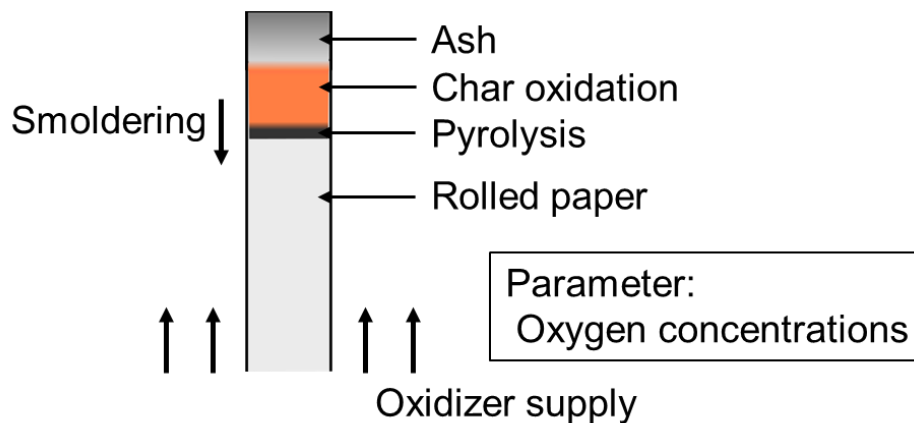
Fig.2.6. Schematics of the experiment conducted by Sato and Sega [50].

Moussa has examined the effect of pressure and oxygen concentration on the smoldering of a cellulosic element experimentally as well as theoretically [51]. The schematics of the experiment are shown in Fig.2.7. Their work successfully revealed the decreasing trend of burning rate and temperature as the extinction condition was approached. Nevertheless, the experimental data near the extinction limit was not well provided.
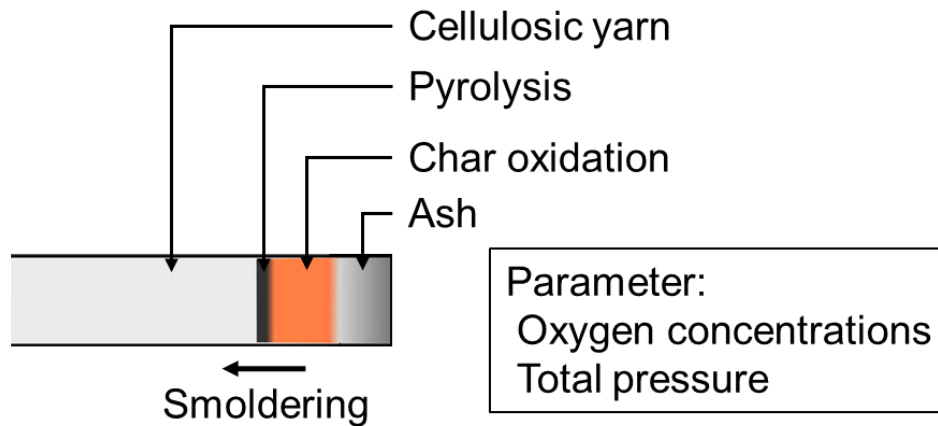
Fig.2.7. Schematics of the experiment conducted by Moussa [51].

Schult et al. [54] and Decker and Schult [55] examined critical conditions to cause

smoldering in polyurethane foam to extinguish through theoretical analysis under an

assumption of a one-step or two-step reaction of solid fuel. Fig. 2.8 shows schematics of

results for predictions of extinction limits for solid or gas deficient cases. For solid

deficient cases, their calculation led extinction with oxygen depletion because oxygen

depletion is caused by the char oxidation reaction, thus the mass flux of the forced gas is

sufficiently high. Whereas, for gas deficient cases, extinction can be observed when the

mass flux of the forced gas is sufficiently low. Lozinski and Buckmaster examined the

limit conditions in which the transition to extinction occurs. Taking account of an

endothermic pyrolysis reaction to the theoretical model, predicted smoldering behavior

mimicked experimental results obtained by Torero et al [56]. These predictions were validated to experimental results in the extinction limit in which the oxidizer supply is sufficiently large, but the case for little oxidizer supply was not validated because experiment without natural convection is hardly conducted.
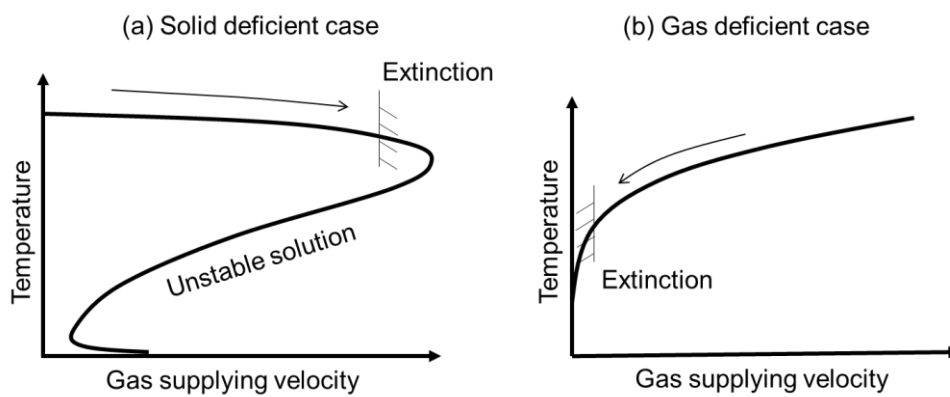
Fig.2.8. Schematics of results for theoretical predictions of extinction in polyurethane foam by Decker and Schult [55]. (a) Solid deficient case. (b) Gas deficient case.

2.5. The Transition from Smoldering to Flaming

Sato and Sega examined the behavior of smoldering and flame spread with varying oxygen concentrations with cellulosic cylinders [50]. The critical oxygen concentrations when flame spreads occur decrease with the decrease of diameters of the cylinder, whereas the critical oxygen concentrations when smoldering is extinguished are almost constant. Moussa investigated both steady and transient smoldering for cylindrical cellulosic material in oxygen and nitrogen environments of varying pressure and

compositions [51]. Extinction limits and the limits of transition to flaming were summarized in combinations of oxygen mole fraction and partial pressure.

Ortizz-Molina et al. conducted an experimental investigation to determine the major factors governing the smoldering behavior of flexible polyurethane foams in environments of varying the gas composition and pressure [81] as shown in Fig. 2.9. The transition to extinction or flaming occurred at the critical values of the ambient oxygen concentrations and oxygen partial pressures.
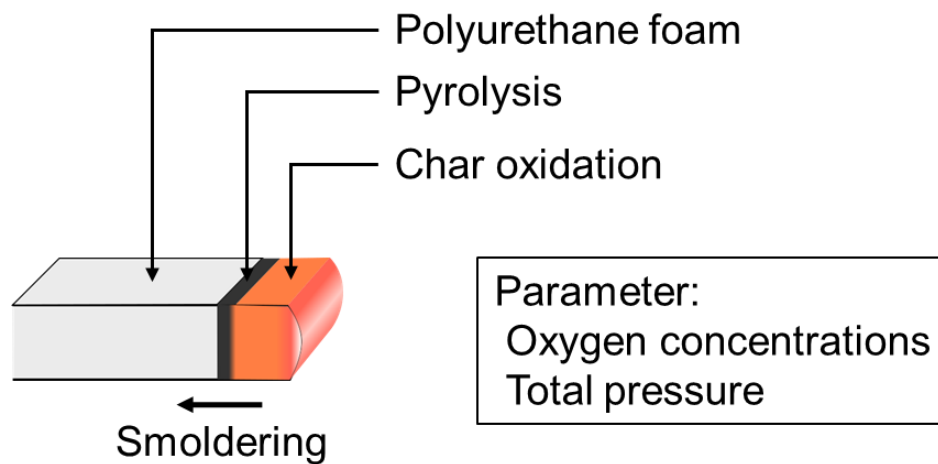
Fig.2.9. Schematics of the experiment conducted by Ortizz-Molina et al [81].

Ohlemiller investigated the transition from smoldering and flaming in cellulosic insulation [82]. The schematics of the experiment are shown in Fig.2.10. He varied the flow velocity over the horizontal layer of cellulosic material in forward and reverse

directions and found that the transition only occurred in forward smoldering and originated in a local region, along the leading edge of the smoldering. The reason for the transition to flaming was explained that the hot gases of volatiles and combustion gases heat the smoldering region because the leading-edge region of smoldering is kinetically controlled.
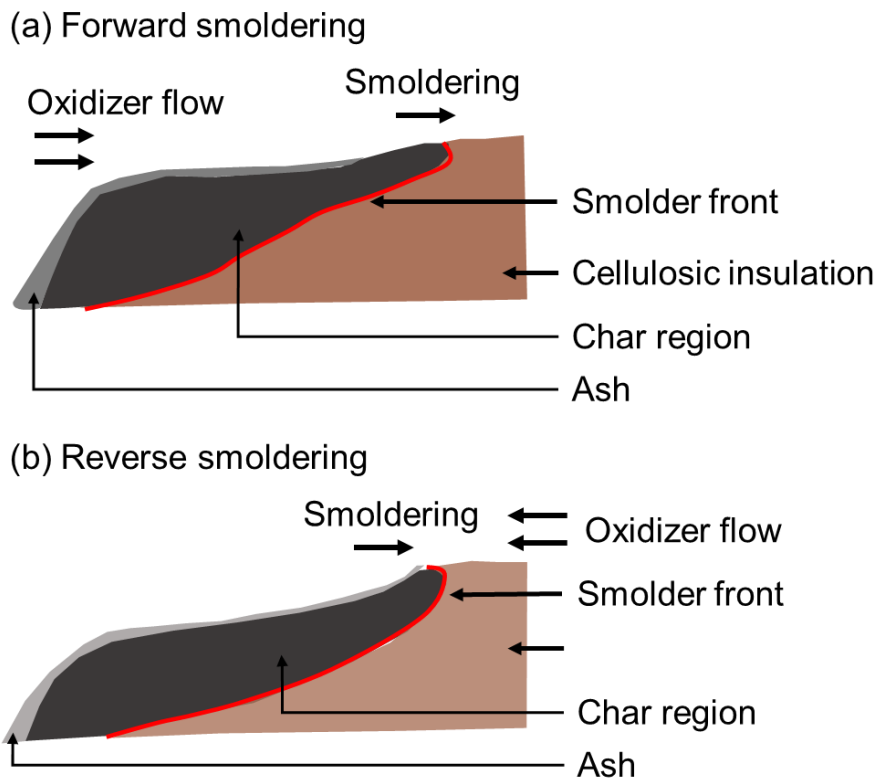
Fig.2.10. Schematics of the experiment conducted by Ohlemiller [82].
(a) Forward smoldering experiment. (b) Reverse smoldering experiment.

Bar-Ilan et al. investigated the transition from forward smoldering to flaming using small polyurethane foam samples. It was found that the trigger of the transition was the char

upstream of the smoldering region. Some researchers have argued that the transition to

flaming can be observed in forward smoldering because unburnt fuel is heated up by the

hot gases from the smoldering. A few researchers observed a transition to flaming in

reverse smoldering [51,81].

  Aldushin et al. studied the possibility of a transition from reverse smoldering to flaming

in polyurethane foam by numerical simulation as shown in Fig.2.11 [83]. They

reproduced the transition to flaming by adding an extra oxidizer to participate in the char-

oxidation reaction, which causes the temperature to rise until the gaseous reactions started.

They mentioned that the transition to flaming can be caused in the char oxidation region.
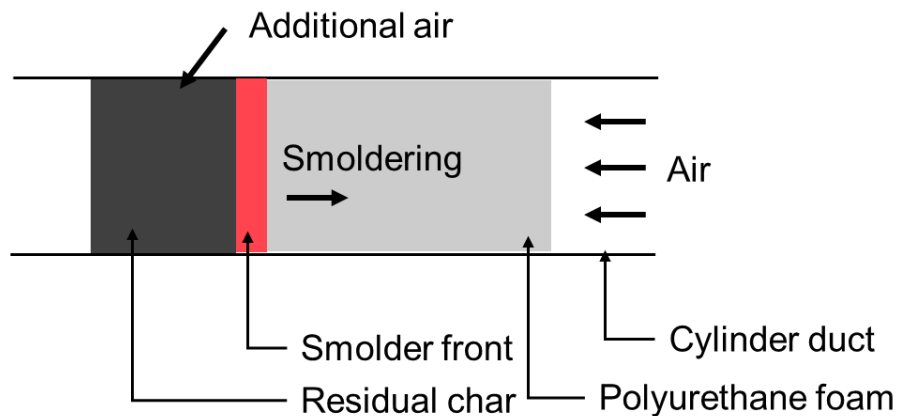
Fig.2.11. Schematics of computational model [83].

Chapter 3

3. Influence of Total Pressure on Smoldering

3.1. Introduction

In the past research of fundamental smoldering combustion, microgravity is used for eliminating natural convection because the extinction limit of smoldering cannot be observed. However, the cost of a microgravity experiment is high and the size and weight of the experimental apparatus are limited in the space station or space crafts. It is hard to experiment smoldering with dense combustibles under natural convection in a small chamber to ensure that the change of the oxygen level is negligible during the experiment. To avoid the limitation of the experiment, a method using a low-pressure environment has been proposed as one of the approaches for the experiment under reduced natural convection. In this study, not only a low-pressure environment is adapted to our experimental environment, but also a thin biomass stick is used for suppressing buoyancy-induced flow based on the scale modeling [84]. Smoldering experiment with a low-pressure environment and a thin biomass stick expects the advantages of examination for both extinction limits and transition to flaming from smoldering because of the reduced disturbance of natural convection. However, the influence of a low-pressure environment on smoldering combustion has not been well understood due to few studies on that topic. In this chapter, the influence of a low-pressure environment on smoldering

combustion is examined, and then the low-pressure method for examination for both

extinction limits and transition to flaming from smoldering is verified.

3.2. Material

  A dried incense stick (Nihon Kodo Co., Sasara Binchotan) was selected as the biomass

stick. The incense stick is a thin-rod biomass stick that consists of mainly the sawdust of

bark of *Machilus thunbergi* and has homogenous properties of porosity and composition

due to commercial products (Fig.3.2). The diameter of the incense stick is 2 mm and the

length is 150 mm. This small-diameter allows ambient gases to diffuse into the center of

the incense stick even though the porosity is relatively lower than such a polyurethane

foam, cotton, and cellulose yarn.
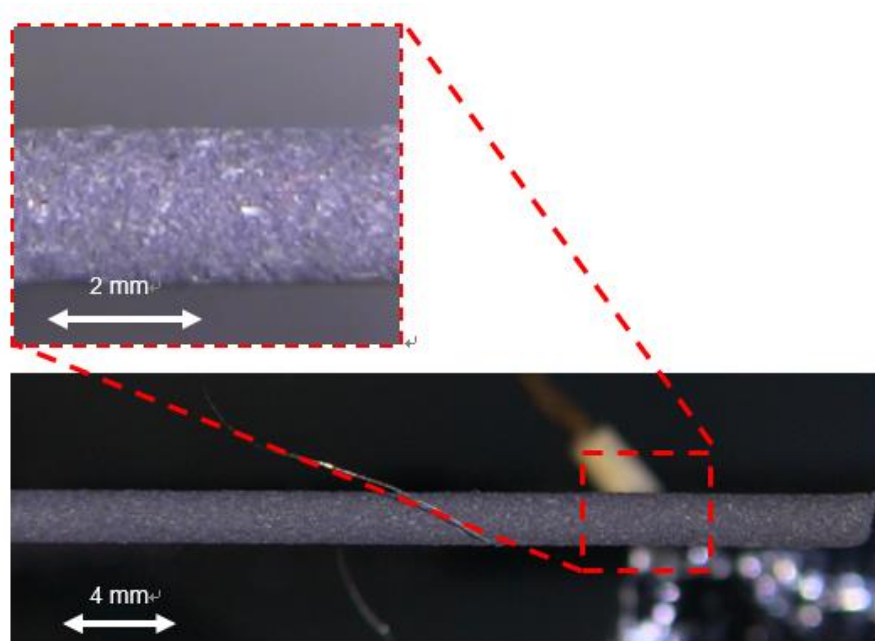
Fig. 3.1. An Incense stick used in the experiment.

In early studies [85,82], the surface shape of the biomass stick was changed through the experiment because oxidizer is supplied to the dense fuel by flowing over its surface. It means that the thermal structure in the smoldering region and the flow field over its surface are complex. Using a thin-rod incense stick, the surface of the smoldering region is hardly changed (Fig.3.2), so that a 1-D smoldering structure is formed. Since the incense stick is a fragile material, it is difficult to measure the temperature in the smoldering region for the biomass stick less than a 2-mm diameter. On the contrary, a thicker (larger) sample is easy to measure the temperature, however, it cannot hold 1-D burning feature, so that multi-dimensionality is additionally considered.

(a) Incense stick   (b) Cellulosic insulation
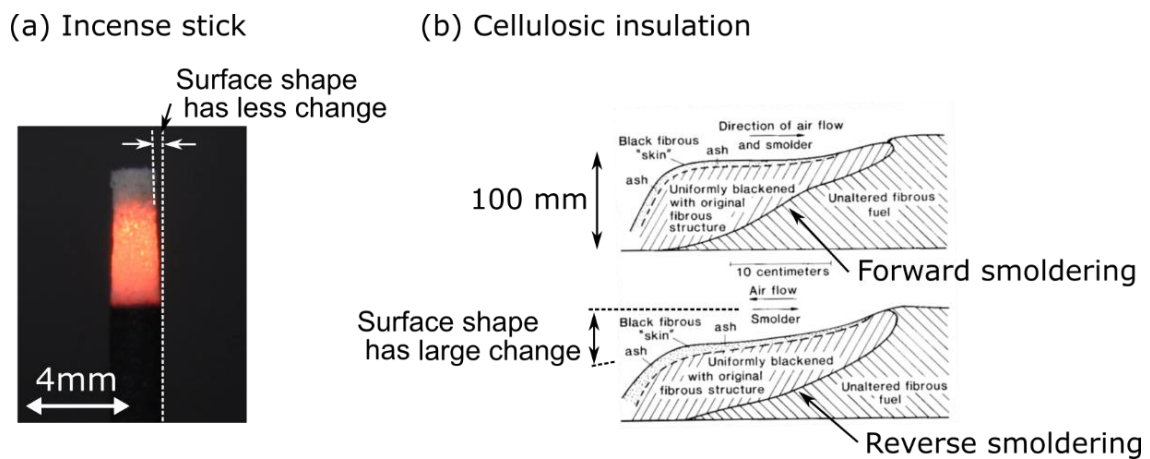
Fig.3.2. Surface shape in the smoldering region. (a) Smoldering incense stick. (b) Smoldering cellulosic insulation [82].

The physical properties of the incense stick are similar to wood samples. Table 3.1 shows the physical properties of the incense stick. The normal bulk density is 0.97 and the

porosity is 0.42 measured by the mercury injection method. Since the density of wood is

between 0.401 and 1.156 g/cm^3 and the porosity of wood is between 22.1 and 73.68 %

as shown in table 3.2 [86], the incense stick is considered as a representative sample of

wood. Therefore, the thin-rod incense stick is suitable for smoldering experiment in a

low-pressure environment.

Table 3.1 Physical properties of the incense stick

Physical properties	Unit	Value
Normal bulk density	g/cm^3	0.97
Specific density	g/cm^3	1.66
Porosity	—	0.42
Total pore area	m^2/g	13.96
Median pore diameter (volume)	μm	2.62

Table 3.2 Density and porosity of wood samples [86].

Wood species	Normal bulk density $[g/cm^3]$	Specific density $[g/cm^3]$	Porosity [%]
Ekki	1.042	1.487	29.92
Beech	0.781	1.472	46.93
Sycamore maple	0.483	1.512	68.05
Norway spruce	0.401	1.524	73.68
European Larch	0.588	1.481	60.30
Macassar ebony	1.156	1.484	22.10
Oak	0.706	1.528	53.81
Scots pine	0.451	1.489	69.71

3.3. Theoretical Aspects of the Effect of Transport on Smoldering
3.3.1. Surrounding Flow Field along a Vertical Biomass Stick

The numerical origin is set at the burning zone so that the origin moves at the constant rate (u_s), although we could assume that u_s is much smaller than gas flow velocity ($u_s \ll |\boldsymbol{v}|$). In free-convection heat transfer [87,88], continuity, motion, and energy equations in the cylindrical coordinates (r, θ, z) are expressed as

$$\nabla \cdot \boldsymbol{v} = 0 , \tag{3.1}$$

$$\overline{\rho_g}(\boldsymbol{v} \cdot \nabla \boldsymbol{v}) = -\nabla P + \mu \nabla^2 \boldsymbol{v} - \overline{\rho_g}\boldsymbol{g}\bar{\beta}\left(T_g - \bar{T}\right) , \tag{3.2}$$

$$\rho_g c_p\left(\boldsymbol{v} \cdot \nabla T_g\right) = k \, \nabla^2 T_g , \tag{3.3}$$

where $\boldsymbol{v}$ is the flow velocity vector with components v_r, v_θ, v_z [m/s], ρ_g is the density of gases [kg/m^3], P is the pressure term expressed as $p + \overline{\rho_g}gh_a$ [Pa], p is the pressure [kPa] , h_a is the height [m], μ is the viscosity of gases [Pa·s], $\overline{\rho_g}$ is the density at a mean temperature between the peak temperature on the smoldering region and the ambient temperature [kg/m^3], $\boldsymbol{g}$ is the gravity acceleration vector [m/s^2], T_g is the temperature of gases [K], $\bar{T}$ is the average temperature of gases between the peak and ambient temperature [K], c_p is the specific heat at constant pressure [J/kg·K], and k is the thermal conductivity of gases [W/m·K]. For the vertical direction, the gravity vector is given as

$$g = (0, \quad 0, \quad g), \tag{3.4}$$

and the gravity vector for the horizontal direction is given as,

$$\boldsymbol{g} = (g \cos \theta, \quad g \sin \theta, \quad 0). \tag{3.5}$$

To find some dimensionless parameters to characterize the flow systems, dimensionless

parameters are introduced with the characteristic quantities as follows:

$$\widetilde{\nabla} = L\nabla, \tag{3.6}$$

$$\widetilde{\boldsymbol{v}} = \frac{\boldsymbol{v}}{v_0}, \tag{3.7}$$

$$\widetilde{P} = \frac{P - P_0}{\rho_g v_0{}^2}, \tag{3.8}$$

$$\widetilde{T} = \frac{T_g - T_0}{T_w - T_0}. \tag{3.9}$$

Here, L is the characteristic length [m], v_0 is the characteristic velocity [m], P_0 is the

ambient pressure term [Pa], T_w is the surface temperature of the smoldering region [K].

In terms of these dimensionless parameters, the equations in Eq. (3.1) – (3.3) are

transformed to

$$\widetilde{\nabla} \cdot \boldsymbol{v} = 0, \tag{3.10}$$

$$\left(\widetilde{\boldsymbol{v}} \cdot \widetilde{\nabla}\widetilde{\boldsymbol{v}}\right) = -\widetilde{\nabla}\widetilde{P} + \frac{1}{Re}\widetilde{\nabla}^2\widetilde{\boldsymbol{v}} - \frac{Gr}{Re^2}\left(\frac{\boldsymbol{g}}{|\boldsymbol{g}|}\right)\left(\widetilde{T} - \frac{1}{2}\right),$$ (3.11)

$$\left(\widetilde{\boldsymbol{v}} \cdot \widetilde{\nabla}T_g\right) = \frac{1}{Re\ Pr}\ \widetilde{\nabla}^2\widetilde{T}.$$ (3.12)

The dimensionless numbers are defined as

$$Re = \frac{\overline{\rho_g}Lv_0}{\mu},$$ (3.13)

$$Gr = \frac{\overline{\rho_g}^2 g\bar{\beta}(T_1 - T_0)}{\mu^2},$$ (3.14)

$$Pr = \frac{c_p\mu}{k}.$$ (3.15)

Figure 3.3 shows schematics of the smoldering model along with a rod-shaped stick at atmospheric pressure and in a low-pressure environment. The smoldering combustion occurs through the porous media, which means that oxygen is transported to the smoldering region by convection. A boundary layer is formed over the smoldering region due to the buoyancy-induced flow. In the boundary layer, Reynolds number can be regarded as unity when the characteristic length is taken as the boundary layer thickness. The Prandtl number consists of physical properties and then it considered as a constant value (for air, $Pr = 0.72$). Therefore, the flow field along the biomass stick is governed by the Grashof number comparing orders of magnitude of the dimensionless numbers.

Normal pressure

Low pressure

Smoldering

Heat loss

Oxygen transport by convection

Oxygen diffusion through porous media

Dence and porous material

z

g

r

u_s

Y_o

u_{diff}

Smoldering

Heat loss

Oxygen diffusion

Oxygen diffusion through porous media

Dence and porous material

z

g

r

u_s

Y_o

u_{diff}
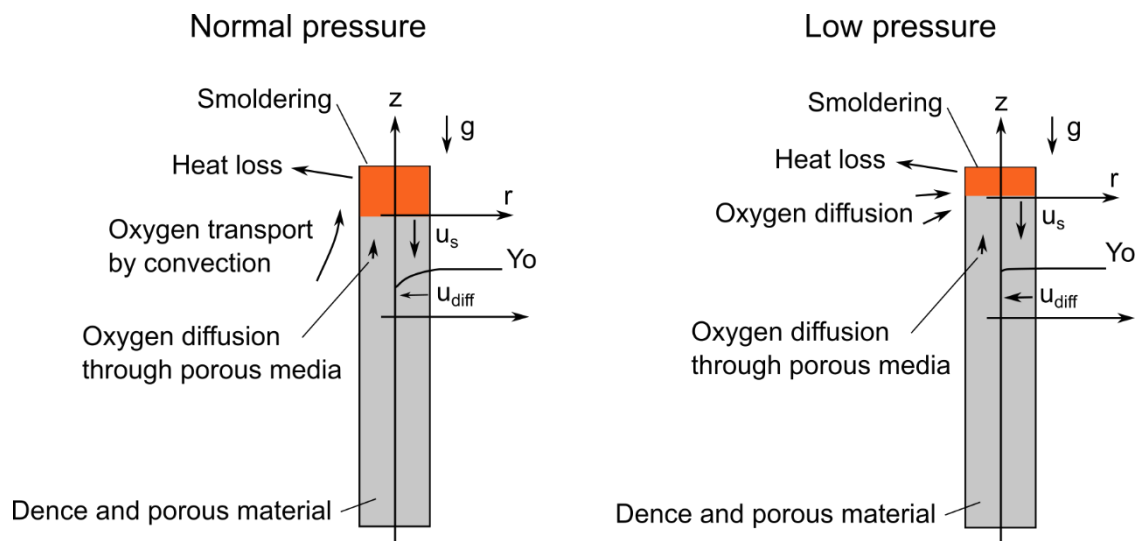
Fig. 3.3. Schematics of the model of the smoldering biomass stick (test specimen) with the small diameter and the flow field around the smoldering stick. The coordinate system of the smoldering is along the vertically downward.

In the governing equations of surrounding flow along with the smoldering biomass stick, the flow is induced by the buoyancy force. The buoyancy force is a function of the density of the surrounding gases from Eq. (3.11) and (3.14). Reduction of the density of the surrounding gases makes Grashof number small, as a result, reducing ambient pressure contributes to a reduction of the driving force for the flow of surrounding gases. This idea is based on the scale analysis of the transport process of solid combustion (Grashof number scaling concept) [84]. A low-pressure environment also reduces the influence of natural convection on the smoldering region. Moreover, a low-pressure environment increases the stability of laminar flow due to the principles of the theory of stability of laminar flows [89]. Thus, the reduction of disturbance of oxidizer to the smoldering region induced by natural convection allows us to provide the experimental environments

49

for the transition to flaming with less flow disturbance and for observation of smoldering

behavior near the extinction limit like micro-gravity environment.

3.3.2.Oxygen Transport through a Biomass Stick

Oxygen transport is presumed to be driven by the gas flow through a permeable biomass

stick and molecular diffusion. For the flow, the flow field through the biomass stick

expects to be governed by Darcy's law [90]. The flow velocity is defined as

$$u_d = -\frac{K}{\mu}\frac{dp}{dz},$$ (3.16)

where u_d is the Darcian velocity [m/s], K is the permeability [m^2]. In this study, an

incense stick is used as the biomass stick, which consists of wood powder and has a

porosity of 0.4. Referring to the works done by Dai et al. [91], it is assumed that oxidizer

gases pass through voids between impermeable particles of wood. The normalized

permeability is approximated as a modified Carman-Kozeny relation [90],

$$\frac{K}{l^2} = 2.0 \times e^{-6}\frac{\phi^3}{(1-\phi)^2},$$ (3.17)

where ϕ is porosity in the porous material, l is the interparticle (center to center)

distance in the lattice. For the incense stick, the interparticle distance is as estimated as

$l = 33\ \mu m$ under hypothesis that the lattice is considered as *body-centered cubic* (BCC)

with gaps of 10 % of l between the interparticle and the porosity is 0.4 and from the

experimental data that the particle size distribution of the powdered incense stick shows

a strong peak at $30 - 40\ \mu m$ [92]. The pressure gradient is expressed as $dp/dz =$

$-\overline{\rho_g}g$ and then the order of the pressure gradient is estimated to be about 10 Pa/m.

Consequently, the predicted permeability is $9.6 \times 10^{-13}\ m^2$ and then the predicted

Darcian velocity is 6.0×10^{-7} m/s.

On the other hand, the oxygen is also transferred by molecular diffusion from the side

(radial direction toward the center axis). To estimate the order of diffusion velocity, a one-

dimensional unsteady diffusion problem is considered. The concentration profiles can be

described in the following form [93]:

$$\frac{Y_o - Y_{o,\infty}}{Y_{o,ini} - Y_{o,\infty}} = \frac{2}{R_s} \sum_{n=1}^{\infty} \frac{J_0(b_n r)}{b_n J_1(b_n R_s)} \exp[-D_e b_n^2 t], \qquad (3.18)$$

where Y_o is the mass fraction of oxygen [-], $Y_{o,\infty}$ is the mass fraction of oxygen at the

surface at $r = R_s$ [-], $Y_{o,ini}$ is the mass fraction of oxygen at the initial time [-], D_e is

the effective diffusion coefficient [m²/s], the $b_n's$ are roots of $J_0(b_n R_s) = 0$, $J_0(br)$ is

the Bessel function of the first kind of order zero, the radius of the porous cylinder is

$R_s = 1.0 \times 10^{-3}$ [m]. The effective diffusion coefficient was estimated using the

following equations [94,95]:

$$D_e = \frac{\varphi}{\tau}\left(\frac{D_{ij}D_{iK}}{D_{ij} + D_{iK}}\right) , \tag{3.19}$$

$$D_{ij} = \frac{0.00186 T^{\frac{3}{2}}}{p_{atm}\sigma_{ij}{}^2\Omega}\left(\frac{1}{M_i} + \frac{1}{M_j}\right)^{\frac{1}{2}} , \tag{3.20}$$

$$D_{iK} = \frac{d_{pm}}{3}\sqrt{\frac{8RT}{\pi M_i}} , \tag{3.21}$$

$$\tau = \varphi^{-0.5} , \tag{3.22}$$

where φ is the porosity of the biomass stick [-], τ is the tortuosity [-], D_{ij} is the binary diffusion coefficient [m²/s], T is the temperature of gases [K], p_{atm} is the ambient pressure [atm], σ_{ij} is the collision diameter [Å], Ω is the collisional integral, M_i and M_j are the molecular weights of gas species i and j [g/mol], d_{pm} is the mean pore size of the porous media [m], R is the universal gas constant [J/mol-K].

For the calculation of the effective diffusion coefficient, the following assumptions are considered: (1) the binary diffusion occurs between oxygen (O_2) and carbon monoxide (CO), (2) the temperature of gases in the biomass stick is 900 K, (3) the adapted pressure is 10 kPa, and (4) the mean pore size of the porous media is estimated at 3×10^{-6} m from the measured data of the pore size distribution done by the mercury porosimetry analysis (Micromeritics, AutoPore V 9600). The estimated effective diffusion coefficient is $D_e = 0.3 \, m_2/s$. Applying the diffusion coefficient to Eq. (3.18), the diffusion velocity can be calculated. Figure 3.4 shows profiles of mass fraction and diffusion velocity of

oxygen in a biomass stick for unsteady-state oxygen diffusion in the case of $R_s = 1.0$ mm

and $Y_{o,\infty} = 0.23$. At $t = 0.01$ s, the maximum velocity is 2.8×10^{-3} m/s. When

oxygen is consumed by oxidative reactions, diffusion velocity of oxygen (order of

velocity is 10^{-3} m/s) is larger than Darcian velocity (order of velocity is 10^{-6} m/s) in

the comparison between gas flow through a permeable material and molecular diffusion.

  Mass flux of oxygen which penetrates through an unburned zone is independent of total

pressure, whereas oxidative reactions of char depend on the partial pressure of oxygen.

Thus, a reduction in the burning rate in a low-pressure environment can be attained

keeping oxygen mass flux enough to sustain the reactions.
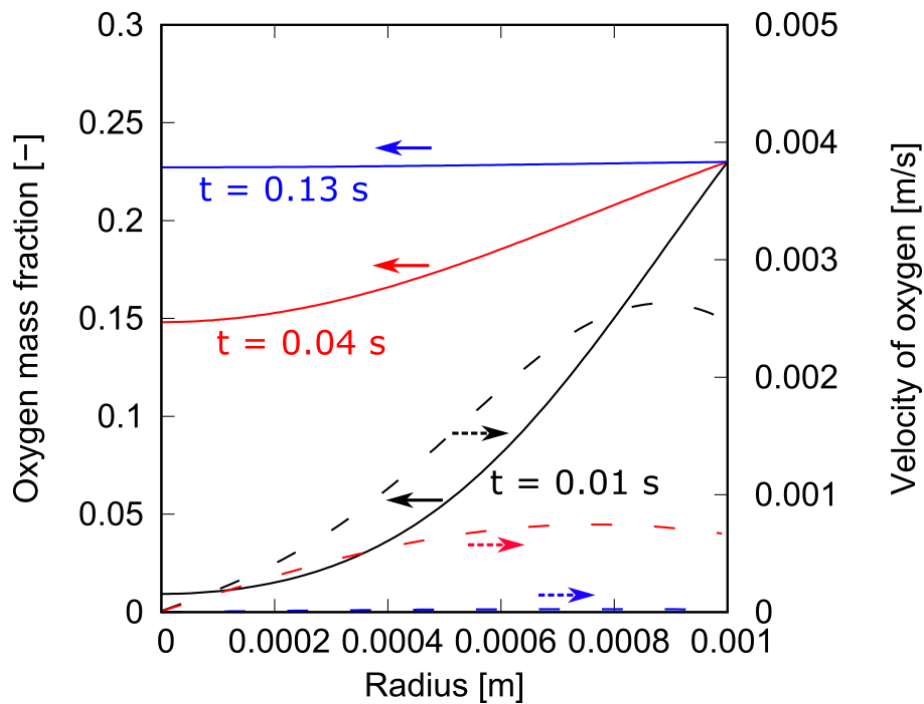
Fig. 3.4. Profiles of oxygen mass fraction and diffusion velocity of oxygen for unsteady-state mass transfer in a biomass stick.

3.4. Experimental Setup
3.4.1. Experimental Apparatus

A schematic diagram of the experimental setup is shown in Fig.3.5. The experiments of a

smoldering biomass stick made of biomass were conducted in a vacuum chamber. The

chamber size is 500 mm × 650 mm in the cross-section and 770 mm in height. This size

is sufficiently large comparing the size of the biomass stick, and the change of the oxygen

level is consequently negligible during operation.

The orientation of the biomass stick is set either at vertical or horizontal to the ground

level to compare the potential contribution of free convection on the smoldering stick. An

electrical igniter made of nickel-chromium wire was placed at the top of the biomass stick.

Before experimenting, the biomass sticks were placed in an oven at over 40 °C for more

than two hours to remove any moisture. Before the start of the experiment, air in the

chamber was removed by a vacuum pump (Adixen, rotary pump) up to 0.5 - 0.7 kPa in

absolute. Then research-grade oxygen and nitrogen dried gases (both purities are 99.5 %)

were introduced into the chamber at the prescribed partial pressure to set the target

ambient atmosphere. The adapted pressure range was from 1 kPa to 100 kPa to secure the

accuracy of oxygen concentration. The oxygen levels in the oxidizer are either 0.23 or

0.38 in mass fraction, Yo [-], to examine the effect of ambient oxygen on the smoldering

structure. After waiting for three minutes to ensure that a quiescent environment is

achieved in the chamber, the ignition procedure was started. Ignition is made by nickel-chromium wire put on top of the biomass stick with 60 W for fifteen to twenty-five seconds.
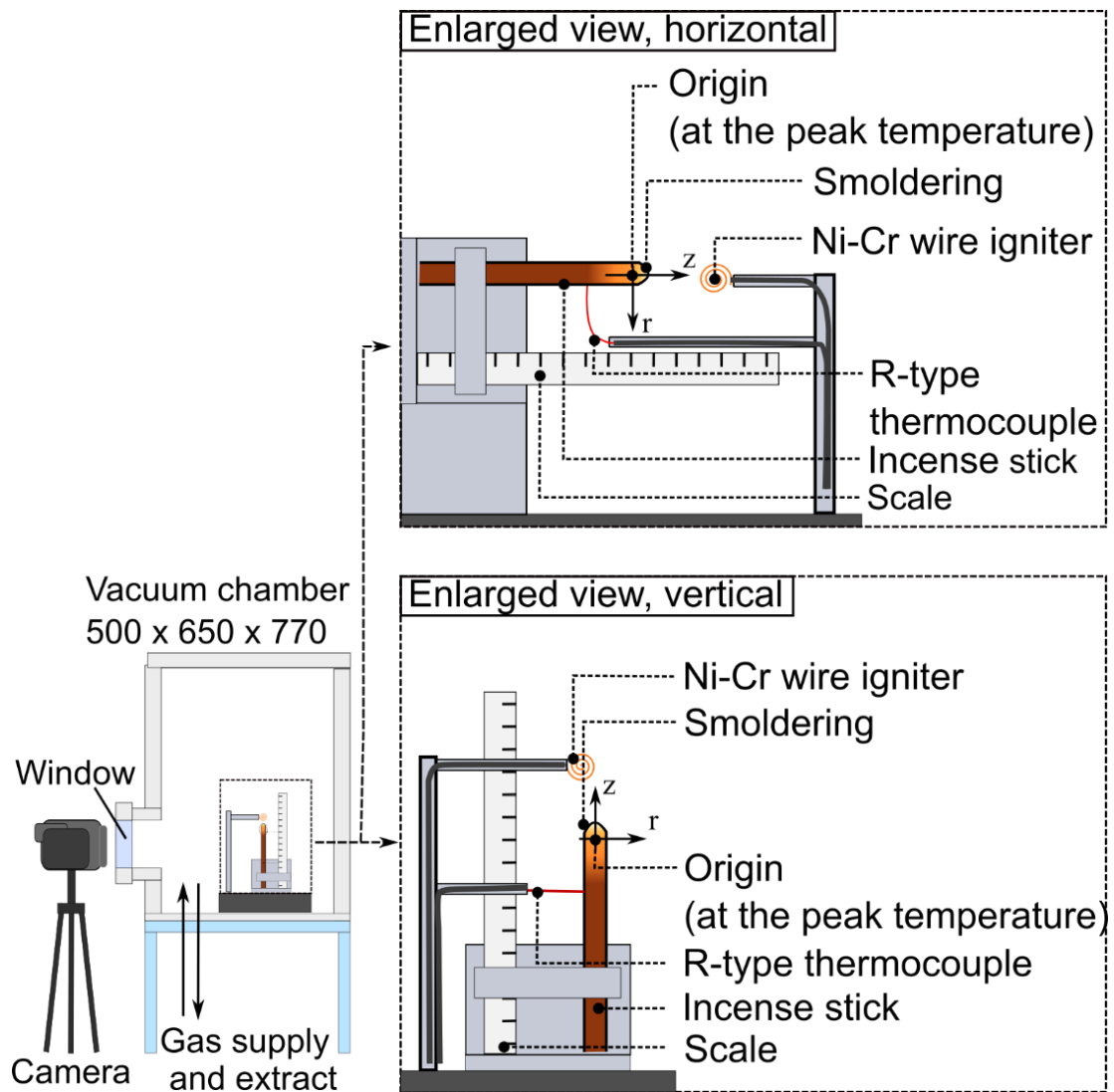
Fig.3.5. Schematic of experimental apparatus.

3.4.2.Measurement Methods

The movement of the smoldering front was recorded by a video camera (Canon iVIS HF G10, interlace 24 fps, less than 1/24 seconds in exposure time) through the observation window (Fig.3.5). For Yo=0.23 and below 20 kPa, the ISO sensitivity was set to 10 dB to ensure better visibility. The frames of interest were extracted from the recorded data for image analysis. Using the image processing software ImageJ Fiji [96], the positions of the smoldering front were extracted from each image and the smoldering rate was then calculated. Time zero (t = 0 sec) is defined as the moment when the biomass stick is ignited. The experiment was repeated at least three times for each adapted pressure.

Measurement of the temperature in the center of the biomass stick was conducted as shown in Fig.3.6 (a). A 0.2 mm-diameter hole was made at 15 mm from the top of the biomass stick to avoid the influence of the igniter and then an R-type thermocouple (0.05 mm in diameter, 0.10 - 0.15 mm of junction size) was embedded into the hole. The signal history from the thermocouple was recorded by a data logger (Graphtec, GL900). An example of temperature history is shown in Fig.3.6 (b). The temperature history can be converted to a temperature profile since the smoldering rate of the opposed smoldering is considered to be constant in the steady-state from experimental results. Then, the temperature profile inside the biomass stick was obtained. The converted profile is shown in Fig.3.6 (c). The origin is set at the peak temperature along the axial axis and the

negative sign corresponds to the preheat zone (virgin fuel).
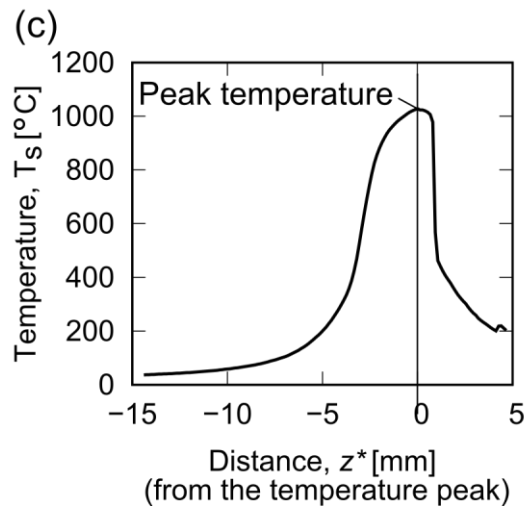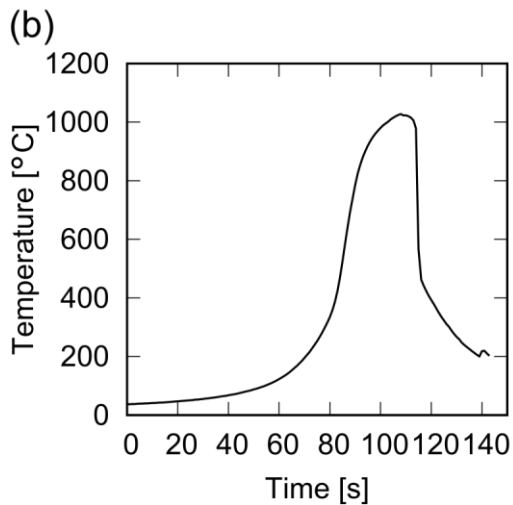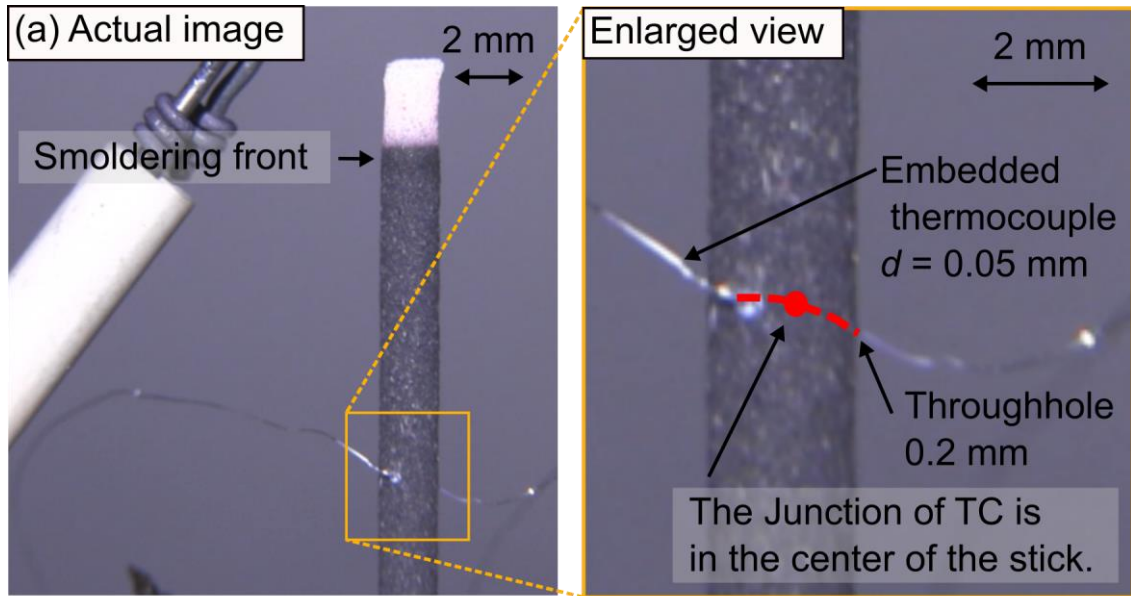
Fig.3.6. Temperature measurement. (a) magnified image of the location where the fine thermocouple is embedded, (b) obtained temperature history of the embedded thermocouple, (c) the temperature profile converted from (b) with smoldering rate. Note that the origin is set at the location of peak temperature.

3.5. Experimental Results
3.5.1. Combustion Mode

Direct images of the smoldering biomass stick at the represented conditions are shown in Fig. 3.7 – 3.9 for both vertical and horizontal cases with various oxygen levels. The (red) luminous zone can be observed in all conditions, where the extensive surface oxidation is expected. For $Y_O = 0.23$, the length of the luminous zone decreases with decrease the adapted pressure irrespective of the orientation of the biomass stick. The remained ash deposition was found at the post smoldering zone. The amount of remaining ash in the vertical case was larger than the horizontal case because gravity assists the fall-off of the ash. When the adopted pressure is over 40 kPa, the length of the luminous zone in the vertical case becomes longer than that in the horizontal case. For horizontal cases at relatively high pressures, the luminous zone on the upper surface of the stick tends to be brighter than the lower surface due to the impinging buoyancy-driven flow (i.e., gravity effect). When the adopted pressure is lower than 40 kPa, the length of the luminous zone in both orientations is nearly identical and both luminosities are uniform, suggesting that the effect of orientation (namely the role of the buoyancy flow) on the smoldering behavior becomes minor. Figure 3.8 shows direct images of the smoldering and the transition to flaming for $Y_O = 0.38$. Almost identical trends depending on the pressure were observed except for the relatively higher-pressure levels. At 100 and 80 kPa, the

transition from smoldering to flaming was observed only in the horizontal case (see Fig. 3.8 (b).), but no transition occurred in the vertical case. This difference indicates the effect of orientation on the smoldering behavior. In the image at 72 s for 80 kPa, the tiny crack in the ash region appeared and then the gaseous reaction initiated from the crack. In the horizontal case, the shape of the smoldering and ash regions is easily changed due to the gravity. The length of the luminous zones of smoldering gradually increases with time until the transition occurs. This is the reason that the luminous zone for 100 and 80 kPa are shorter (picture is in growing stage). Even at Y_O = 0.38, we can similarly find that the length of the luminous zone for both orientations becomes (nearly) identical and its luminous intensity for both orientations is quite uniform when adopted pressure level decreases, although its intensity strongly depends on the applied oxygen concentration.

Fig.3.9 shows direct images of the smoldering in Y_O = 0.53 within a limited range of pressure. The intensity of the luminous zone in both vertical and horizontal directions is stronger than the cases of Y_O = 0.53 and 0.23. A similar trend to that in Y_O = 0.23 was observed except for the near-extinction limit. At the near-extinction conditions, the length of the luminous zone in the vertical case was slightly longer than that in the horizontal case, even though it was a lower pressure environment. This might be the effect of remaining ash, which may prevent heat losses from the hot zone to the ambient.
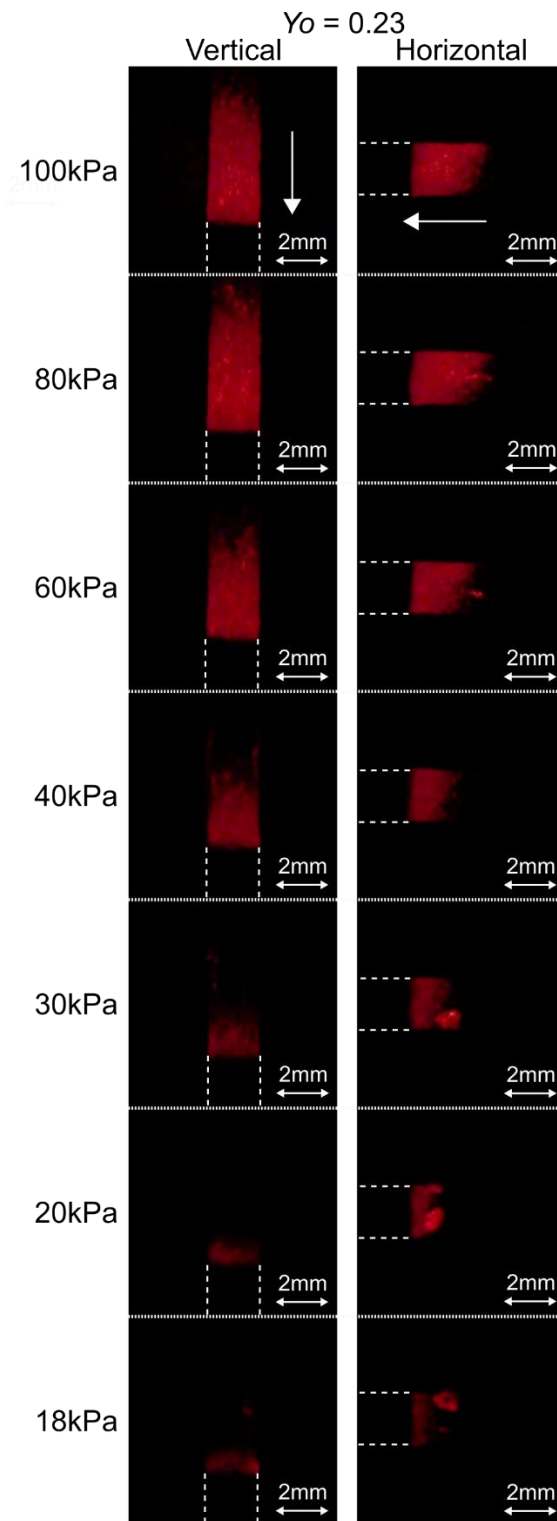
Fig. 3.7. Direct images of the smoldering 2-mm-diameter incense stick with various environmental conditions along vertically downward and horizontal orientations. Y_O = 0.23, P = 18 – 100 kPa. To improve the visibility of images, the brightness of all images was adjusted.
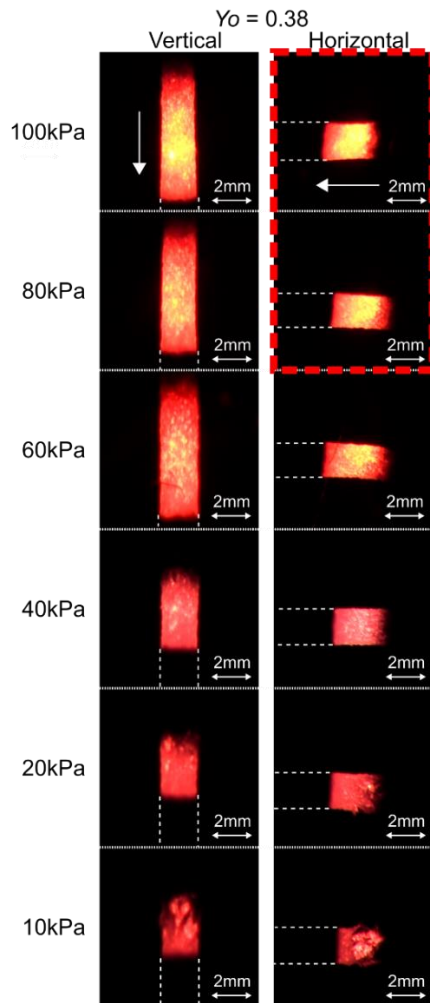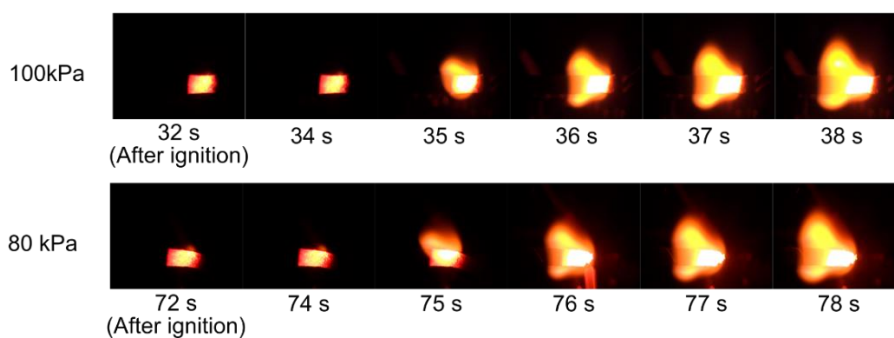
Fig. 3.8. Direct images of the smoldering 2-mm-diameter incense stick with various environmental conditions along vertically downward and horizontal orientations. (a) Smoldering in Y_O = 0.38, P = 10 – 100 kPa. (b) Sequential images of the transition from smoldering to flaming along the horizontal orientation. Y_O = 0.38, P = 100 and 80 kPa. Note that no such transition was observed for the vertically-oriented case.
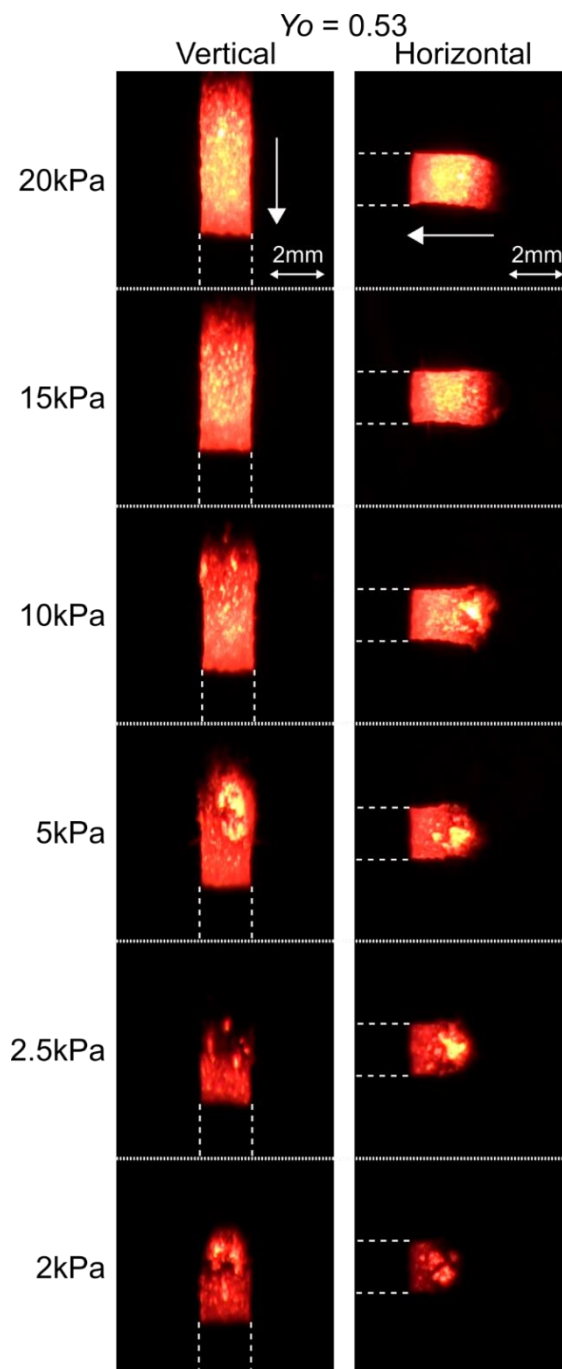
Fig. 3.9. Direct images of the smoldering 2-mm-diameter incense stick with various environmental conditions along vertically downward and horizontal orientations. Y_O= 0.38, P = 10 − 100 kPa.

3.5.2. Propagation Velocity

The smoldering rates along the vertical and the horizontal cases were obtained by the time sequence of the measured smoldering front. Representative results are shown in Fig. 3.10, showing that the smoldering progress in steady-state and its rate can be defined as the slope in the plot. In Fig. 3.10 (d), time-history of the location of the moving burning front shows the smoldering progress and flame spread because the transition to flaming from smoldering occurred at 68 s. The pressure effect on the smoldering rate is summarized in Fig.3.11 (a) for $Y_O = 0.23$, Fig.3.11 (b) for $Yo = 0.38$, and Fig.3.11 (c) for $Yo = 0.53$. The error bars represent the 95 % confidence intervals of a mean calculated from (at least) three-time trials for each adapted pressure. For $Y_O = 0.23$ in Fig.3.11 (a), the smoldering rate decreases in both the vertical and horizontal cases as the pressure decreases. These trends are consistent with the results predicted by Moussa [51]. The decrease of the smoldering rate against the pressure is linear over 60 kPa, while the decrease becomes larger until extinction. The extinction limits in both vertical and horizontal cases exist between 15 kPa and 18 kPa in the present experiment. The influence of natural convection on supplying oxygen onto the smoldering zone is expected to be larger when the pressure is larger. It is noted, however, that the difference of smoldering rates between the vertical and horizontal cases is within uncertainty, suggesting that the

effect of gravity due to the difference in sample orientation on the smoldering rate is minor in the present study. A similar trend is found for $Yo = 0.38$ in Fig.3.11 (b), hence, it is understood that the gravity effect on the smoldering rate stays minor as long as a small-scale biomass stick (2-mm diameter rod) is used. However, it should be emphasized that the identical smoldering rates between the vertical and the horizontal cases do not mean the thermal structures in the smoldering biomass stick are identical under the different imposed environmental conditions. Suppose if the structures are the same for both orientations, we would not observe the transition only for the horizontal case at Yo = 0.38 (not observed in the vertical case) as shown in Fig.3.8. Therefore, the gravity can cause the difference in the thermal structure depending on the orientations.

For $Y_O = 0.53$ in Fig.3.11 (c), the smoldering rates indicate the higher values than Yo = 0.23 and 0.38. The trend of the smoldering rate is similar to the other results. However, the range of total pressure in which smoldering combustion appears seems to be small because the transition to flaming occurs above 30 kPa.

(a) *Yo* = 0.23, P=80 kPa, vertical
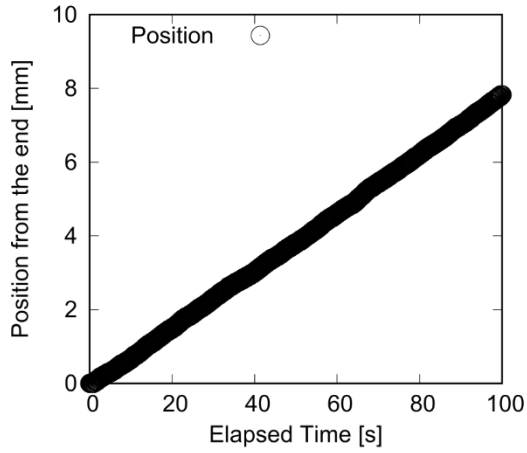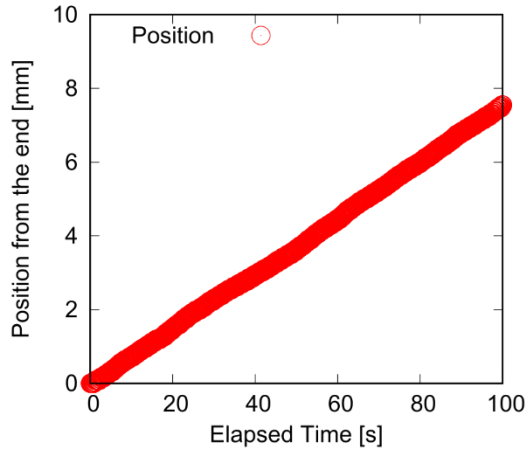
(b) *Yo* = 0.23, P=80 kPa, horizontal

(c) *Yo* = 0.38, P=80 kPa, vertical
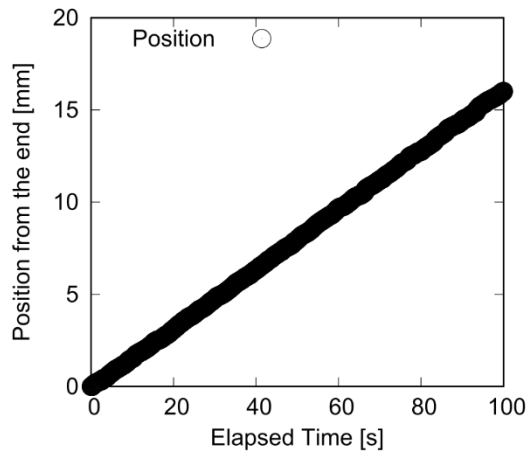
(d) *Yo* = 0.38, P=80 kPa, horizontal
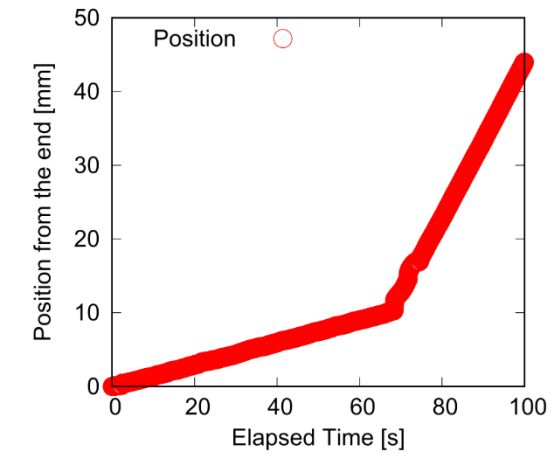
(e) *Yo* = 0.53, P=20 kPa, vertical
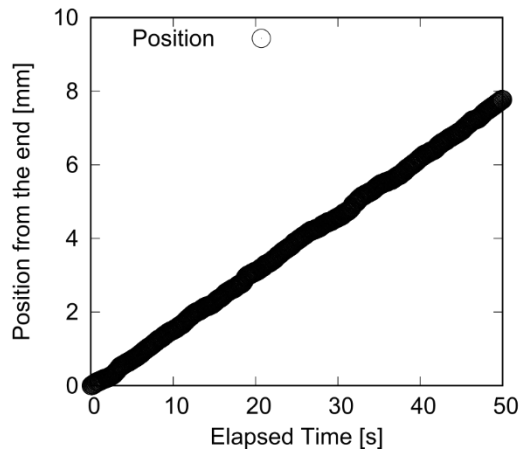
(f) *Yo* = 0.53, P=20 kPa, horizontal
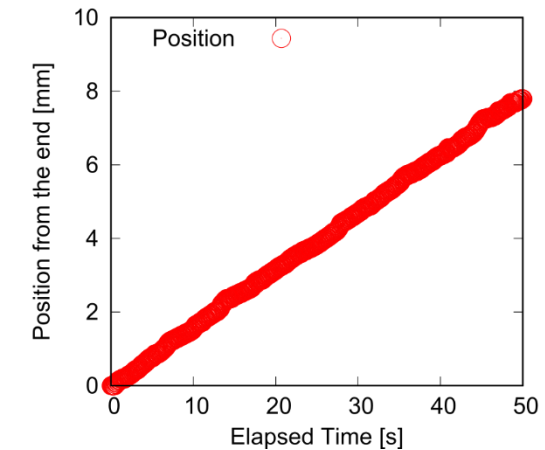
Fig. 3.10. Time-history of the location of the moving burning front. (a) *Yo* = 0.23, *P*=80 kPa, vertical, (b) *Yo* = 0.23, *P*=80 kPa, horizontal, (c) *Yo* = 0.38, *P*=80 kPa, vertical, (d) *Yo* = 0.38, *P*=80 kPa, horizontal, (e) *Yo* = 0.53, *P*=20 kPa, vertical, (f) *Yo* = 0.53, *P*=20 kPa, horizontal.
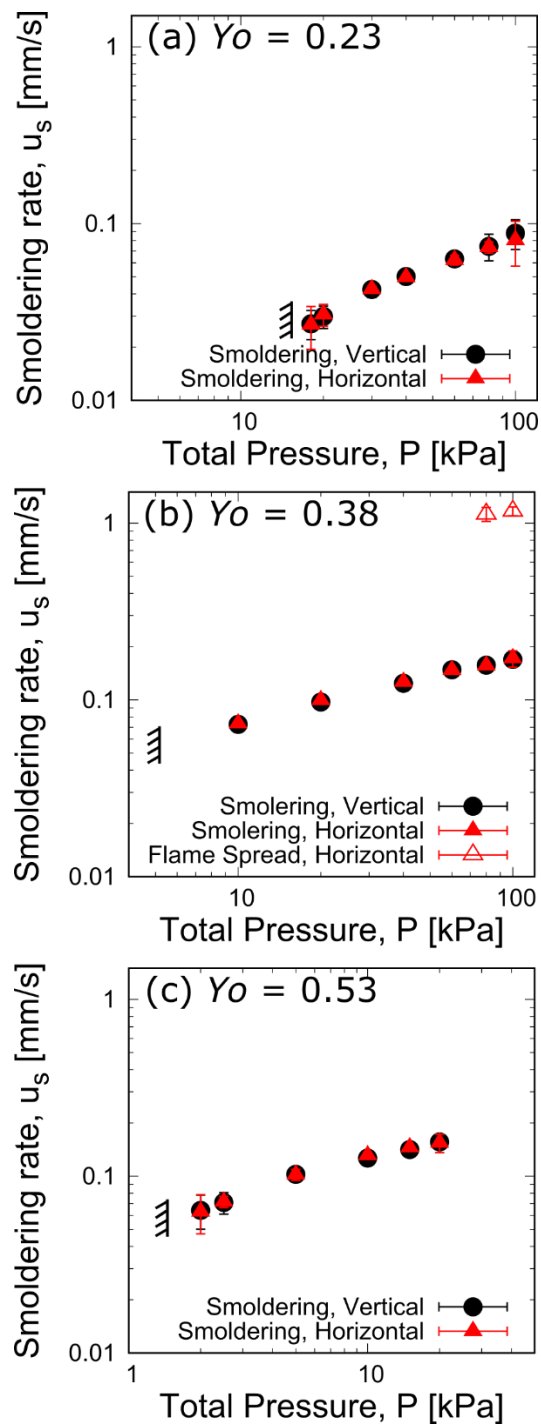
Fig. 3.11. Summary of the measured smoldering rate for the vertical and horizontal biomass stick. (a) Y_O = 0.23, range of the total pressure from 15 kPa to 100 kPa in absolute. (b) Y_O = 0.38, range of total pressure from 10 kPa to 100 kPa. (c) Y_O = 0.53, range of total pressure from 5 kPa to 20 kPa. Solid circle: vertical downward smoldering, Solid triangle: horizontal smoldering, Open triangle: post-transition flame spread.

3.5.3. Temperature in Smoldering

Figure 3.12 and 3.13 compare the measured temperature profiles of the vertical and horizontal cases. For convenience, the calculated gradients of the temperature profiles are also shown. The origin of the horizontal axis is set at the location exhibits the temperature peak. For the case of $Y_O = 0.23$ at 100 kPa (see Fig.3.12 (a) and (b)), the trends of the temperature profile and its gradient are not identical between the vertical and horizontal cases. The value of the gradient peak for both vertical and horizontal cases is nearly identical although the appeared location is different, suggesting that the conductive heating is nearly the constant to lead the identical smoldering rate. Between the gradient peak and the temperature peak (say, oxidative region), it is noted that the temperature gradient in the horizontal case is larger than that in the vertical case, implying that there is the effect of gravity. As approaching to low-pressure (see Figs. 3.12 (c)-(f)), the gradient in the oxidative region for both orientations becomes closer and gentle, then eventually satisfactorily identical to each other (nearly being a plateau profile). Importantly, the same trend can be found in the case of $Y_O = 0.38$ (see Figs. 3.13 (a)-(f)). The difference in the temperature profiles between the vertical and horizontal cases appears more clearly in high oxygen levels. The observed trends are expected to be universal.

Fig.3.14 shows the peak temperatures obtained from the temperature histories. The

measured peak temperatures are plotted against the imposed pressure and compared for the vertical and horizontal oriented cases in Fig. 3.12 for Y_O = 0.23 and Fig. 3.13 for Y_O = 0.38. For Y_O = 0.53, the only peak temperatures are shown in Fig.3.14 (c). Y_O = 0.23, both peak temperatures are different yet have larger errors above 80 kPa, suggesting that it is difficult to say that there is a clear difference between two orientation cases. Below 20 kPa for Y_O = 0.23 (near the extinction limit), the difference in the peak temperatures for both the vertical and horizontal cases seems to be pronounced, however, the uncertainties of the measured temperature are large so that it would be difficult to conclude that there is a clear difference in thermal structure depending on the biomass stick orientation. For Y_O = 0.38, the trends of the peak temperatures against the pressure are nearly identical under the smoldering condition (below 60 kPa). This is because the use of a thin biomass stick achieves reduced-natural-convection environments using the low-pressure method. Therefore, oxygen transport is governed by molecular diffusion in the low-pressure environment in this experiment. For Y_O = 0.53, the trends of the peak temperatures against the pressure is similar to Y_O = 0.23. These peak temperatures have relatively larger errors than the other results. One of the reasons to cause the errors is insufficient coating on the surface of a thermocouple because a R-type thermocouple may have a catalyst effect of platinum on volatiles and combustion products.
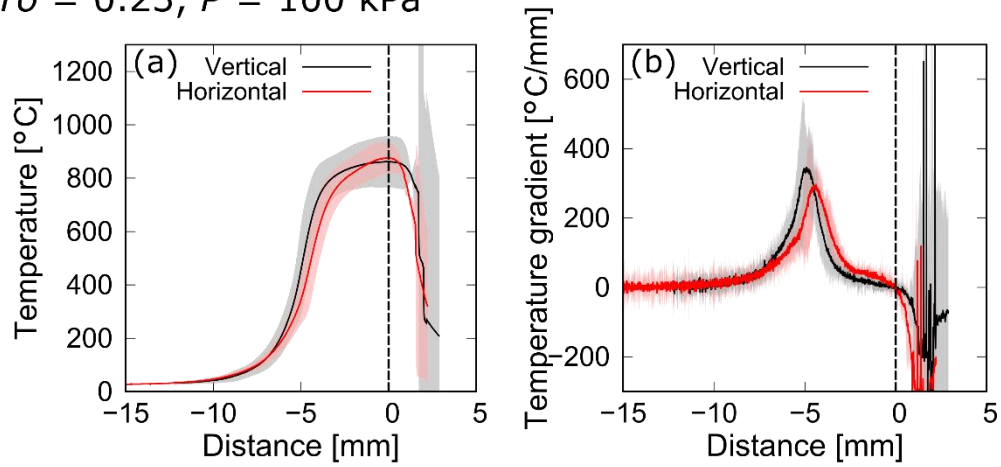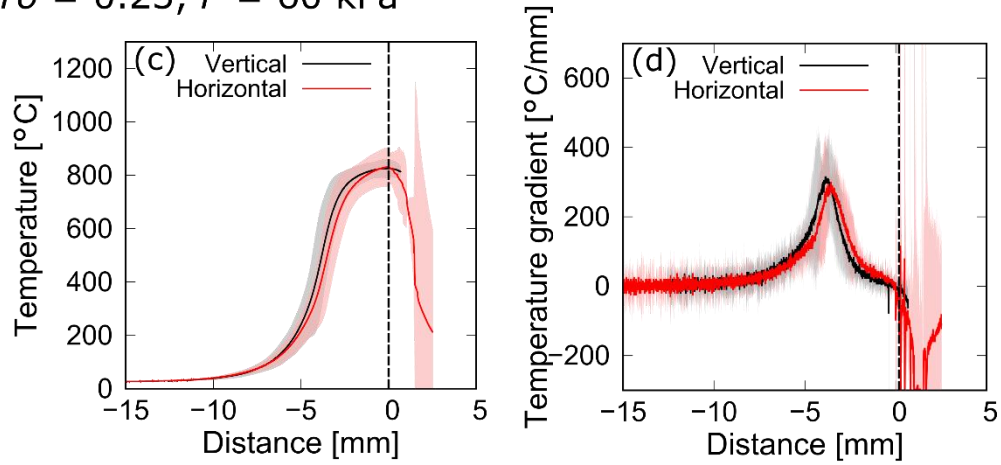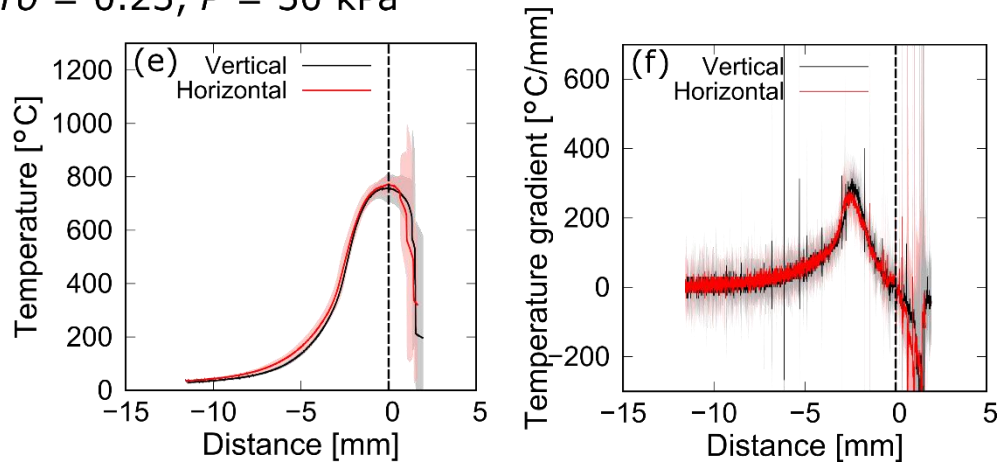
Fig. 3.12. Typical temperature profiles and its gradients along with the vertical and horizontal biomass sticks for Y_O = 0.23. (a), (b), P = 100 kPa, (c), (d) P = 60 kPa, (e), (f) P = 30 kPa. The origin is at the peak temperature. The solid lines show averaged temperature profiles and the shadows show the error bar. Black color means the vertical orientation and red color means the horizontal orientation.
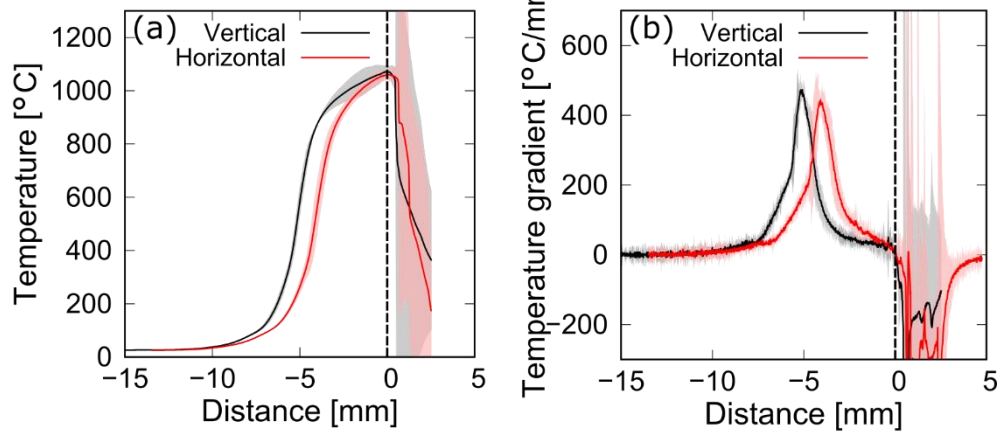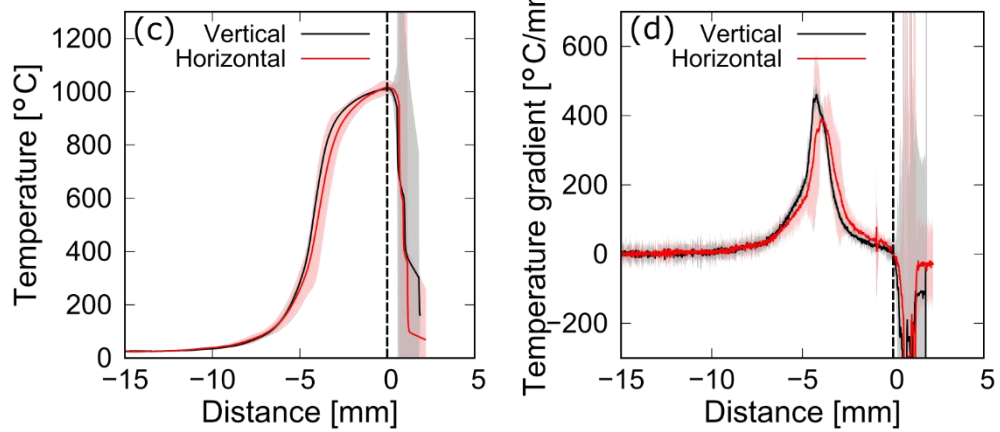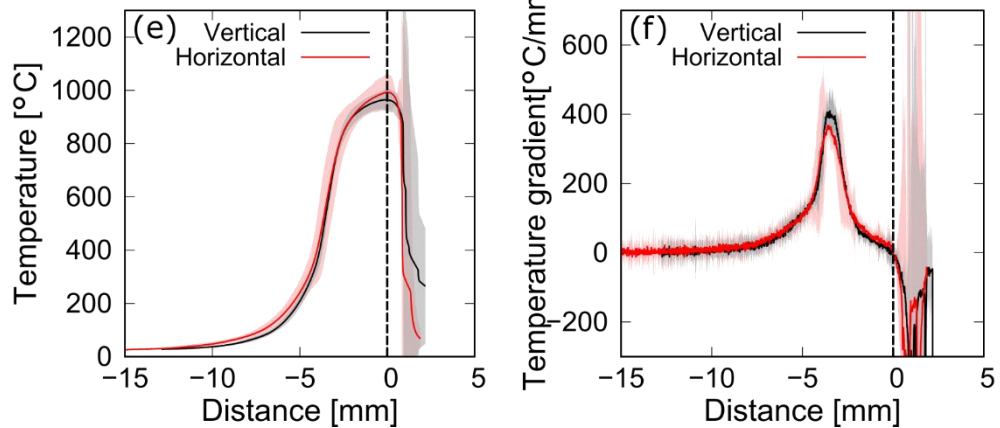
Fig. 3.13. Typical temperature profiles and its gradients along with the vertical and horizontal biomass sticks for Y_O = 0.38. (a), (b), P = 60 kPa, (c), (d) P = 40 kPa, (e), (f) P = 20 kPa. The origin is at the peak temperature. The solid lines show averaged temperature profiles and the shadows show the error bar. Black color means the vertical orientation and red color means the horizontal orientation.
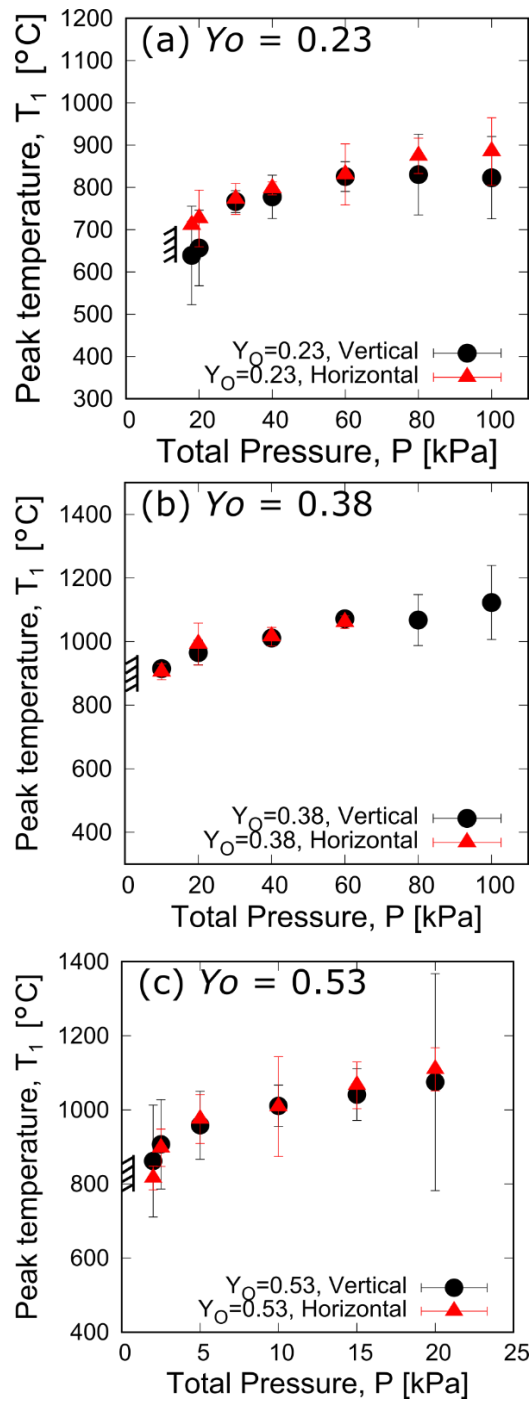
Fig. 3.14. The peak temperature against the adopted pressure along with the vertical and horizontal biomass stick. Solid circle: vertically downward smoldering, Solid triangle: horizontal smoldering. (a) Oxygen mass fraction Y_O = 0.23, range of total pressure from 15 kPa to 100 kPa in absolute. (b) Y_O = 0.38, range of total pressure from 5 kPa to 100 kPa. (c) Y_O = 0.53, range of total pressure from 1 kPa to 20 kPa. For comparison purposes on smoldering status, data at transient conditions are excluded.

Figure 3.15 shows the peak temperatures against the partial pressure of oxygen for all experimental conditions. The peak temperatures for the high oxygen concentration indicate higher temperatures than the lower oxygen concentration. In smoldering combustion, char oxidation reactions are expressed as the power-law of the partial pressure of oxygen [97]. In the experimental condition of the same partial pressure of oxygen, the reaction rates for the various oxygen concentrations would be identical. However, the peak temperatures in the same partial pressure of oxygen are different. It is presumed that the reduced-natural-convection environments decrease the heat losses from the reaction region.
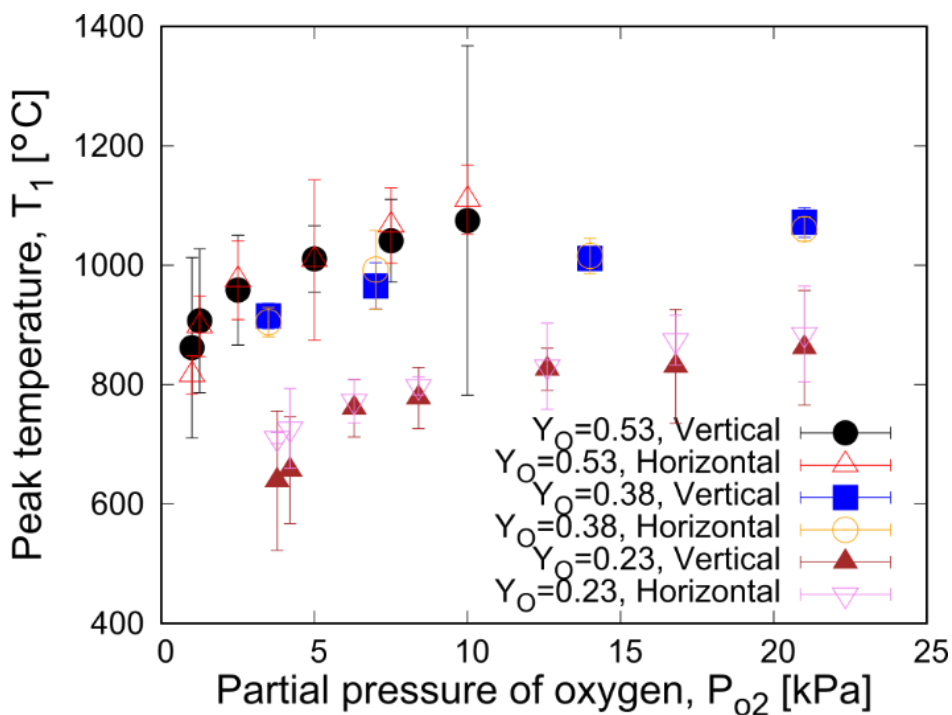
Fig. 3.15. The peak temperatures against the partial pressure of oxygen for all experimental conditions.

3.6. Analysis of the Smoldering Region

3.6.1. Effect of Reducing Pressure on the Smoldering Region

 Let us introduce a simple modeling concept to discuss the effect of reducing pressure on the smoldering combustion. Fig. 3.16 depicts the schematic diagram of a structure in the oxidative region. Additional assumptions are made to obtain the qualitative trend of the measured temperature profile; such as (1) no heat loss toward perpendicular to the axis; (2) no overlapping reactions between char oxidation and both pyrolysis and oxidative degradation, so that the only char oxidation is considered in the oxidative region; (3) the local thermal equilibrium between the solid and the gases is achieved.
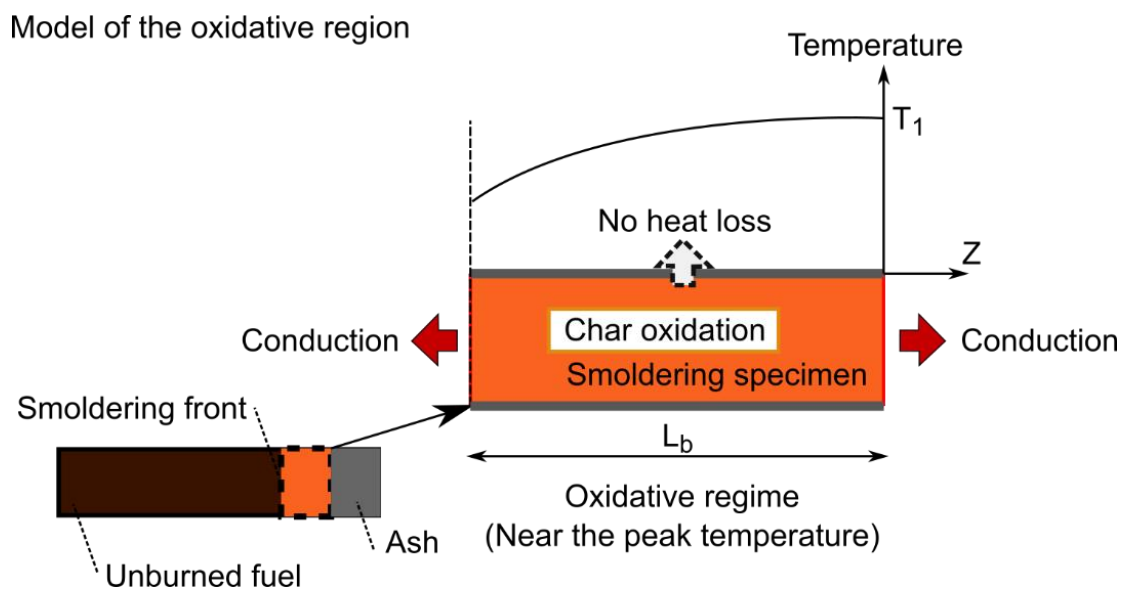
Fig. 3.16. The schematic diagram of the thermal structure of the oxidative region without the convective heat loss.

Then the simplified energy equation in the oxidative region, the species equation, and the kinetic model of the char oxidation referring to Ref. [98] and [99] are expressed as follows;

$$\rho_c c_c u_s \frac{dT_s}{dz} = (k_c + k_r)\frac{d^2 T_s}{dz^2} + Q\rho_c \dot{\omega} \,, \tag{3.23}$$

$$\rho_c u_s \frac{dZ_c}{dz} = -\rho_c \dot{\omega} \,, \tag{3.24}$$

$$\dot{\omega} = A\left(\frac{X_o P}{101.3}\right)^n Z_c{}^m \exp\left(-\frac{E}{RT_s}\right), \tag{3.25}$$

where averaged (volumetric) density of char ρ_c is defined by $(1-\varphi)\rho_s + \varphi\rho_g$, φ is the porosity of the biomass stick [-], ρ_s is the density of solid [kg/m^3], averaged (volumetric) specific heat of char c_c is defined by $(1-\varphi)c_s + \varphi c_g$, c_s is the specific heat of solid [J/kg·K], c_g is the specific heat of gas [J/kg·K], k_c is the effective conductivity of the biomass stick, k_r is the coefficient [W/m·K] (defined as a radiant conductivity, $k_r = 4Fd\sigma T_m{}^3$, [73,100]), F is a radiation exchange factor [-], d is a particle diameter [m], σ is the Stefan-Boltzmann constant [W/m^2·K^4] and T_m is arithmetic mean temperature between the peak temperature of the smoldering Y_c is the mass fraction of char [-], Z_c is conversion of mass losses defined as $1 - (m - m_f)/(m_0 - m_f)$, m is the current mass [kg], m_f is the final mass [kg], m_0 is the initial mass [kg], A is a pre-exponential factor [1/s], X_o is the oxygen concentration

in the ambient gas [-], P is the adapted pressure in the vacuum chamber [kPa], n and m

are the reaction order [-], E is the activation energy [kJ/mol], R is the universal gas

constant [$J/mol\ K$]. Note that the reaction expression and constants are slightly modified

and adjusted to fit the present problem. Note that the Eq. (3.25) is slightly modified from

the original [98] by replacing the oxygen concentration to the partial pressure of oxygen

to include the pressure effect.

The boundary conditions to solve Eqs. (3.23) - (3.25) are $T_s = T_1$ at $z = 0$ and $T_s \to$

T_0 at $z \to -\infty$. To make the Eqs. (3.23) – (3.25) dimensionless, the following non-

dimensional variables are introduced:

$$\Theta(\xi) = \frac{T_s - T_0}{T_1 - T_0}, \tag{3.26}$$

$$\xi = \frac{\rho_c c_c u_s}{(k_c + k_r)} z, \tag{3.27}$$

$$Q^* = \frac{Q}{c_c(T_1 - T_0)}, \tag{3.28}$$

$$\beta = \frac{E}{RT_1^2}(T_1 - T_0), \tag{3.29}$$

$$\Lambda = \frac{(k_c + k_r)}{\rho_c c_c u_s^2} A\left(\frac{X_o P}{101.3}\right)^n \tag{3.30}$$

where Q^* is the non-dimensional heat release [-], and Λ is the non-dimensional

Damkohler number [-]. Using these dimensionless variables and parameters and

substituting Eq. (3.25) into Eqs. (3.23) and (3.24), then obtain

$$\frac{d\theta}{d\xi} = \frac{d^2\theta}{d\xi^2} + \Lambda Q^* Z_c^m \exp\left(-\frac{T^*}{\theta_0^* + \theta}\right),$$ (3.31)

$$\frac{dZ_c}{d\xi} = -\Lambda Z_c^m \exp\left(-\frac{T^*}{\theta_0^* + \theta}\right),$$ (3.32)

where T^* is defined as $T^* = E/R(T_1 - T_0)$, θ_0^* is $\theta_0^* = T_0/(T_1 - T_0)$. To eliminate

the reaction term, the linear combination of them is applied to Eq. (3.31) and (3.32). After

the coupled equation is integrated over ξ and the boundary conditions are used, the

following relation is obtained

$$Z_c = 1 - \theta + \frac{d\theta}{d\xi}.$$ (3.33)

Substituting Eq. (3.33) into Eq. (3.31), then Eq. (3.31) becomes

$$\frac{d^2\theta}{d\xi^2} - \frac{d\theta}{d\xi} + \Lambda\beta Q^*\left(1 - \theta + \frac{d\theta}{d\xi}\right)^m \exp\left(-\frac{T^*}{\theta_0^* + \theta}\right) = 0.$$ (3.34)

Employing the Runge-Kutta method with the initial condition ($\theta = 0.99$ at $\xi = 0$),

calculated profiles are shown in Fig. 3.17, with the measured temperature profile for Y_O

$= 0.38$ and $P = 60$ kPa in the horizontal orientation for comparison purpose. The physical

properties for this calculation are shown in Table 3.3. This figure shows that the predicted

profile adjacent to the temperature peak is matched well with the measured one

satisfactorily for the only char-oxidation region. The trend of the predicted profile

becomes far from the measured one over $\xi < -4$, where the pyrolysis reaction is not taken into account. With this respect, it is safely said that the model can predict at least the temperature gradient near the peak location.
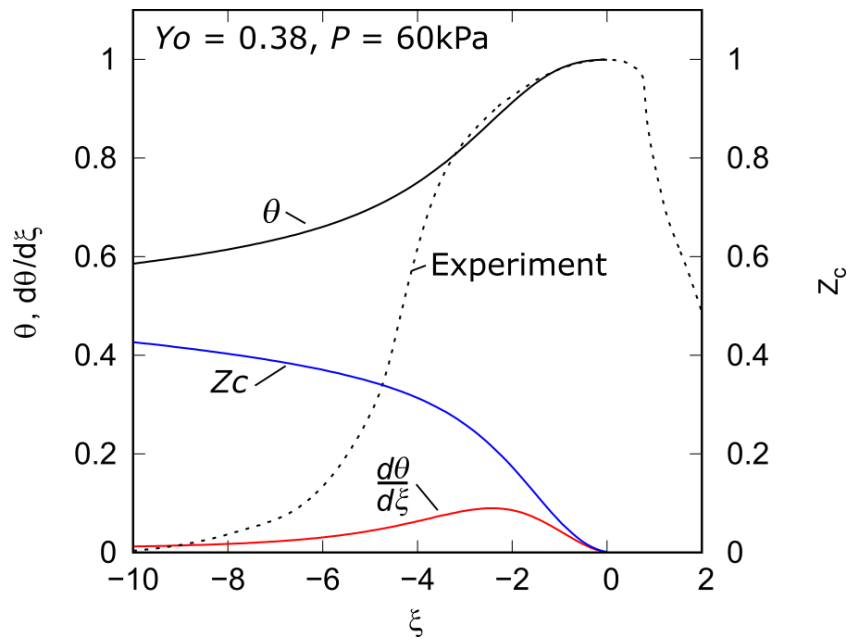
Fig. 3.17. The comparison between the experimental and theoretical profiles in the oxidative region. The experimental data is for Y_O = 0.38 and P = 60 kPa in the horizontal case. The dashed line shows the dimensionless temperature profiles based on the measured temperature history. Solid lines show the calculated profiles of dimensionless temperature and the mass conversion of biomass sticks.

Fig. 3.18. compares the predicted temperature profile only around the temperature peak at various pressure levels. To focus on the local profile near the temperature peak, only the (expected) region at – 0.01 m < x < 0 mm is shown. The model predicts the decreasing

trend of the temperature gradient when the adopted pressure decreases. As pressure

decreases, eventually, the gradient becomes quite gentle as shown in the measured one.

The gentle temperature gradients mean that the heat release rates in the oxidative region

decrease with the decrease of the pressure. Thus, when the heat losses are taken into

account in the model, the temperature gradients in the oxidative region will be affected

depending on the pressure because the effect of the heat losses on the weak reaction region

is large.
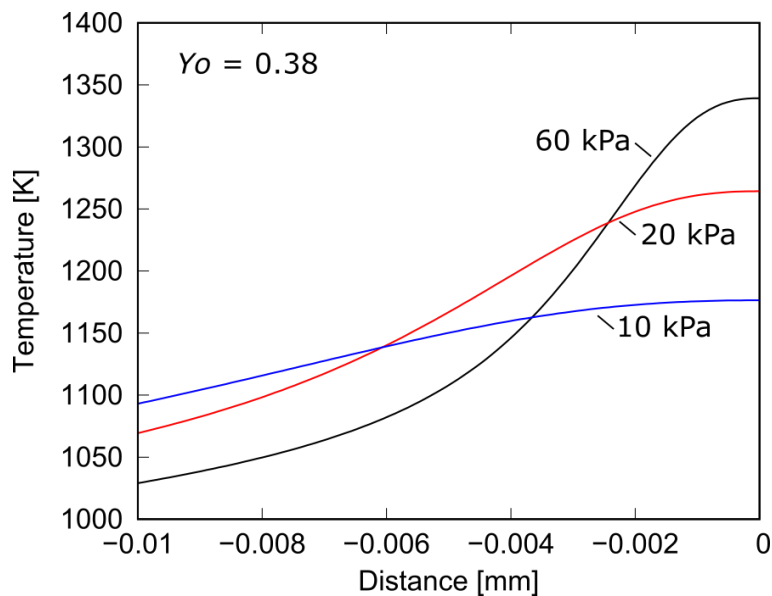
Fig. 3.18. Prediction of the temperature profiles in the oxidative region for Y_O = 0.38.

Table 3.3. Physical properties

Property	Unit	Value	Note
ρ_s	kg/m^3	1670	Ref. [101]
ρ_g	kg/m^3	1.166	Ref. [102]
c_s	J/kg·K	1740	Ref. [101]
c_g	J/kg·K	1006	Ref. [102]
φ	-	0.4	Estimated value
Q	MJ/kg	10.0	Estimated value from Ref. [98]
E	kJ/mol	125	Ref. [99]
A	s^{-1}	4.8	Determined value to fit the calculation to the experimental result
n	-	0.53	Ref. [99]
m	-	0.49	Ref. [99]
u_s	mm/s	0.00014	Measured value
T_1	K	1342	Measured value
T_0	K	300	Measured value

3.7. Conclusions

The smoldering behavior of thin biomass stick under reduced pressure was experimentally investigated for the vertically- and horizontally-oriented cases at various oxygen concentrations, aiming to examine the influence of a low-pressure environment on smoldering combustion. In a low-pressure environment, the smoldering rates, peak temperatures, and the thermal structures are identical for both vertical and horizontal cases. The fact implies that natural convection is suppressed and oxygen transport is governed by molecular diffusion. Using the biomass stick with 2 mm diameter and the total pressure below 60 kPa, the reduced-natural-convection environment was attained. Therefore, the low-pressure method can be adapted to examination for the extinction limit of smoldering without disturbance of natural convection and can improve the conventional method with poor reproductivity of observation for the limiting behavior of smoldering.

Chapter 4

4. Transition from Smoldering to Extinction

4.1. Introduction

This section aims to experimentally investigate the transition from smoldering to extinction using a low-pressure environment. In the standard atmospheric pressure (101.3 kPa) of air, one experimental method applies a forced flow over the smoldering materials to supply oxidizer into the smoldering region [85]. However, it is hard to observe the extinction limit of smoldering material through conventional experiments because of the presence of buoyancy-driven flows. The other method is a smoldering experiment in a low-oxygen environment. Reducing the oxygen level can cause the extinction of smoldering [50]. In recent research of smoldering in the natural environment [80], it has been observed that smoldering fronts in shallow or deep peat have different dynamics. Near the surface of peat, an adequate amount of oxygen is supplied into the smoldering fronts but higher heat losses affect the smoldering region. On the other hand, deep fronts are in low oxygen levels but insulated from heat losses. Since pyrolysis and oxidation reactions compete depending on oxygen levels [103], the heat balance between heat losses and heat release rates in smoldering fronts play a key role in smoldering dynamics near the extinction limit. Therefore, both chemical kinetics and transport phenomena should

be discussed to understand the smoldering dynamics near the extinction limit.

In this experiment for smoldering extinction, oxygen concentrations and pressure levels inside the vacuum chamber were selected as the experimental parameters to vary the controlling mechanisms of smoldering near the extinction limit. The extinction mechanisms of smoldering materials are examined by the burning conditions and the obtained propagation rates of smoldering front and the temperature profiles of smoldering materials.

4.2. Experimental Setup
4.2.1. Experimental Apparatus

A schematic diagram of the experimental setup is shown in Fig.1. The experiment on a downward burning incense stick was conducted in a low-pressure chamber that was 500 mm × 650 mm in cross-section and 770 mm in height. A 2-mm-thick incense stick was used as the biomass stick (Nihon Kodo Co., Sasara Binchotan). The stick consists of mainly the sawdust and has homogenous properties of porosity and composition due to commercial products. The bottom end of the stick is held vertically on a supporter made of aluminum alloy. The length to burn is 100 mm from the end of the supporter. A 0.2 mm-diameter hole is made at 40 mm from the top of the biomass stick and an R-type thermocouple (0.050 mm in diameter, 0.10 - 0.15 mm of junction size) is embedded into

the hole to measure the temperature history inside the burning stick (see Fig.4.1). Before experimenting, the biomass sticks were dried in an oven at 40 °C for more than two hours to remove the effect of moisture content.
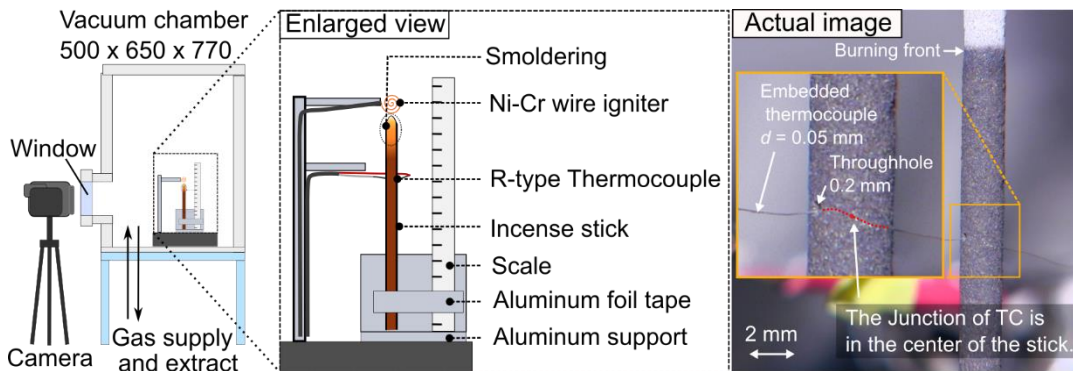
Fig. 4.1. Schematic of the experimental setup and a photo of the burning incense stick and the embedded thermocouple.

4.2.2. Measurement Methods

The movement of the smoldering front was recorded by a video camera (Canon iVIS HF G10, interlace 24 fps, less than 1/24 seconds in exposure time) through the observation window (Fig.4.1). The frames of interest were extracted from the recorded data for image analysis. Using the image processing software ImageJ Fiji [96], the positions of the smoldering front were extracted from each image and the smoldering rate was then calculated. Time zero ($t = 0$ sec) is defined as the moment when the smoldering front passes 3-mm below the initial top surface. The experiment was repeated at least three times for each adapted pressure.

Measurement of the temperature in the center of the biomass stick was conducted as shown in Fig.4.1. A 0.2 mm-diameter hole was made at 15 mm from the top of the biomass stick to avoid the influence of the igniter and then an R-type thermocouple (0.05 mm in diameter, 0.10 - 0.15 mm of junction size) was embedded into the hole. The temperature history was converted to a temperature profile by the same method described in Section 3.3.3. The origin is set at the peak temperature along the axial axis and the negative sign corresponds to the preheat zone (virgin fuel).

4.3. Experimental Results
4.3.1. Combustion Mode

Direct images of the burning biomass sticks at the represented conditions are shown in Fig.4.2. This series of experiments was conducted under the mass fraction of oxygen, Y_O = 0.53 at various imposed pressures at P = 60, 40, 15 and 2.5 kPa, respectively. As seen in (a) P = 60 kPa, the general flame spread can be identified because there is a rich oxidizer for continuous flaming. As the gaseous flame moves downward rapidly, biomass stick at post-flame zone burns continuously (surface oxidation). The brightness of the burning biomass stick seems almost constant, implying that oxygen supply is fairly uniformly made into the biomass stick in the present system.

When the pressure was reduced at P = 40 kPa, the transition from smoldering (non-

flaming) to flame spread was identified. Followed by the successful ignition, first, the

smoldering lasts for a while, then transiting to flaming, finally the flame spreading. The

reproducibility of the transient phenomenon was checked three times to confirm that the

transient point was nearly constant (12 mm – 14 mm top from the surface). This is

interesting and of note that the transient behavior might be precisely studied by adopting

the low-pressure technique.

As the pressure is further reduced at $P = 15$ kPa, the only smoldering was experienced

without any transition. In contrast with the case of the flaming, luminosity becomes much

less and the luminous part is only limited at the vicinity of the top end. It is identified that

the residual ash tends to cover the burning zone, which creates difficulty in identifying

the exact area of the luminous zone in a precise manner. Such a trend is more severe at

near-extinction limit: $P = 2.5$ kPa. In this sense, if only on optical measurement for

temperature is adopted it is not a good way to extract the smoldering characters, e.g.

preheating zone or temperature profile.

Figure 4.3 shows the time-variation of the position of the burning front for the same

burning conditions shown in Fig. 4.2 ($Yo = 0.53$, $P = 60, 40, 15$ and 2.5 kPa). The slope

indicates the rate of flame spread or smoldering, indicating that steady burning is achieved.

At 40 kPa (Fig.4.2 (b)), where the transition occurs, both rates for smoldering (before

transition) and flame spread (after transition) are found to be nearly constant, suggesting

that the burning mode is completely switched from one to the other at the transition. It is

important to note that the transition is quite solid, implying that controlling the transition

is fairly possible by varying the pressure.
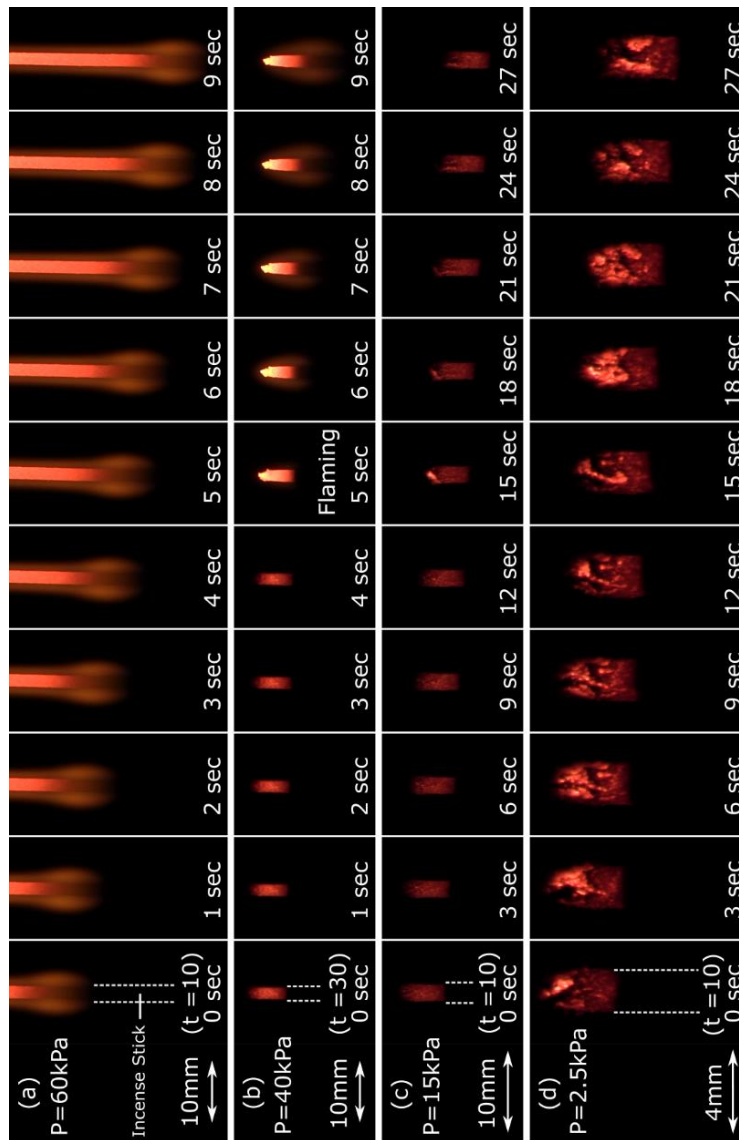
Fig. 4.2. Typical sequential images of burning biomass stick with various ambient pressures at (a) P=60 kPa, (b) P=40 kPa, (c) P=15 kPa and (d) P=2.5 kPa under oxygen mass fraction Y_O=0.53.
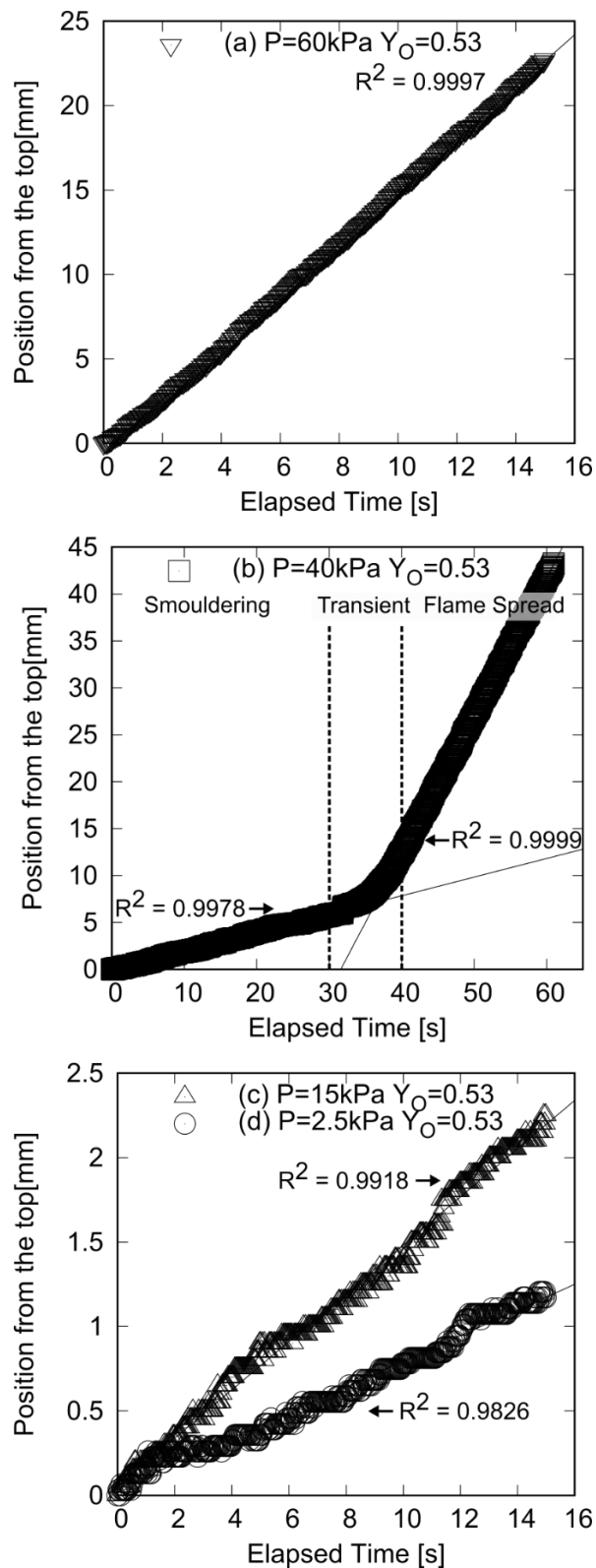
Fig. 4.3. Time-history of the location of the downwardly moving burning front. (a) *P*=60 kPa, (b) *P*=40 kPa, (c) *P*=15 kPa, and (d) *P*=2.5 kPa under oxygen mass fraction *Yo*=0.53.

4.3.2.Propagation Velocities

 Another series of experiments have been conducted under various oxygen mass fractions,

Yo = 0.20, 0.23, 0.33, 0.53 and 1.0, at various chamber pressure levels ranging from 1.0

to 90 kPa. The results are summarized in Fig.4.4. The flame spread was experienced only

when the oxygen mass fraction was set over 0.53. On the contrary, only smoldering was

experienced only when the oxygen mass fraction was set below 0.33. In the transient

regime, smoldering was first observed after ignition and then transition to the flame

spread. Burning rates decreased with decreasing the ambient pressure whereas they

increased with increasing oxygen mass fraction. The effect of oxygen on burning rates

was found to be more sensitive than that of imposed pressure except for the extinction

point. This trend is fairly consistent with the fact found by Moussa [51]. The sensitivity

of the burning rate against pressure was found only at the near extinction limit and

pronounced under a lower oxygen concentration field. The lower limiting value of the

burning rate seems rather constant when the oxygen mass fraction is lower than Yo =0.33,

then goes up when the oxygen mass fraction increases. At high oxygen mass fraction (Yo

~ 1.0) ambient condition is not very accurate due to the lack of accuracy of the pressure

gauge (we will upgrade in the future). Nevertheless, the extinction point for Yo =0.53 is

dependable and repeatable. Hence, measured data of Yo =1.0 will not be used for the

following discussions. From now on, we shall focus on the smoldering behavior in detail.
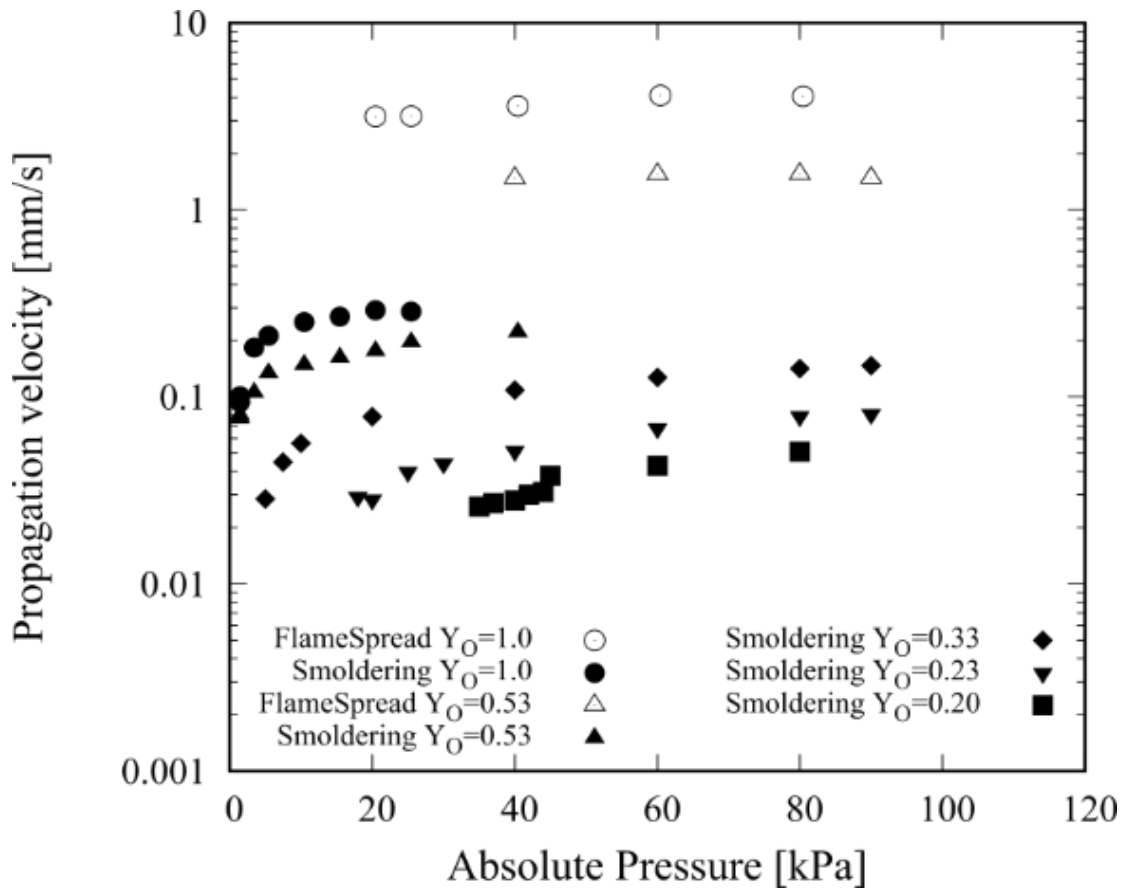
Fig.4.4. Propagation rate against absolute pressure for Yo=0.20, 0.23, 0.33, 0.53 and 1.0.

4.3.3. Peak Temperatures

Based on the signal from a fine thermocouple embedded in the biomass stick, precise temperature profiles during the smoldering event were obtained. The temperature profiles are shown in Fig. 4.5. The trends of the temperature in the smoldering region are similar except for the region near the peak temperature. The plateau regions near the peak temperature are wider in higher oxygen concentrations.

Figure 4.6 shows the variation of the peak temperature in a smoldering event under Yo

= 0.20, 0.23 and 0.53. It is found that the overall trends are quite similar to the trends of

the smoldering rate in Fig. 4.4. When the oxygen mass fraction is relatively large ($Yo >$

0.23), the sudden temperature drop is identified near the extinction limit. This trend failed

to be observed at $Yo = 0.20$, potentially because the heat loss to the thermocouple might

play a role.

Figure 4.7 shows the relationship between the smoldering velocity (Fig. 4.4) and

reciprocal of peak temperature (Fig.4.6). The dashed line is an estimated function by the

method of least squares. The estimated exponential function is good agreement in the

plotted data and confirms that the smoldering velocity fairly shows an Arrhenius-like

temperature dependency. This fact suggests that the peak temperature is well-correlated

to the smoldering velocity and could be considered as the system-controlling parameter

in the present system.
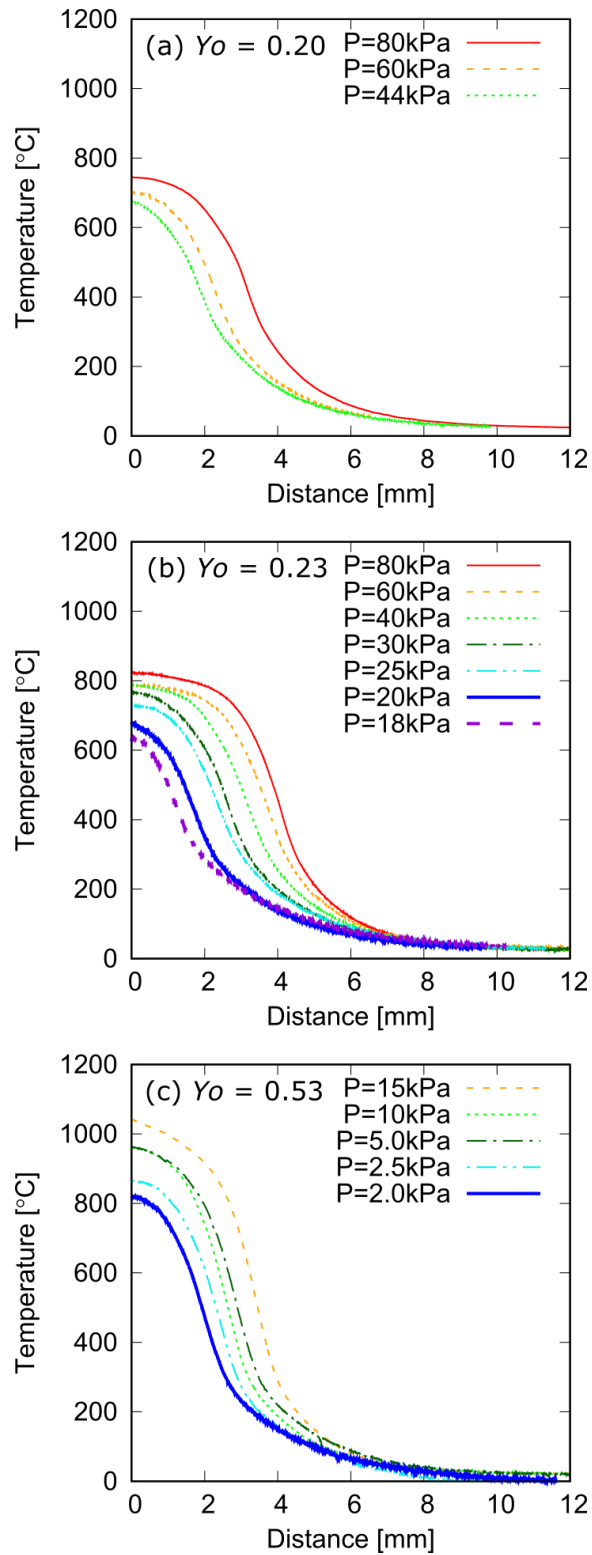
Fig. 4.5. Measured temperature profile ahead of the peak location. (a) *Yo* = 0.20, (b) *Yo* = 0.23, and (c) *Yo* = 0.53.
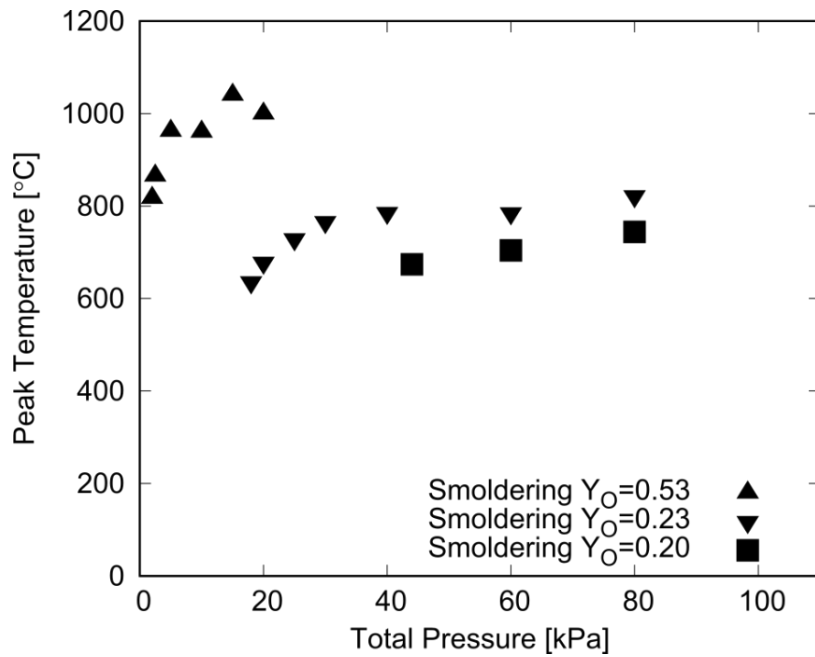
Fig. 4.6. Peak temperature against the imposed pressure, *Yo* = 0.20, 0.23 and 0.53.
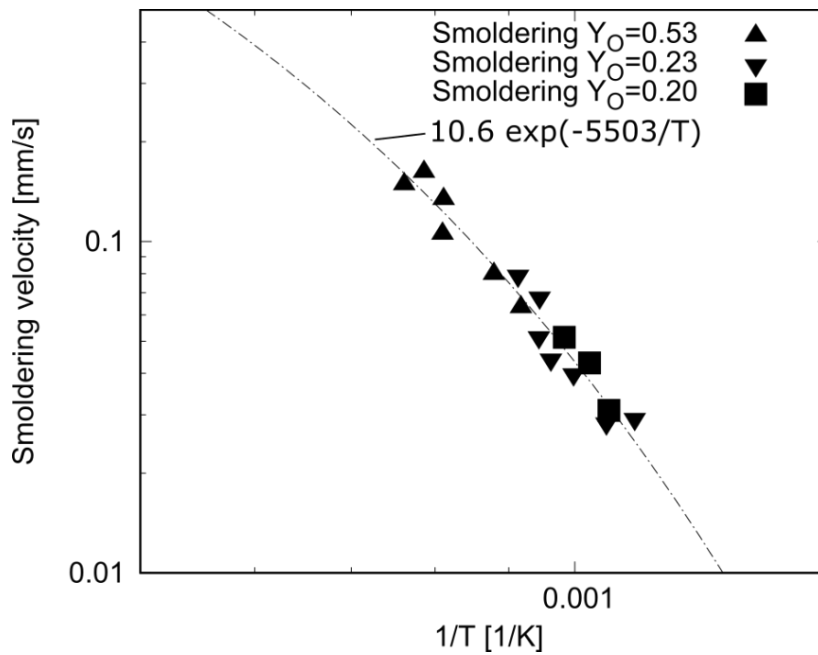
Fig. 4.7. Relationship between smoldering velocity and reciprocal temperature, *Yo* = 0.20, 0.23 and 0.53.

4.4. Discussion

4.4.1. Extinction Limits

The combustion modes and the experimental conditions are summarized in Fig.4.8. For higher oxygen concentrations, the extinction limits seem to be along the line of $P_{O2} = 1.0\ kPa$. However, below 0.33 in mass fraction, the extinction limits are not agreed in the line of $P_{O2} = 1.0\ kPa$.
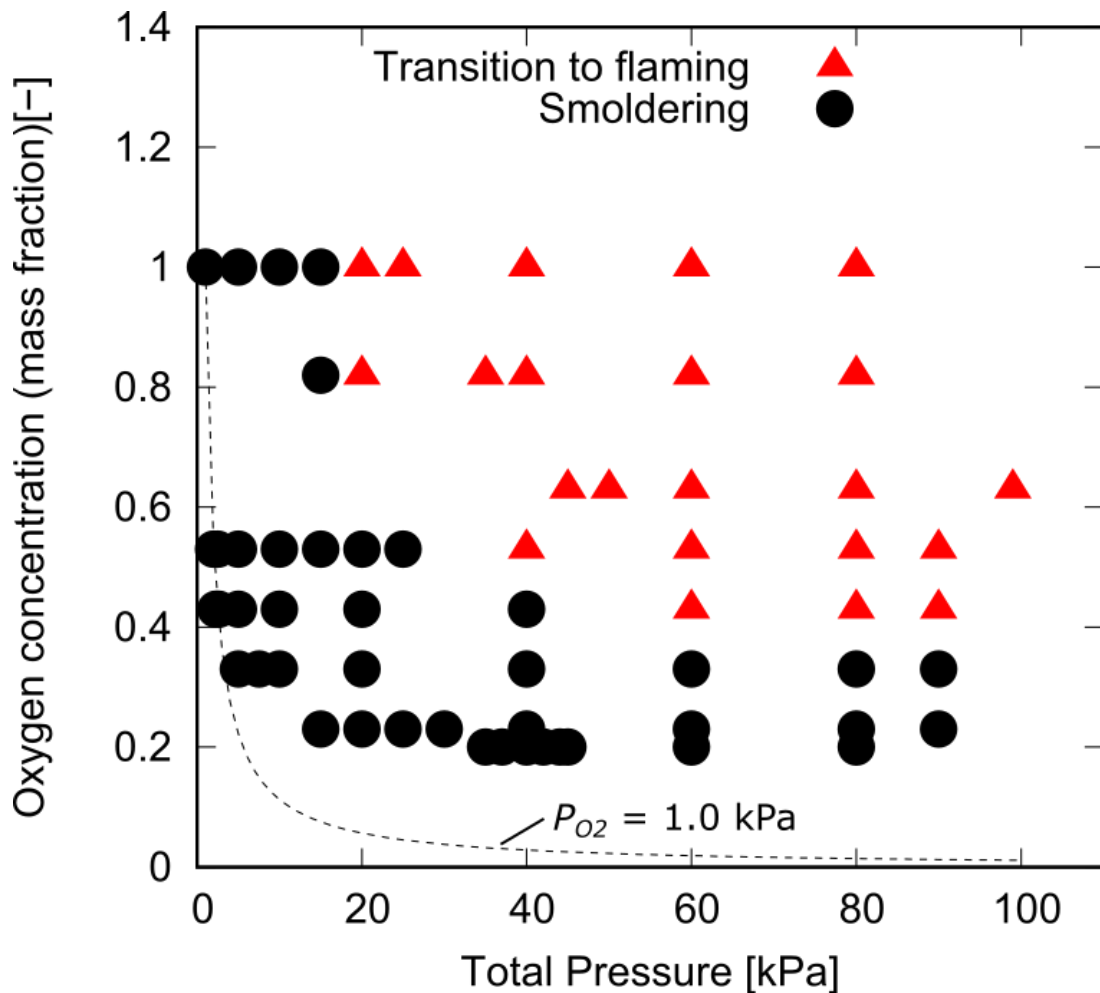
Fig. 4.8. Mapping combustion conditions.

Figure 4.9 shows the relationship between propagation rates and total pressure for each oxygen concentration. It seems that the extinction occurs at the "critical" propagation velocity when oxygen concentration is below 0.4. However, the trend of the propagation rates in extinction limit changes. The propagation rates in the extinction limit seem to be depending on total pressure, $u_S \propto P^{-n}$.

According to research on reverse combustion in a packed bed of wood particles done by Fatehi and Kaviany [73], two extinction limits were obtained. One is the extinction limit in the oxygen-limited regime, the other is in the fuel-limited regime. In the oxygen-limited regime, the temperature in the reacting region is sufficiently high, whereas oxygen supply is deficient so that the oxygen supply rate determines the reaction rate. For our experiment results, the range in which oxygen concentration is above 0.4 seems to be equivalent to the oxygen-limited regime because the temperature in the reaction region increases with the increase of oxygen concentrations. Moreover, in the higher oxygen levels, the smoldering velocity at the extinction limit is depending on the total pressure, which means that oxygen transfer by natural convection affects the smoldering velocity. Therefore, the extinction limit in the higher oxygen levels is determined by a function of total pressure.

On the other hand, the range in which oxygen concentration is below 0.3 is considered as a kinetics-limited regime. In the kinetic-limited regime, total pressures at the extinction

limit are relatively higher than the cases of higher oxygen levels, which implies that

oxygen supply by natural convection is adequate, but the effect of heat losses on the

reaction region becomes dominant due to the low oxygen concentrations. Consequently,

the temperatures in the reacting region in lower oxygen concentrations are lower than the

case of higher oxygen concentrations. Therefore, the extinction limit in the lower oxygen

levels is independent of total pressure.
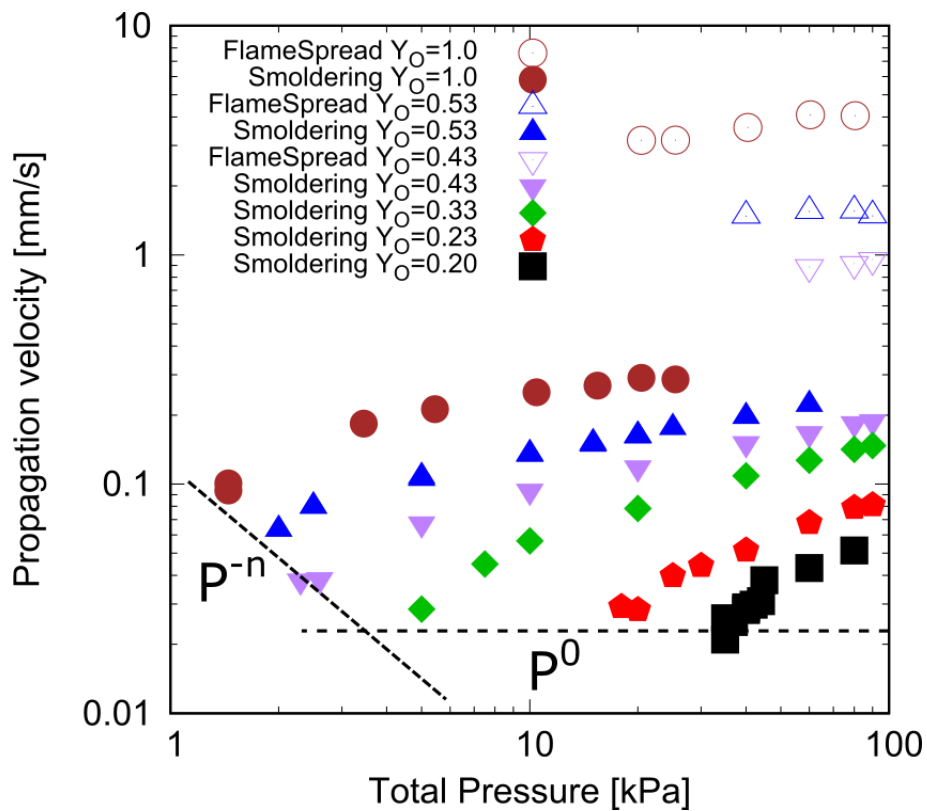
Fig. 4.9. Relationship between propagation rates and total pressure.

4.5. Conclusions

An experiment on smoldering combustion was conducted in the burning conditions with various ambient pressure and oxygen concentrations using a thin-rod biomass stick (incense stick). The extinction limits were obtained clearly. It seems that the extinction occurs at the "critical" propagation velocity when oxygen concentration is below 0.4. However, the trend of the propagation rates in extinction limit changes. The propagation rates in the extinction limit seem to be along $u_S \propto P^{-n}$, where the range of exponent n is $1 < n < 2$. Based on the experimental results, the extinction limits can be classified by the oxygen-limited regime and transport-controlled regime. The range in which oxygen concentration is above 0.4 seems to be equivalent to the oxygen-limited regime, where the temperature in the reaction region is high enough so that the oxygen is controlling factor to maintain the heat release reaction to sustain the smoldering. In the extinction limit, it is well-described as the constant partial pressure of oxygen, suggesting that the limiting factor is the amount of oxygen in the field to provide the surface reaction (exothermic) reaction. The reason why the relatively faster smoldering velocity than the reaction rate is caused by the balancing temperature at the reaction region. We could observe that the smoldering velocity is well-correlated to the temperature at the reaction region even at the limit (see Fig. 4.6). This fact implies that the increase of smoldering

velocity is due to the higher temperature at the reaction regime.

On the contrary, the range in which oxygen concentration is below 0.4 is considered as transport-controlled regime at which the limit is insensitive to the adopted oxygen concentration. Nevertheless, the limit is well-described as the nearly constant smoldering velocity, suggesting there exhibits the nearly constant temperature of the reaction region. However, it is important to notice that the limit at lower oxygen concentration (say 0.2) gives higher partial pressure of oxygen as compared to the ones at the higher oxygen concentrations (say 0,23 or 0.33). Namely, heat release is expected to be larger for the former case than the latter. Nevertheless, the temperature at the limit is constant. Considering all together, only the heat loss depending on the total pressure can be the cause to induce such a feature in the limiting condition. In this sense, this limit can be called a "transport-controlled regime".

Chapter 5

5. Transition from Smoldering to Flaming

5.1. Introduction

This chapter aims to experimentally investigate the transition from smoldering to flaming using a low-pressure environment. Many researchers have investigated the transition to flaming in the forward smoldering experiment since Ohlemiller investigated the transition from smoldering and flaming in cellulosic insulation [82]. The Ohlemiller's study inferred that the smoldering front is kinetically limited so that the heated gases cause the transition to flaming in forward smoldering because the smoldering region is highly responsive to temperature. On the other hand, a few researchers observed transition to flaming from smoldering except the forward smoldering cases [51,81]. Moussa examined the smoldering behavior of a cellulosic material mounted horizontally inside a chamber. In the burning conditions of higher oxygen concentrations and partial pressure of oxygen, the transition to flaming was observed during the horizontal smoldering in natural convection. Rein mentioned that the upward smoldering in a pile of fuel can lead to the transition to flaming when the smoldering front approach to or reach at the free surface [39]. Aldushin et al. studied the possibility of a transition from reverse smoldering to flaming in polyurethane foam by numerical simulation [83]. They reproduced the

transition to flaming by adding an extra oxidizer to participate in the char-oxidation

reaction, which causes the temperature to rise until the gaseous reactions started. However,

it was not clear what the dominant factor was to cause the transition to flaming from

reverse smoldering in natural convection. To answer this unresolved question, we

employed a low-pressure environment to control chemical kinetics and transport

phenomena in smoldering combustion under natural convection. By suppressing the

disturbance of natural convection to the smoldering region, uncertainty in the experiments

for the transition to flaming, for example, the location where the transition to flaming

occurs, can be removed. The mechanisms of the transition to flaming from reverse

smoldering and its dominant factors are examined using the low-pressure method in this

section.

5.2. Experimental Setup
5.2.1. Experimental Apparatus

  A schematic diagram of the experimental setup is shown in Fig.5.1. The experiments of

a smoldering test biomass stick made of biomass were conducted in a vacuum chamber.

The chamber size is 500 mm × 650 mm in the cross-section and 770 mm in height. The

procedure of the experiment is in the same manner as Section 3.2. A dried incense stick

(Nihon Kodo Co., Sasara Binchotan) was adapted as the fuel (biomass) biomass stick.

The adapted pressure range was from 10 kPa to 100 kPa to find the range of transition from smoldering to flaming. The adapted oxygen levels were 0.23, 0.53, 0.63, and 0.83 in mass fraction, Yo [-].

A nichrome wire ignitor was used to ignite the biomass sticks. The tip of the ignitor touched on the top end of the biomass sticks and then the ignitor was turned on at 30 W. The heating time to ignite the biomass sticks was adjusted to between 15 and 25 seconds because the minimum ignition time increases with the decrease of oxygen level. After turning off the ignitor, it was slowly moved away from the contact point to avoid any effect on the following smoldering and transition events.
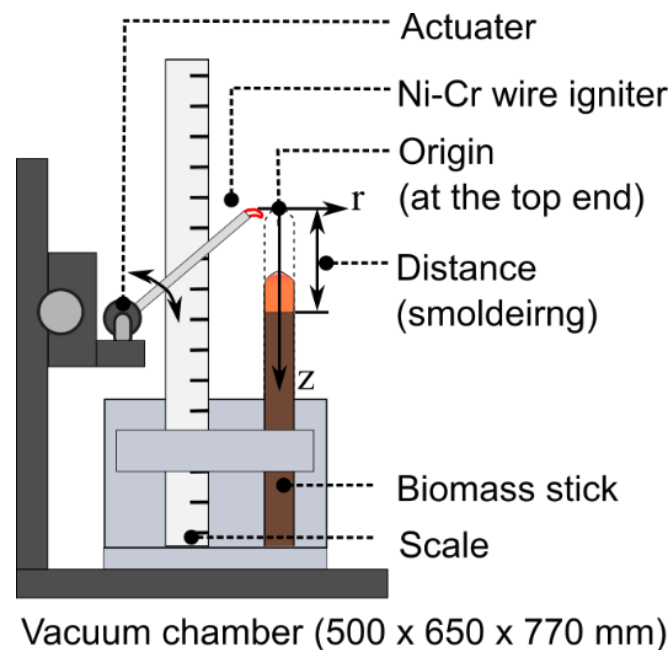
Fig. 5.1. Schematic of the experimental setup.

5.2.2.Measurement Method

The whole event was recorded by a video camera (Canon iVIS HF G10, progressive 24 fps, 1/250 seconds in integration time) through an observation window. The frames of interest were taken from the recorded data for image analysis. Using the image analysis software ImageJ Fiji [96], the positions of the propagating front, the lengths of the luminous region in smoldering, and its intensity profiles were calculated.

5.3. Experimental Results
5.3.1.Actual Images of Combustion Mode

Extracted frames of the burning biomass sticks at the represented conditions are shown in Fig. 5.2. Each image was sampled from the recorded video every second. Here, $t = 0 \, s$ is defined as the time at which the heating by the ignitor was terminated at the top of the biomass stick. The white dash lines show the surface of the circumference of the biomass sticks.

In the case of sufficient oxygen (a) $Yo = 0.82$ and $P = 100$ kPa, fast flaming at 3s is identified after the short period of the growing stage. Because the external heating was terminated before the flaming, we can say that the flaming occurred spontaneously. In this sense, even if this is a fast flaming condition, we can define it as a short-term transition. Once the flame appeared, it spread down over the surface. The propagation velocity of the flame spread was faster than the consumption velocity of the biomass stick.

Even if the oxygen was reduced at case (b), $Yo = 0.63$ and $P = 60$ kPa, the overall trend

observed is similar to case (a), although the time scale was much different. After ignition,

smoldering proceeded for 9 seconds. The intensity of the luminous regions of smoldering

seems to be identical until the transition to flaming occurs. The length of the luminous

regions was longer than that of the case (a). Small amounts of piled ash were observed

over the smoldering zone. At 9.6 seconds, the transition from smoldering to flaming was

observed, after which the flame spread moved downward. When the oxygen was reduced

further at case (c), $Yo = 0.53$ and $P = 60$ kPa, the length of the piled-up ash was around 4

mm at 43.9 s. Thus, the influence of heating to ignite the unburned region was much

smaller in the transition to flaming at 44.9 s than in the cases of (a) and (b). Smoldering

proceeded for 43.9 seconds after ignition. Ash piled up on the smoldering region because

of the longer smoldering duration. Although the lengths of the luminous regions increase

as time goes by after the ignition, it becomes nearly constant. At 44.9 seconds, the

transition from smoldering to flaming was observed and a downward flame spread is

followed. The intensities of the luminous regions of smoldering decreased as the oxygen

level reduced. The difference in intensity among the luminous regions indicated that the

oxygen levels played an important role in the reaction rate of the char oxidation because

it is a surface reaction of char and depends on the partial pressure of oxygen [98].
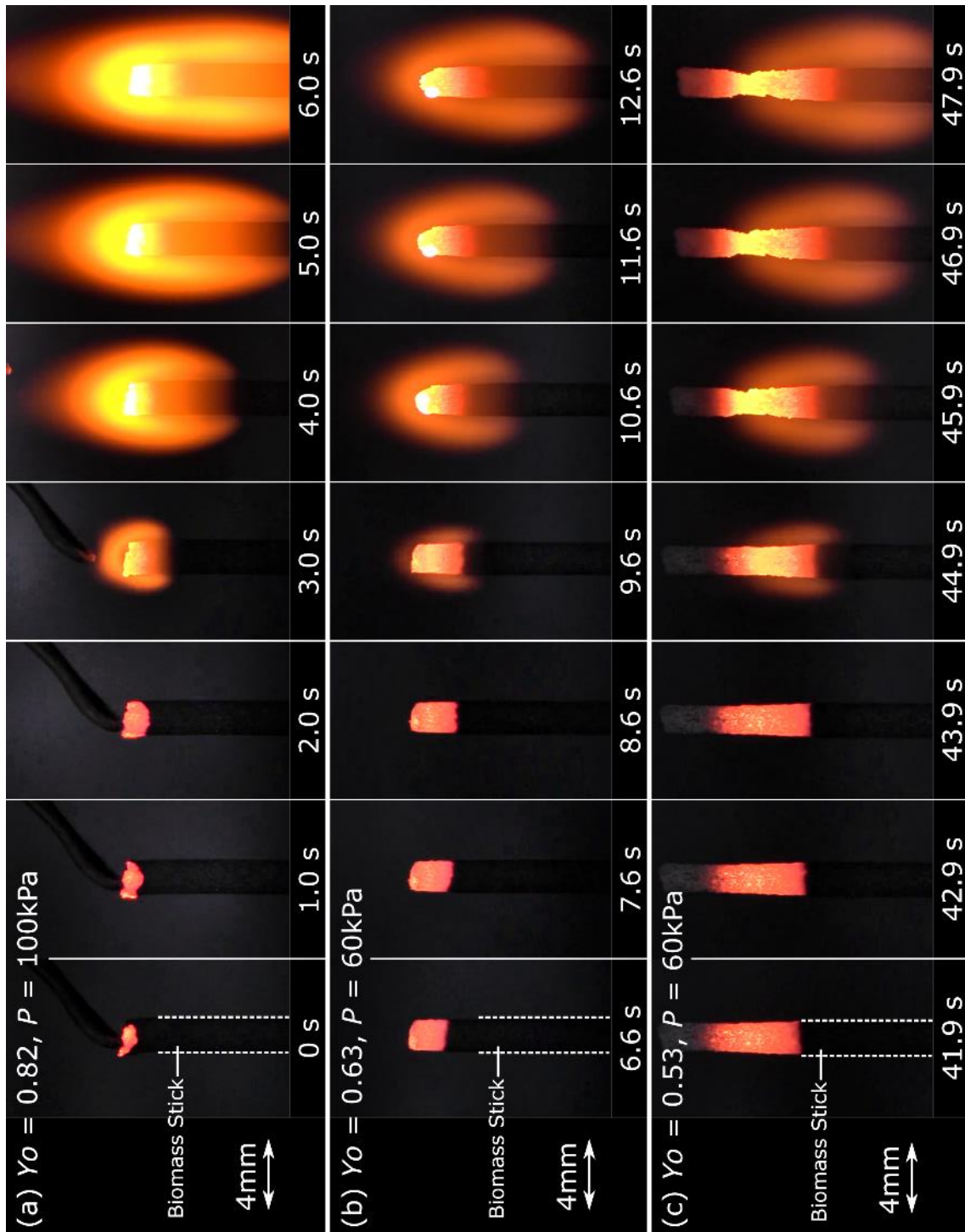
Fig. 5.2. Images frames of burning biomass sticks. (a) *Yo* = 0.82, *P* = 100 kPa. (b) *Yo* = 0.63, *P* = 60 kPa. (c) *Yo* = 0.53, *P* = 60 kPa. To improve the visibility of the images, the brightness of all images was adjusted.

5.3.2.Mapping the Transition Conditions

The smoldering behavior was classified by the environmental conditions as shown in Fig. 5.3. The horizontal axis shows the total pressure in the chamber and the vertical axis shows the oxygen levels in mass fraction. The solid triangles describe the condition in which the spontaneous transition from smoldering to flaming can be observed. The spontaneous transition to flaming describes the transition to flaming observed in steady smoldering. The open triangles describe the condition in which the transition to flaming is caused by the disappearance under the piled-up ash in the smoldering region. The solid circles show the conditions under which the smoldering can be observed entirely. The area of spontaneous transition to flaming decreases with the reduction of the pressures or oxygen levels. The dashed line shows the constant partial pressure of oxygen, $Po = 30$ kPa. The critical conditions for the spontaneous transition to flaming seem to fit the dashed line of $Po = 30$ kPa. However, the conditions under which the transition to flaming can be observed extends under lower pressures and oxygen levels, since the conditions under which the transition to flaming is caused by disappearing under the piled-up ash exists.
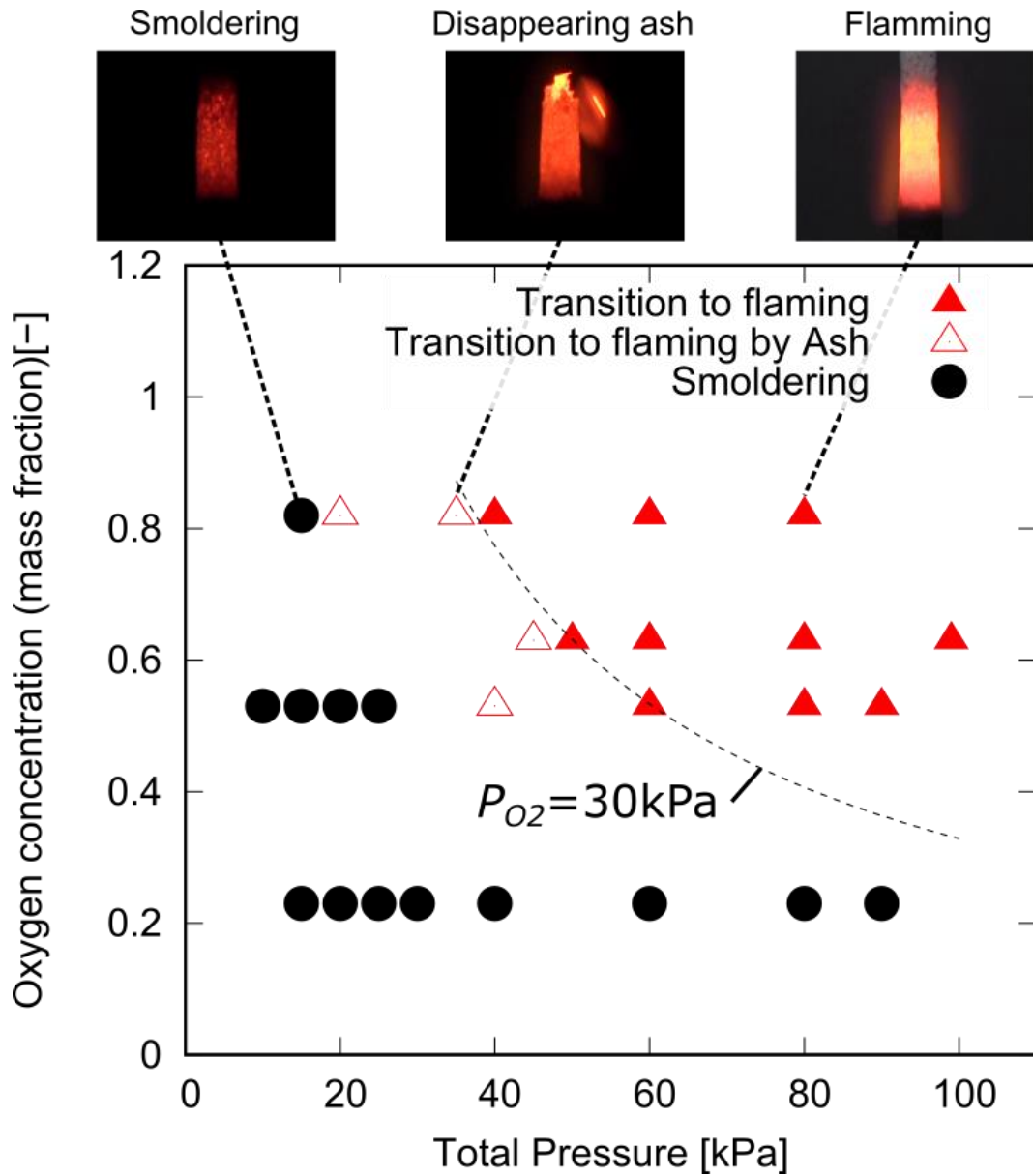
Fig. 5.3. Classification for the conditions of the smoldering and the transition to flaming. Solid triangles indicate the condition of the spontaneous transition to flaming. Open triangles indicate the condition of the transition to flaming caused by disappearing ash. Solid circles indicate the condition in which only smoldering can be observed.

5.3.3.The Length of Smoldering Region and its Change

From the image frames of the burning biomass sticks, we learned that spontaneous ignition to flaming can occur either when the length of the luminous region increases or stays as nearly constant. Figure 5.4 shows the time sequence of the lengths of the luminous region, together with the positions of the smoldering front for each condition, shown in Fig.5.4. For the case (a) $Yo = 0.82$ and $P = 100$ kPa, the lengths of the luminous region seemed constant before the flaming, as with the position of the smoldering front. After the transition at 3 seconds, the length of the luminous region gradually increased, at which time flaming was experienced. For the case (b) $Yo = 0.63$ and $P = 60$ kPa, the lengths of the luminous region increased weakly in the time before flaming as well as the position of the smoldering front. A similar trend can be seen in case (a) after flaming was experienced. For the case (c) $Yo = 0.53$ and $P = 60$ kPa, on the contrary, it was the unique behavior of the length of the luminous region, which firstly increased with the time then approached to the constant before the transition was experienced. The smoldering front continuously progressed over time, and it was clear that a firm steady state was achieved before flaming. This implies that a maximum length of the luminous region exists depending on ambient pressures and oxygen levels. The maximum length can be considered as one of the criteria for the transition to flaming because the luminous region where char oxidation is the most dominant reaction heats the ambient combustible gases.
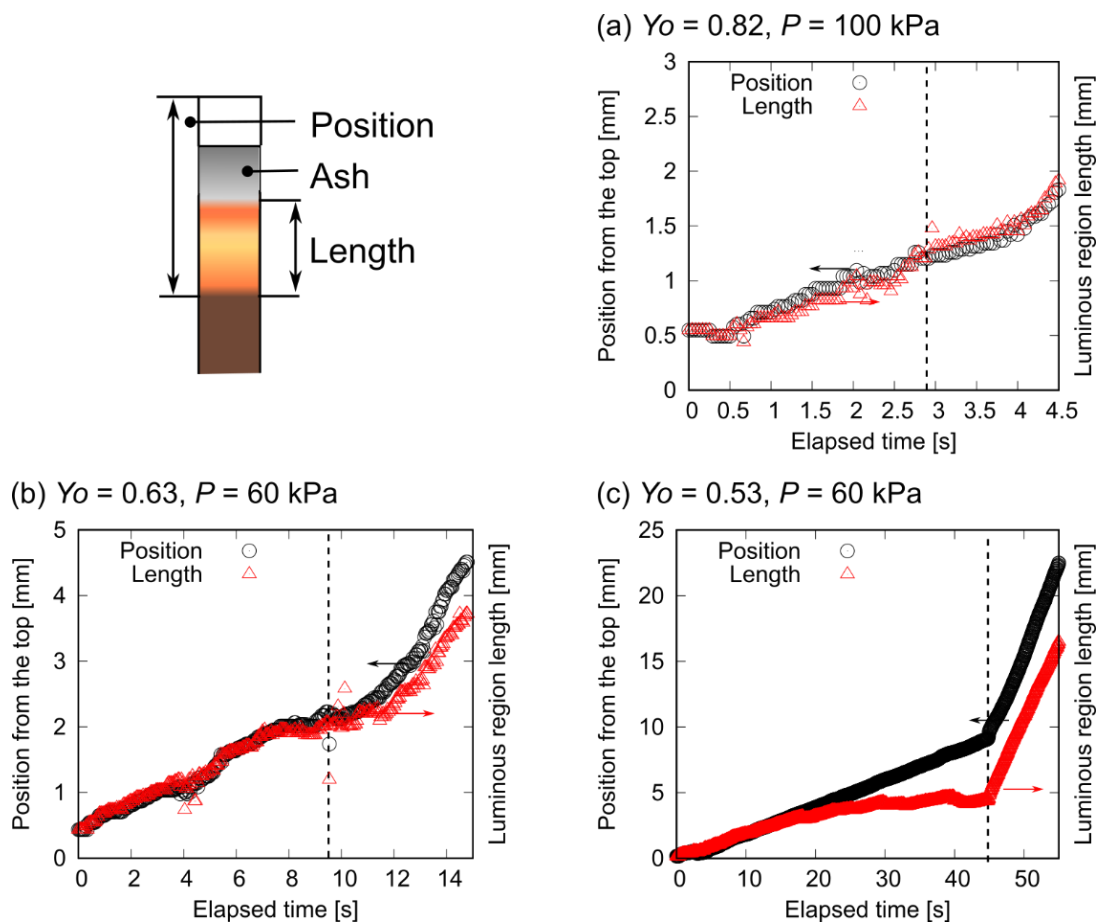
Fig. 5.4. Positions of the smoldering front from the top end of the unburnt biomass sticks and the length of the luminous region of smoldering. (a) *Yo* = 0.82, *P* = 100 kPa. (b) *Yo* = 0.63, *P* = 60 kPa. (c) *Yo* = 0.53, *P* = 60 kPa.

Figure 5.5 shows the critical lengths of the luminous region at the onset of the transition (flaming) in various environmental conditions. It is found that the lengths of the luminous region sharply increase with reducing the total pressures irrespective of the adopted oxygen levels. Interestingly, the critical lengths approach the maximum length (approximately 4 mm) for all oxygen conditions considered in this study. The presence of the maximum critical length suggests that there must be the interaction between the smoldering region and the surrounding mixtures of pyrolysis gas and ambient oxygen.
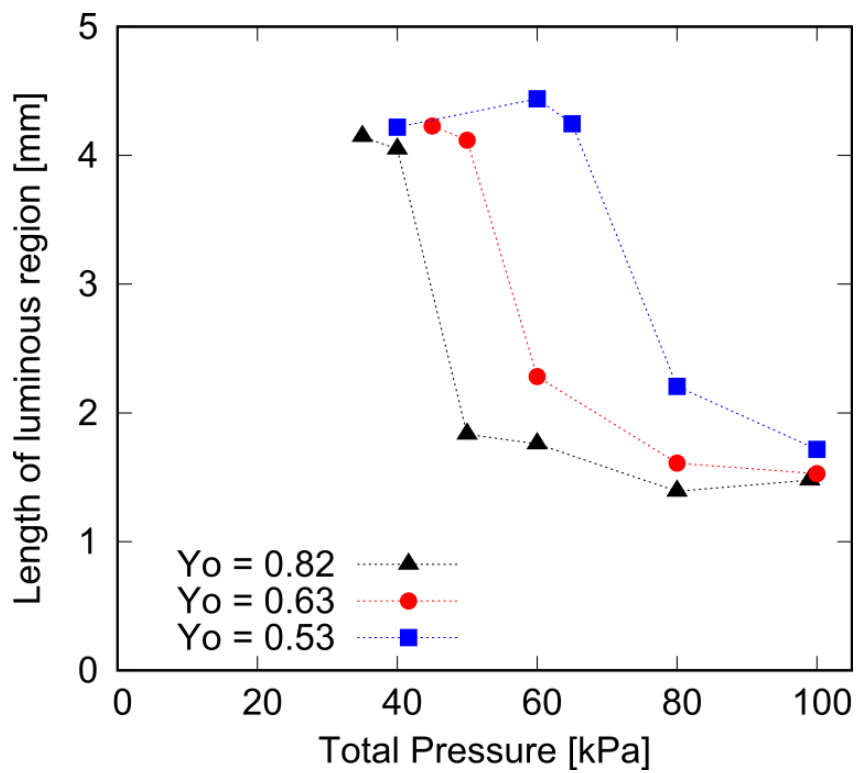
Fig. 5.5. The lengths of the luminous region on the smoldering biomass sticks against the total pressure for *Yo* = 0.82, 0.63, and 0.53.

5.4. Analysis of the Results

5.4.1. Effect of Solid-Phase Reaction on Transition to Flaming

We examine what is the trigger of transition to flaming from the relationship between the length of the luminous region on the smoldering biomass sticks and the experimental condition. Figure 5.6 shows the schematic of a smoldering sample and a simple ignition model. In smoldering combustion, the dominant heat release in the chemical reactions comes from char oxidation [98]. It is expected that the transition to flaming occurs when the heat release rate overcomes the heat losses from the char-oxidation region.
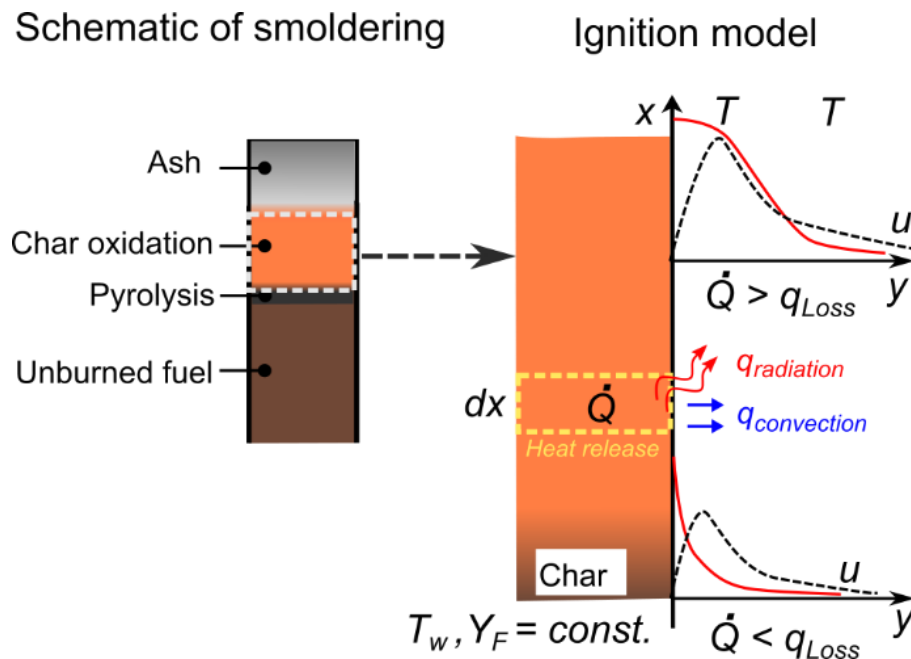
Fig. 5.6. Schematic of the char oxidation region for the transition from smoldering to flaming.

Based on the Semenov's theory of thermal ignition, an energy balance equation in the char oxidation region is developed and expressed as,

$$A(x)\{h(T_w - T_o) + \varepsilon\sigma(T_w{}^4 - T_o{}^4)\}$$
$$= V(x)\rho_s Q_s A_S (P_{o2})^n (\alpha_F)^m \exp\left(-\frac{E_s}{RT_w}\right), \tag{5.1}$$

where $A(x)$ is the surface area from the bottom of the cylinder in the ignition model to the distance x $[mm^2]$, x is the axial distance [mm] from the bottom in the ignition model, T_w is the wall temperature on the cylinder surface of the ignition model $[K]$, $V(x)$ is the volume from the bottom of the cylinder to the distance x in the ignition model $[m^3]$, ρ_s is the density of char $[kg/m^3]$, Q_s is the heating value of the char oxidation reaction [kJ/kg], A_S is the frequency factor of the char oxidation [1/s1, P_{O2} is the partial pressure of oxygen $[Pa]$, α_F is the conversion rate of char and assumed as $\alpha_F = 1.0$, E_s is the activation energy of the char oxidation [J/kg], R is the universal gas constant [J/kg $\cdot$ K], n, m are the reaction orders [-], ϵ is the emissivity of the char [-], σ is the Stefan-Boltzmann constant [W/m^2 $\cdot$ K^4], k_g is the thermal conductivity of the ambient gas $[W/m^2 \cdot K]$. The heat transfer coefficient, h $[W/m^2 \cdot K]$, along the cylinder is given as follows [104],

$$h = \frac{k}{L}\left\{\frac{4}{3}\left[\frac{(7/5)Pr}{(20 + 21Pr)}\right]^{\frac{1}{4}}(PrGr_L)^{\frac{1}{4}} + \frac{(4/35)(272 + 315Pr)}{64 + 63Pr}\frac{L}{d}\right\} \tag{5.2}$$

$$Gr_L = \frac{g\bar{\beta}(T_w - T_o)L^3}{\mu^2}\frac{P^2}{R^2 T_o{}^2} \qquad\qquad (5.3)$$

where Pr is the Prandtl number or the ratio of momentum diffusivity to thermal diffusivity, L is the characteristic length of the char oxidation region $[m]$, g is the gravity acceleration $[m/s^2]$, $\bar{\beta}$ is the volume expansion ratio $[1/K]$, and μ is the viscosity of gases $[Pa \cdot s]$.

The critical length (the axial distance) at which the heat losses in the left side of the Eq. (5.1) are equal to the heat release on the right side were calculated using the Newton-Raphson method. Fig.5.7 shows a comparison with the critical lengths of the experimental data and the predicted values. For $Yo = 0.82$, the trend of the critical lengths predicted by the simple ignition model agrees with the experimental results above 50 kPa. However, the predicted value of the critical length is quite different from the experimental one. For $Yo = 0.63$ and 0.53, similar trends are obtained. The difference between the prediction and experimental data increases with the decrease of the oxygen levels. In an environment with a higher oxygen level, the heat release rate of the char oxidation is expected to be fast. Consequently, the surface temperature can be high enough to ignite the combustible gases produced by the pyrolysis of the solid fuel. This is because the difference between the prediction and experimental data is smaller than the case of the lower oxygen level. Whereas, when the oxygen level or the total pressure is lower, the predicted lengths are

underestimated against the experimental values. The fact implies that not only the char

oxidation takes place, but also gas-phase reactions occur during the process of the

transition to flaming.
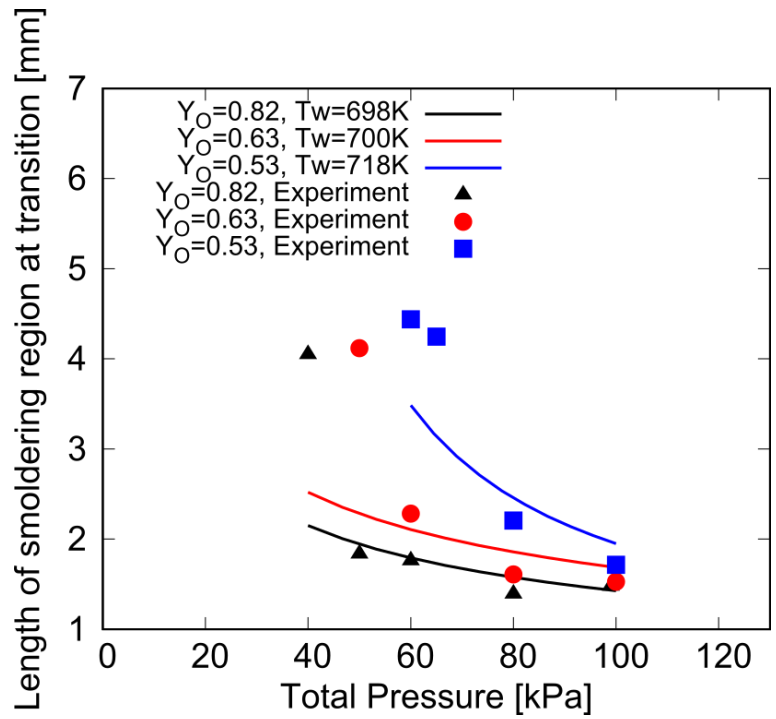
Fig. 5.7. The predicted lengths of the smoldering region at the transition against the total pressures of oxygen from the heat balance equations for $Yo = 0.53, 0.63$, and 0.82.

5.4.2. Effect of Gas-Phase Reaction on Transition to Flaming

We introduced a simple model with gas-phase reactions, referring to the approach for the Semenov model [2], to explain the relationship between the length of the smoldering region when the transition to flaming occurs and the environmental conditions. Fig. 5.8 (a) depicts a schematic diagram of the model used to examine the heat balance between the pyrolysis gases in the boundary layer and the surrounding gases. The pyrolysis gases emitted in the front of the char oxidation region then covered the surface of the char oxidation region. The ignition model for the pyrolysis gases in the boundary layer over the char oxidation region was developed as shown in Fig. 5.8 (b). Based on the Semenov model, it ignores temperature differences among pyrolysis gases in the boundary layer, while the temperature in the boundary layer was equal to the surface temperature of the char oxidation region. The heat release rate within the volume of the boundary layer was assumed to balance with the heat loss along the radial direction by natural convection at the transition to flaming. The concentrations of the pyrolysis gases were assumed not to change until the transition to flaming.

(a) Schematic of smoldering

Ash

Char oxidation — Pyrolysis gases
(CO, CH4, H2, CO2...)

Pyrolysis

Unburned fuel — Region for modeling

(b) Ignition model

δ

$\dot{Q}$ → $q_{convection}$

Heat release

Char oxidation — Boundary layer
Surface area, S
Temperature   Char   Volume, V
= const.   Temperature = const.
Reactant concentrations
= const.
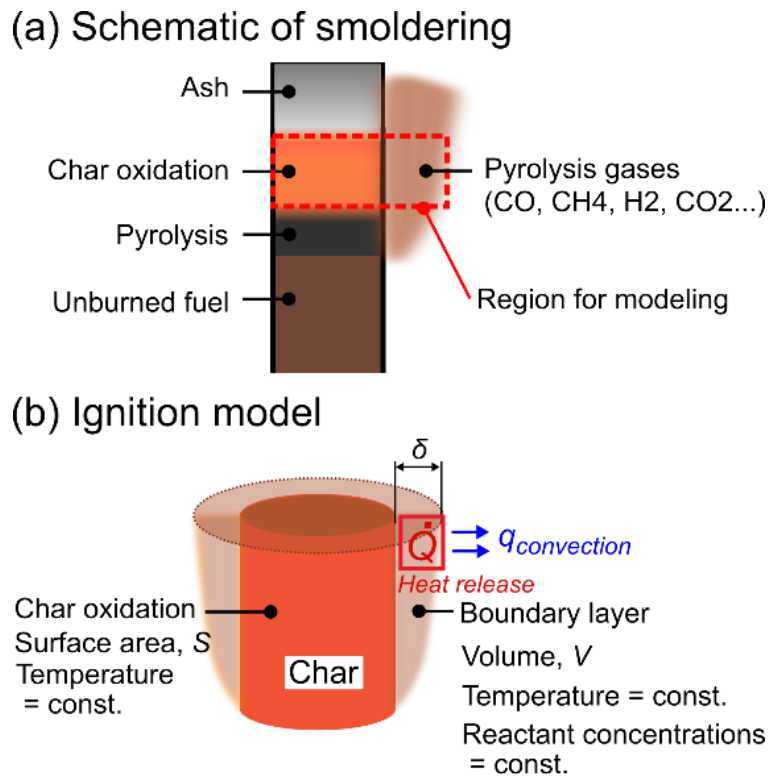
Fig. 5.8. Schematic diagram of the model showing the interaction between the smoldering region and the surrounding pyrolysis gases. (a) Description of the interaction between the smoldering region and the surrounding pyrolysis gases. (b) Ignition model of the transition to flaming.

Baker and Kilburn found that a substantial proportion of the carbon oxides and a large amount of the hydrocarbons were produced in the low-temperature region behind the char decomposition region [105]. According to the measurement for species concentration profiles over the smoldering surface done by Sato and Sega [50], carbon monoxide, methane, and hydrogen concentrations in the pyrolysis gases exist over the surface of the smoldering region, so that carbon monoxide oxidation is assumed as the dominant chemical reaction causing the spontaneous ignition due to the lower concentrations of

methane and hydrogen. The direct reaction of the carbon monoxide oxidation ($CO + O_2 \rightarrow CO_2 + O$) is a slow process because of its high activation energy. However, in the presence of hydrogen, the reaction between carbon monoxide and OH radicals ($CO + OH \rightarrow CO_2 + H$) is the dominant path for the carbon monoxide oxidation [106]. Assuming that hydrogen, oxygen, water vapor, and OH radicals are in chemical equilibrium, the reaction rate of the carbon monoxide oxidation is expressed as a function of the concentrations of oxygen, water vapor and carbon monoxide [107]. From the equilibrium formation reactions,

$$\text{H}_2 + \frac{1}{2}O_2 \overset{K_{P_{H2O}}}{\leftrightarrow} \text{H}_2\text{O} \ , \tag{5.4}$$

$$\frac{1}{2}O_2 + \frac{1}{2}\text{H}_2 \overset{K_{P_{OH}}}{\leftrightarrow} \text{OH} \ , \tag{5.5}$$

where, $K_{P_{H2O}}$ is the equilibrium constant of the reaction (5.4), and $K_{P_{OH}}$ is the equilibrium constant of the reaction (5.5). Both of the equilibrium constants are expressed as

$$K_{P_{H2O}} = \frac{P_{H2O}}{P_{H2} + (P_{O2})^{\frac{1}{2}}}, \tag{5.6}$$

$$K_{P_{OH}} = \frac{P_{OH}}{(P_{H2})^{\frac{1}{2}} + (P_{O2})^{\frac{1}{2}}}, \tag{5.7}$$

where, P_{H2O} is the partial pressure of water vapor, P_{OH} is the partial pressure of OH radical, P_{H2} is the partial pressure of hydrogen, P_{O2} is the partial pressure of oxygen. To estimate

the partial pressure of OH radical in the equilibrium state, the following equations are considered,

$$P_{H2} = \frac{P_{H2O}}{K_{P_{H2O}}(P_{O2})^{\frac{1}{2}}},$$ (5.8)

$$P_{OH} = K_{P_{OH}}(P_{H2})^{\frac{1}{2}}(P_{O2})^{\frac{1}{2}}.$$ (5.9)

Equation (5.8) is substituted into the Eq. (5.9), and then the partial pressure of OH radical in the equilibrium state can be obtained as,

$$P_{OH,eq} = \frac{K_{P_{OH}}}{\left(K_{P_{H2O}}\right)^{\frac{1}{2}}}(P_{H2O})^{\frac{1}{2}}(P_{O2})^{\frac{1}{4}}.$$ (5.10)

The reaction of CO oxidation can be expressed as,

$$-\frac{d[CO]}{dt} = k_{chem}\frac{P_{CO}}{RT}\frac{P_{OH}}{RT} = k_{chem}A_cP_{CO}(P_{H2O})^{\frac{1}{2}}(P_{O2})^{\frac{1}{4}},$$ (5.11)

where k_r is the rate constant of a chemical reaction and A_c is the pre-exponential factor. Taking into account the overall carbon monoxide consumption-rate expression Eq. (5.11), the heat balance equation between the heat release rate of the pyrolysis gases in the boundary layer and the heat loss by natural convection to the surroundings is expressed by:

$$Sh(T_w - T_o) = VQ_cW_{CO}A_cP_{CO}{}^1P_{H2O}{}^{\frac{1}{2}}P_{O2}{}^{\frac{1}{4}}\exp\left(-\frac{E}{RT_w}\right), \qquad (5.12)$$

where T_w is the temperature of the surface of the char oxidation region and in the boundary layer $[K]$, T_o is the ambient temperature of gases far from the surface $[K]$, S is the surface area of the char-oxidation region $[m^2]$, V is the volume of the pyrolysis gases in the boundary layer $[m^2]$, Q_c is the heating value of carbon monoxide oxidation [W/kg], W_{CO} is the molecular weight of carbon monoxide $[kg/mol]$, A_c is the pre-exponential factor $[mol/m^3 \cdot s]$, P_{CO}, P_{H2O}, P_{O2} are the partial pressure of carbon monoxide, water, oxygen in the pyrolysis gases respectively [kPa], E is the activation energy [kJ/mol], R is the universal gas constant $[J/mol\,K]$.

To obtain the relation between the length of the char oxidation region and the ambient pressure, the dependence of surface area S, the volume V, and the thickness of the boundary layer δ on the length L and the pressure P are can be demonstrated as

$$S = 2r_o\pi L \propto L, \qquad (5.13)$$

$$V = \pi\{(r_o + \delta)^2 - r_o{}^2\}L \sim 2\pi r_o\delta L \propto \delta L, \qquad (5.14)$$

$$\delta \propto \frac{1}{h} \propto \frac{L}{(L^3P^2)^{\frac{1}{4}}} = L^{\frac{1}{4}}P^{-\frac{1}{2}}. \qquad (5.15)$$

Dividing Eq. (5.12) by V, the both sides in Eq. (5.12) for L, and P are expressed as

$$(L.H.S) \propto \frac{S}{V}h \propto \frac{L}{\delta L}(L^3 P^2)^{\frac{1}{4}}\frac{1}{L} \propto L^{-\frac{1}{2}}P, \qquad (5.16)$$

$$(R.H.S) \propto P_{CO}{}^l P_{H2O}{}^m P_{O2}{}^n \propto P_{O2}{}^{l+m+n}, \qquad (5.17)$$

where the boundary layer thickness δ is assumed to be proportional to the reciprocal of

the heat transfer coefficient. In Eq. (5.12), P_{CO} and P_{H2O} are assumed to be proportional

to P_{O2}, because the volatile products (carbon monoxide, water vapor as a product of

hydrogen oxidation) increase with the increase of the oxygen concentration and the

smoldering temperature caused by the oxygen-rich environment [18, 19]. Eq. (5.16) and

(5.17) are rearranged, the reaction orders, and then we can obtain the following relation,

$$LP^{-2} \propto P_{O2}{}^{-3.5}. \qquad (5.18)$$

The average lengths of the smoldering region obtained from three times tests for each

condition are plotted in the $L/P^2 - P_{O2}$ planes except for the results in which the

transition to flaming is caused by disappearing under the piled-up ash in the smoldering

region (Fig. 5.9). It is found that the trend of the predicted critical lengths when the transition

to flaming occurs based on Eq. (5.18) is in good agreement with the experimental data.

Deviation might be caused by the assumption to estimate the concentration of carbon

monoxide and water vapor. However, the overall trend is well captured by the simple model.
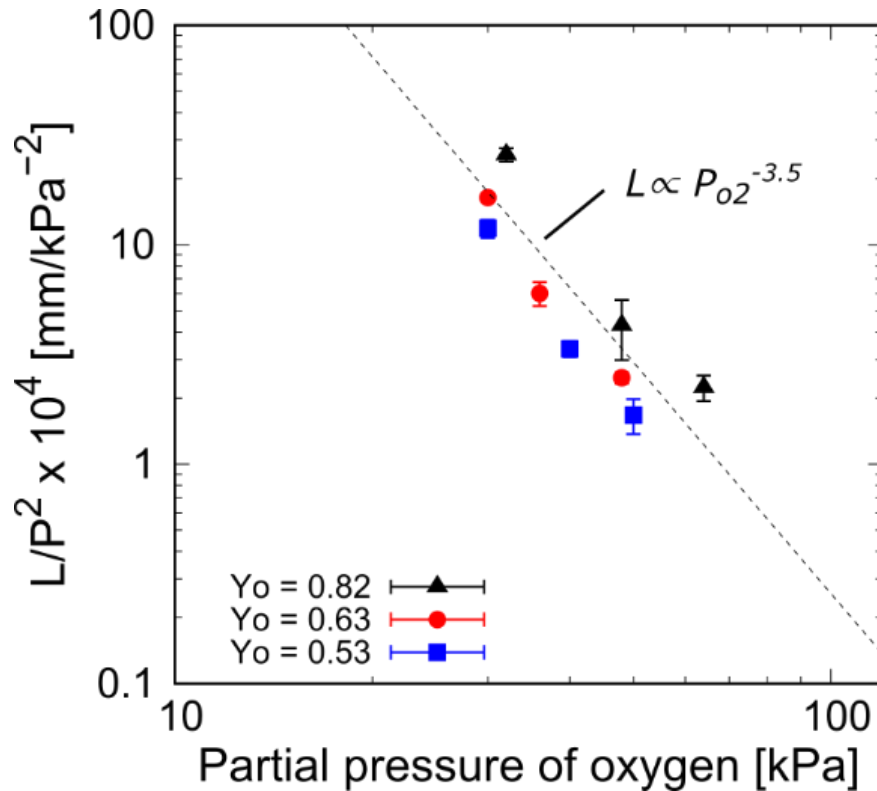
Fig. 5.9. The relationship between L/P^2 and partial pressure of oxygen.

5.5. Conclusions

The experiment of the transition from reverse smoldering to flaming in low-pressure

environments using a thin-rod biomass stick was conducted to determine the dominant

factor for the critical length of transition to flaming. Even though the reverse smoldering

was steady, the lengths of the luminous region increased over time for the cases where

the transition to flaming could be observed. The condition of the spontaneous transition

to flaming was determined by the partial pressure of oxygen. When the partial pressure of oxygen in the ambient oxidizer was lower than 30 kPa, the spontaneous transition to flaming was not observed except for the cases of disappearing under ash. To clarify the critical condition for the transition to flaming, the luminous lengths were measured by image analysis. The luminous lengths are dependent on the pressure and oxygen levels and increase with a decrease in the pressure and oxygen levels. The maximum luminous length existed through the whole conditions. To examine the relationship between the luminous lengths and the conditions of pressure and oxygen levels, simple ignition models were developed. One is based on a solid-phase reaction. The critical lengths predicted by the model show good agreement with the experimental data near the atmospheric pressure, however, the difference between the experimental data and the prediction increases with reducing the pressure. To develop a more accurate model, gas-phase reactions are taken into account. The predicted critical conditions are in good agreement with the experimental data, implying that the occurrence of the transition is mainly controlled by the heat balance between the heat release rate of the pyrolysis gases and the heat loss from the hot pyrolysis gases to the surrounding when the concentrations of pyrolysis gases are enough to ignite.

Chapter 6

6. Conclusions

6.1. Conclusions

Experimental research on transition phenomena of smoldering combustion was conducted to develop a new experimental method for examination of transition to extinction or flaming from smoldering with high reproducibility and to clarify mechanisms to cause the transition from smoldering. By varying oxygen concentrations and pressure, oxygen supply to the smoldering region can be adjusted.

Smoldering behavior in the range from the extinction limit to the transition to flaming was observed. For the transition to extinction, the range in which oxygen concentration is below 0.4 is considered as transport-controlled regime at which the limit is insensitive to the adopted oxygen concentration. Nevertheless, the limit is well-described as the nearly constant smoldering velocity, suggesting there exhibits the nearly constant temperature of the reaction region. However, it is important to notice that the limit at lower oxygen concentration (say 0.2) gives higher partial pressure of oxygen as compared to the ones at the higher oxygen concentrations (say 0,23 or 0.33). Namely, heat release is expected to be larger for the former case than the latter. Nevertheless, the temperature at the limit is constant. Considering all together, only the heat loss depending on the total pressure can be the cause to induce such a feature in the limiting condition. In this sense,

this limit can be called a "transport-controlled regime".

For the transition to flaming, when the partial pressure of oxygen in the ambient oxidizer was lower than 30 kPa, the spontaneous transition to flaming was not observed except for the cases of collapse of ash. To clarify the critical condition for the transition to flaming, the luminous lengths were measured by image analysis. The luminous lengths are dependent on the pressure and oxygen levels and increase with a decrease in the pressure and oxygen levels. The maximum luminous length existed through the whole conditions. To examine the relationship between the luminous lengths and the conditions of pressure and oxygen levels, a simple ignition model was developed. Based on the ignition theory, the relationship between the critical lengths when the transition to flaming occurs and the environmental conditions were obtained. The predicted critical conditions are in good agreement with the experimental data, implying that the occurrence of the transition is mainly controlled by the heat balance between the heat release rate of the pyrolysis gases and the heat loss from the hot pyrolysis gases to the surrounding when the concentrations of pyrolysis gases are enough to ignite.

6.2. Future Works

For feature works, the boundaries of smoldering conditions will be examined with various diameters of incense sticks and smoldering material. Summarizing the influence of various parameters such as a diameter of biomass stick, materials, pressure, and oxygen levels on transition phenomena to extinction or flaming will allow us to provide a comprehensive model to predict the transition phenomena.

References

1. Fire and Disaster Management Agency. Fire Statistics (Japanese). [Online].; 2019 [cited 2019 11 15. Available from: https://www.fdma.go.jp/pressrelease/statistics/.

2. Drysdale D. An Introduction to Fire Dynamics. 2nd ed. Chichester: John Wiley & Sons; 2011.

3. Oxford University Press. Fire.; 2019 [cited 2020 Jan. 10. Available from: https://www.lexico.com/definition/fire.

4. fire.; 2020 [cited 2020 Jan. 10. Available from: https://www.oxfordlearnersdictionaries.com/definition/english/fire_1?q=fire.

5. fire. 2020..

6. World Health Organization. Global Health Estimates 2016: Deaths by Cause, Age, Sex, by Country and by Region, 2000-2016. Geneva; 2018 [cited 2019 11 26. Available from: https://www.who.int/healthinfo/global_burden_disease/estimates/en/.

7. Zhuang J, Payyappalli VM, Behrendt A, Lukasiewicz K. Total Cost of Fire in the United States. Fire Protection Research Foundation report. Quincy, Massachusetts: National Fire Protection Association; 2017. Report No.: FPRF-2017-21.

8. Blincoe LJ, Miller TR, Zaloshnja E, Lawrence BA. The Economic and Societal Impact Of Motor Vehicle Crashes, 2010(Revised). Washington, DC: National Highway TrafficSafety Administration; 2015. Report No.: DOT HS 812 013.

9. The U.S. Fire Administration. Residential and nonresidential building fire and fire loss estimates by property use and cause (2003-2017) [Web]. Emmitsburg; 2017 [cited 2019 11 26. Available from: https://www.usfa.fema.gov/data/statistics/order_download_data.html#download.

10. Stewart & Heaton Clothing Company. What is the difference between structural and wildland fire fighting? [Online].; Stewart & Heaton Clothing Company [cited 2020 Feb. 3. Available from: http://www.shcc.com.au/FAQRetrieve.aspx?ID=41067.

11. United States Department of Agriculture. Wildfire, Wildlands, and People: Understanding and Preparing for Wildfire in the Wildland-Urban Interface. General Technical Report. Rocky Mountain Research Station; 2013. Report No.: RMRS-GTR-299.

12. Wertman SC. Death in the Line of Duty…A summary of a NIOSH fire fighter fatality investigation. [Online].; 2010 [cited 2020 Feb. 2. Available from: https://www.cdc.gov/niosh/fire/reports/face201010.html.

13. Diaz JM. Economic impacts of wildfire. SFE Fact Sheet 2012-7. 2012;: 4.

14. Page SE, Siegert F, Rieley JO, Boehm HV, Jaya A, Limin S. The amount of carbon released from peat and forest fires in Indonesia during 1997. Nature. 2002; 420: 61–65.

15. Harrison M, Page S, Limin S. The global impact of Indonesian forest fires. Biologist. 2009; 56: 156–163.

16. World Bank 2016. The cost of fire : an economic analysis of Indonesia's 2015 fire crisis. World Bank Group; 2016.

17. National Aeronautics and Space Administration (NASA). [NASA FIRMS].; 2020 [cited 2020 Jan. 10. Available from: https://firms.modaps.eosdis.nasa.gov/map/#z:2;c:-5.6,-7.9;t:adv-points;d:2019-10-26.2019-10-26;l:firms_viirs,firms_modis_a,firms_modis_t.

18. Blumenfeld J. Wildfires Can't Hide from Earth Observing Satellites. In EARTHDATA. [Online].; 2019 [cited 2020 Jan. 10. Available from: https://earthdata.nasa.gov/learn/articles/wildfires-cant-hide-from-earth-observing-satellites.

19. Scott AC. The Pre-Quaternary history of fire. Palaeogeography, Palaeoclimatology, Palaeoecology. 2000; 164(1–4): 281-329.

20. National Wildfire Coordinating Group. Guide to Wildland Fire Origin and Cause Determination. NFES 1874. ; 2016.

21. National Wildfire Coordinating Group. Wildland Fire Suppression Tactics Reference Guide. NFES 1256. ; 1996.

22. Reddington CL, Yoshioka M, Balasubramanian R, Ridley D, Toh YY, Arnold SR, et al. Contribution of vegetation and peat fires to particulate air pollution in Southeast Asia. Environmental Research Letters. 2014; 9: 12.

23. Johnston FH, Henderson SB, Chen Y, Randerson JT, Marlier M, DeFries RS, et al. Estimated Global Mortality Attributable to Smoke from Landscape Fires. Environmental Health Perspectives. 2012; 120: 695–701.

24. Simeoni A. Wildland Fires. In (eds) HMJea. SFPE Handbook of Fire Protection Engineering. New York: Springer; 2016. p. 3283-3302.

25. Lin S, Sun P, Huang X. Can peat soil support a flaming wildfire? International Journal of Wildland Fire. 2019; 28(8): 601-613.

26. World Resources Institute. CAIT Climate Data Explorer. 2017. Country Greenhouse Gas Emissions [CAIT Climate Data Explorer. 2017. Country Greenhouse Gas Emissions]. Washington, DC; 2017 [cited 2019 11 26. Available from: http://cait.wri.org.

27. van der Werf GR, Dempewolf J, Trigg SN, Randerson JT, Kasibhatla PS, Giglio L, et al. Climate regulation of fire emissions and deforestation in equatorial Asia. Proceedings of the National Academy of Sciences. 2008; 105(51): 20350-20355.

28. van der Werf GR, Randerson JT, Giglio L, Collatz GJ, Mu M, Kasibhatla PS, et al. Global fire emissions and the contribution of deforestation, savanna, forest, agricultural, and peat fires (1997–2009). Atmospheric Chemistry and Physics. 2010; 10: 11707–11735.

29. Stracher GB, Taylor TP. Coal fires burning out of control around the world. International Journal of Coal Geology. 2004; 59: 7–17.

30. Melody SM, Johnston FH. Coal mine fires and human health: What do we know? International Journal of Coal Geology. 2015; 152: 1–14.

31. Nolter MA, Vice DH. Looking back at the Centralia coal fire: a synopsis of its present status. International Journal of Coal Geology. 2004; 59: 99–106.

32. Ohlemiller TJ. Modeling of Smoldering Combustion Propagation. Progress in Energy and Combustion Science. 1985; 11(4): 277-310.

33. Rein G. Smouldering Combustion Phenomena. International Review of Chemical Engineering (IRECHE). 2009; 1(1): 1-18.

34. Yokelson RJ, Griffith DWT, Ward DE. Open-path Fourier transform infrared studies of large-scale laboratory biomass fires. Journal of Geophysical Research. 1996; 101(D15): 21067-21080.

35. Friedman R. Fire Safety in Spacecraft. Fire and Materials. 1996; 20: 235-243.

36. Quintiere JG, Birky MM, Mcdonald F, Smith GL. Analysis of Smoldering Fires in Closed Compartments and Their Hazard Due to Carbon Monoxide. NBSIR 82-2556. National Bureau of Standards; 1982.

37. Hotta H, Oka Y, Sugawa O. Interaction between Hot Layer and Updraft from a Smoldering fire Source -Part I An Experimental Approach-. Fire Science and Technology. 1987; 7(2): 17–25.

38. Nolter MA, Vice DH. Looking back at the Centralia coal fire. International Journal of Coal Geology. 2004; 59: 99–106.

39. Rein G. SFPE Handbook of Fire Protection Engineering. 5th ed. (eds.) MH, editor. New York: Springer; 2016.

40. Usup A, Hashimoto Y, Takahashi H, Hayasaka H. Combustion and thermal characteristics of peat fire in tropical peatland in Central Kalimantan, Indonesia. Tropics. 2004; 14(1): 1-19.

41. Watts AC, Kobziar LN. Smoldering Combustion in Organic Soils: Peat and Muck Fires in the Southeastern U.S. Fact Sheets and Research Summaries. Southern Fire Exchange; 2012. Report No.: 2012-9.

42. Frankenberg E, M. D, T. D. Health Consequences of Forest Fires in Indonesia. Demography. 2005; 42(1): 109–129.

43. Ahrens M. Home Fires Started by Smoking. NFPA No. USS10. Quincy: National Fire Protection Association; 2019.

44. Alarie Y, Stock MF, Matijak-Schaper M, Birky MM. Toxicity of smoke during chair smoldering tests and small scale tests using the same materials. Fundamental and Applied Toxicology. 1983; 3(6): 619-626.

45. Babrauskas V, Krasny J. Fire Behavior of Upholstered Furniture. NBS monograph 173. Gaithersburg: National Bureau of Standards; 1985.

46. Alarifi AAS, Phylaktou HN, Andrews GE. What Kills People in a Fire? Heat or Smoke? 2016 Feb. 13-14..

47. Goldstein M. Carbon Monoxide Poisoning. Journal of Emergency Nursing. 2008; 34(6): 538-542.

48. Struttmann T, Scheerer A, Prince S, Goldstein L. Unintentional carbon monoxide poisoning from an unlikely source. The Journal of the American Board of Family Practice. 1998; 11(6): 481-484.

49. Sapporo City Fire Bureau. Tobacco fire experiment, Fire Science Laboratory. [Online].; 2018 [cited 2019 11 26. Available from: https://translate.google.co.jp/translate?hl=ja&sl=auto&tl=en&u=https%3A%2F%2Fwww.city.sapporo.jp%2Fshobo%2Fshokai%2Fgakko%2Flabo%2Fmovie%2Fhaizara.html.

50. Sato K, Sega S. The Mode of Burning Zone Spread along Cylindrical Cellulosic Material. Journal of Fire Sciences. 1985; 3: 26–34.

51. Moussa NA, Toong TY, Garris CA. Mechanism of smoldering of cellulosic materials. Proceedings of the Combustion Institute. 1977; 16(1): 1447-1457.

52. Chao CYH, Wang JJ. Transition from Smoldering to Flaming Combustion of Horizontally Oriented Flexible Polyurethane Foam with Natural Convection. Combustion and Flame. 2001; 127: 2252–2264.

53. Bar-ilan A. Transition From Forward Smoldering To Flaming In Small Polyurethane Foam Samples. Fire Safety Science. ; 8: 127-138.

54. Schult DA, Matkowsky BJ, Volpert VA, Fernandez-Pello AC. Propagation and extinction of forced opposed flow smolder waves. Combustion and Flame. 1995; 101(4): 471-490.

55. Decker MA, Schult DA. Dynamics of smoulder waves near extinction. Combustion Theory and Modelling. 2004; 8: 491-512.

56. Torero JL, Fernandez-Pello AC, Kitano M. Opposed Forced Flow Smoldering of Polyurethane. Combustion Science and Technology. 1993; 91(1-3): 95-117.

57. Cohen L, Luft NW. Combustion of Dust Layers in Still Air. Fuel. 1955; 34: 154–163.

58. Palmer KN. Smouldering Combustion in Dusts and Fibrous Materials. Combustion and Flame. 1957; 1: 129–154.

59. Egerton A, Gugan K, Weinberg FJ. The Mechanism of Smouldering in Cigarettes. Combustion and Flame. 1963; 7(1): 63–78.

60. Gugan K. Natural Smoulder in Cigarettes. Combustion and Flame. 1966; 10: 161–164.

61. Salig RJ. The smoldering behavior of upholstered polyurethane cushionings and its relevance to home furnishing fires. Master thesis. Cambridge: Massachusetts Institute of Technology, Mechanical Engineering; 1982.

62. Rogers FE, Ohlemiller TJ, Kurtz A, Summerfield M. Studies of the Smoldering Combustion of Flexible Polyurethane Cushoning Materials. Journal of fire and flammability. 1978; 9: 5–13.

63. Ohlemiller TJ, Rogers FE. A Survey of Several Factors Influencing Smoldering Combustion in Flexible and Rigid Polymer Foams. Journal of fire and flammability. 1978; 9: 489–509.

64. Ohlemiller TJ, Bellan J, Rogers F. A model of smoldering combustion applied to flexible polyurethane foams. Combustion and Flame. 1979; 36: 197-215.

65. Ohlemiller TJ, Lucca DA. An experimental comparison of forward and reverse smolder propagation in permeable fuel beds. Combustion and Flame. 1983; 54(1-3): 131-147.

66. Stocker DP, Olson SL, Torero JL, Fernandez-Pello AC. Microgravity smoldering combustion on the USML-1 Space Shuttle mission. In Heat transfer in microgravity. New York: American Society of Mechanical Engineers; 1993. p. 99-110.

67. Walther DC, Fernandez-Pello AC, D.L. U. Space Shuttle Based Microgravity Smoldering Combustion Experiments. Combustion and Flame. 1999; 116: 398–414.

68. Bar-Ilan A, Rein G, Fernandez-Pello AC, Torero JL, Urban DL. Forced forward smoldering experiments in microgravity. Experimental Thermal and Fluid Science. 2004; 28(7): 743-751.

69. Bar-Ilan A, Rein G, Fernandez-Pello AC, Torero JL, Urban DL. The effect of buoyancy on opposed smoldering. Combustion Science and Technology. 2004; 176: 2027-2055.

70. Kinbara T, Endo H, Sega S. Downward propagation of smoldering combustion through solid materials. Proceedings of the Combustion Institute. 1967; 11(1): 525-531.

71. Olson SL, Miller FJ. Experimental comparison of opposed and concurrent flame spread in a forced convective microgravity environment. Proceedings of the Combustion Institute. 2009; 32(2): 2445-2452.

72. Dosanjh SS, Pagni PP, Fernandez-Pello AC. Forced cocurrent smoldering combustion. Combustion and Flame. 1987; 68(2): 131-142.

73. Fatehi M, Kaviany M. Adiabatic reverse combustion in a packed bed. Combustion and Flame. 1994; 99(1): 1-17.

74. Roy NC, Hossain A, Nakamura Y. A universal model of opposed flow combustion of solid fuel over an inert. Combustion and Flame. 2014; 161: 1645–1658.

75. Roy NC, Nakamura Y. Investigation of unsteady behaviors of forward and opposed flow. Combustion and Flame. 2016; 163: 517–531.

76. Anca-Couce A. Reaction mechanisms and multi-scale modelling of lignocellulosic. Progress in Energy and Combustion Science. 2016; 53: 41–79.

77. Vassilev SV, Baxter D, Andersen LK, Vassilevaa CG. An overview of the chemical composition of biomass. Fuel. 2010; 89(5): 913-933.

78. Rein G, Lautenberger C, Fernandez-Pello AC, Torero JL, Urban DL. Application of genetic algorithms and thermogravimetry to determine the kinetics of polyurethane foam in smoldering combustion. Combustion and Flame. 2006; 146(1-2): 95-108.

79. Kashiwagi T, Nambu H. Global kinetic constants for thermal oxidative degradation of a cellulosic paper. Combustion and Flame. 1992; 88(3-4): 345-368.

80. Huang X, Rein G. Smouldering combustion of peat in wildfires: Inverse modelling of the drying and the thermal and oxidative decomposition kinetics. Combustion and Flame. 2014; 161(6): 1633-1644.

81. Ortiz-Molina MG, Toong T, Moussa NA, Tesoro GC. Smoldering combustion of flexible polyurethane foams and its transition to flaming or extinguishment. Proceedings of the Combustion Institute. 1979; 17(1): 1191-1200.

82. Ohlemiller TJ. Forced Smolder Propagation and the Transition to Flaming in Cellulosic Insulation. Combustion and Flame. 1990; 81: 354–365.

83. Aldushin AP, Bayliss A, Matkowsky BJ. Is there a transition to flaming in reverse smolder waves? Combustion and Flame. 2009; 156: 2231–2251.

84. Nakamura Y, Aoki A. Irradiated ignition of solid materials in reduced pressure atmosphere with various oxygen concentrations – for fire safety in space habitats. Advances in Space Research. 2008; 40: 777–782.

85. Mukunda HS, Basani J, Shravan HM, Philip B. Smoldering combustion of "incense" sticks - Experiments and modeling. Combustion Science and Technology. 2007; 179: 1113–1129.

86. Plötze M, Niemz P. Porosity and pore size distribution of different wood types. European Journal of Wood and Wood Products. 2011; 69: 649–657.

87. Bird RB, Stewart WE, Lightfoot EN. Transport Phenomena, Int. student edn. 2nd ed. New York: Wiley; 2001.

88. Jaluria Y. Natural convection: Heat and mass transfer. 1st ed. Oxford: Pergamon Press; 1980.

89. Schlichting H. Boundary-Layer Theory. 7th ed. New York: McGraw-Hill, Inc.; 1987.

90. Kaviany M. Principles of Heat Tranfer in Porous Media. 2nd ed. New York: Springer; 1995.

91. Dai C, Yu C, Zhou X. Heat and Mass Transfer in Wood Composite Panels during Hot Pressing. Part II. Modeling Void Formation and Mat Permeability. Wood and Fiber Science. 2005; 37: 242–257.

92. Goitsuka S, Nakamura Y, Matsuoka T. Scale Modeling on Smoldering of Thin Rod Combustibles. 8th International Symposium on Advanced Science and Technology in Experimental Mechanics (8th ISEM). 2013 November 3-6;: 104.

93. Skelland AHP. Diffusional Mass Transfer. Reprint ed.: John Wiley & Sons, Inc.; 1985.

94. He W, Lv W, Dickerson J. Gas Transport in Solid Oxide Fuel Cells. In: Gas Diffusion Mechanisms and Models. 1st ed. Cham, Heidelberg, New York, Dordrecht, London: Springer; 2014.

95. Pisani L. Simple Expression for the Tortuosity of Porous Media. Transport in Porous Media. 2011; 88(2): 193–203.

96. Schindelin J, Argenda-Carreras I, Frise E, Kaynig V, Longair M, Pietzsch T, et al. Fiji: an open-source platform for biological-image analysis. Nature methods. 2012; 9(7): 676-682.

97. Hurt RH, Calo JM. Semi-Global Intrinsic Kinetics for Char Combustion Modeling. Combustion and Flame. 2001; 125: 1138–1149.

98. Anca-Couce A, Zobel N, Berger A, Behrendt F. Smouldering of pine wood: Kinetics and reaction heats. Combustion and Flame. 2012; 159(4): 1708-1719.

99. JanseHarald AMC, de Jonge HG, Prins W, van Swaaij WPM. Combustion Kinetics of Char Obtained by Flash Pyrolysis of Pine Wood. Industrial & Engineering Chemistry Research. 1998; 37: 3909-3918.

100. Kaviany M, Singh BP. Radiative Heat Transfer in Porous Media. Advances in Heat Transfer. 1993; 23: 133-186.

101. Ragland KW, Aerts DJ, Baker AJ. Properties of wood for combustion analysis. Bioresource Technology. 1991; 37(2): 161-168.

102. Rohsenow WM, Hartnett JP, Cho YI. Handbook of Heat Transfer. 3rd ed. New York: McGraw-Hill Education; 1998.

103. Hadden RM, Rein G, Belcher CM. Study of the competing chemical reactions in the initiation and spread of smouldering combustion in peat. Proceedings of the Combustion Institute. 2013; 34: 2547–2553.

104. Burmeister LC. Convective Heat Transfer. 2nd ed. New York: John Wiley & Sons, Inc.; 1993.

105. Baker RR, Kilburn KD. The Distribution of Gases within the Combustion Coal of a Cigarette. Beiträge zur Tabakforschung. 1973; 7: 79–87.

106. Law CK. Combustion Physics. 1st ed. New York: Cambridge University Press; 2006.

107. Dryer FL, Glassman I. High-temperature oxidation of CO and CH4. Symposium (International) on Combustion. 1973; 14(1): 987-1003.

108. S.M. Melody FHJ. Coal mine fires and human health: What do we know? International Journal of Coal Geology. 2015; 152: 1–14.

109. Boetcher SKS. Natural Convection Heat Transfer From Horizontal Cylinders. In Boetcher SKS. Natural Convection from Circular Cylinders. Cham: SpringerBriefs in Applied Sciences and Technology. Springer; 2014. p. 3-22.

110. Bird RB, Stewart WE, Lightfoot EN. Transport Phenomena, Int. student edn. 2nd ed. New York: Wiley; 2001.

111. Beal FC, Eickner HW. Thermal degradation of wood components: a review of the literature. 1st ed. Madison: U.S. Forest Products Laboratory ; 1970.

112. Hu Y, Fernandez-Anez N, Smith TEL, Rein G. Review of emissions from smouldering peat fires and their contribution to regional haze episodes. International Journal of Wildland Fire. 2018; 27: 293-312.

113. Wichman IS. Theory of opposed-flow flame spread. Progress in Energy and Combustion Science. 1992; 18: 553–593.

Appendices

A) Element Analysis and Thermogravimetric Analysis

A.1 Element analysis

The main chemical composition and high heating value of the incense stick are shown in

Table A.1.

Table A.1 The main chemical composition of the incense stick

Element	Unit	Value
C	$mass$ %	49.2
H	$mass$ %	4.0
N	$mass$ %	0.4
O	$mass$ %	26.2
HHV	MJ/kg	17.4

A.2 Thermogravimetric analysis

Mass loss data from the thermogravimetric analysis can be recalculated into conversion,

α [-]. The conversion represents the actual amount of the testing sample. The expression

of conversion is defined as:

$$\alpha = \frac{m_0 - m}{m_0 - m_\infty} \qquad (A.1)$$

Where m_0 is the initial mass of fuel sample $[\mu g]$, m is the actual mass of fuel sample $[\mu g]$,

and m_∞ is the residual mass after testing. The rate of conversion is expressed as a function of temperature and conversion:

$$\frac{d\alpha}{dt} = f(T, \alpha) \qquad\qquad \text{(A.2)}$$

The changes of conversion of the incense stick in the pure-nitrogen atmosphere are shown Fig. A.1. The tests are repeated two times. Whereas, Fig.A.2 shows the changes of conversion of the incense stick in the air.
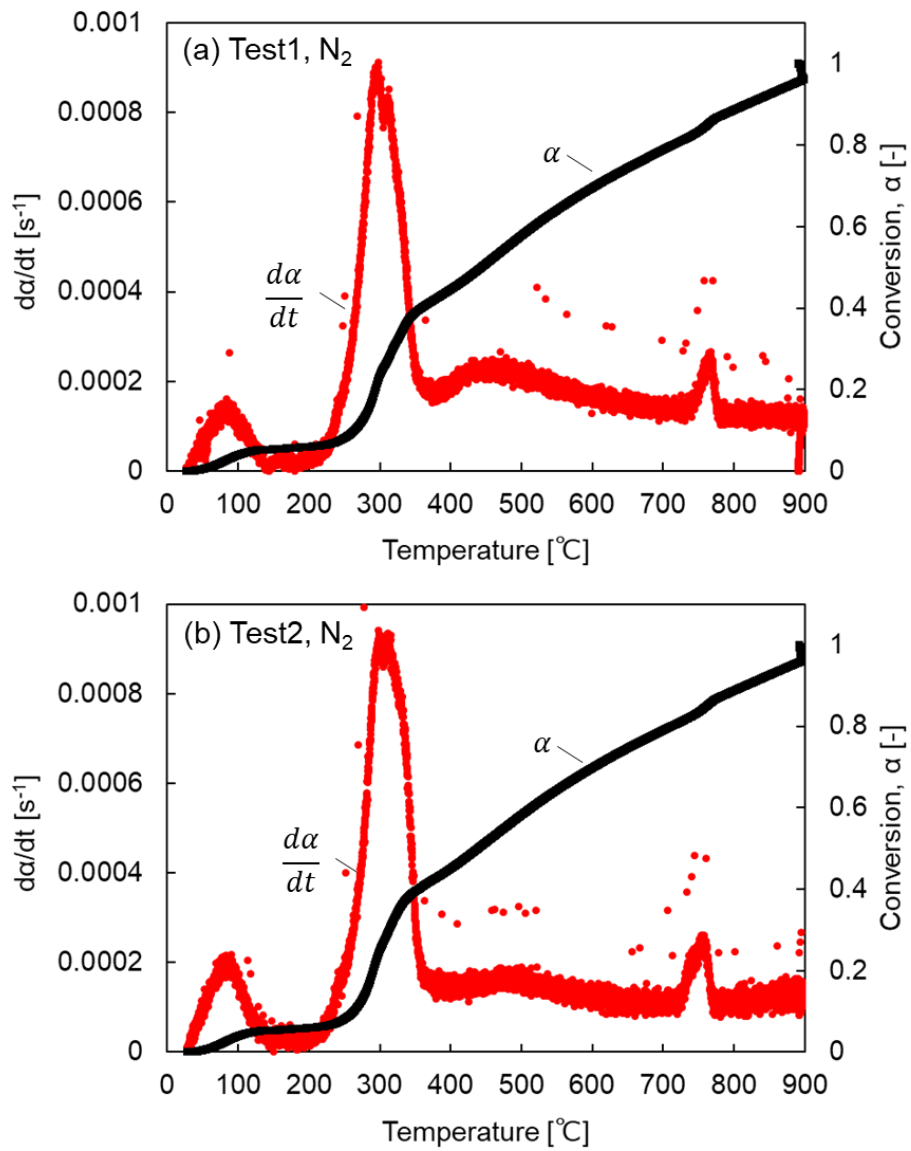
Fig. A.1. The conversion and the conversion rate of the incense stick in pure-nitrogen atmosphere. The heating rate is 10 K/min.
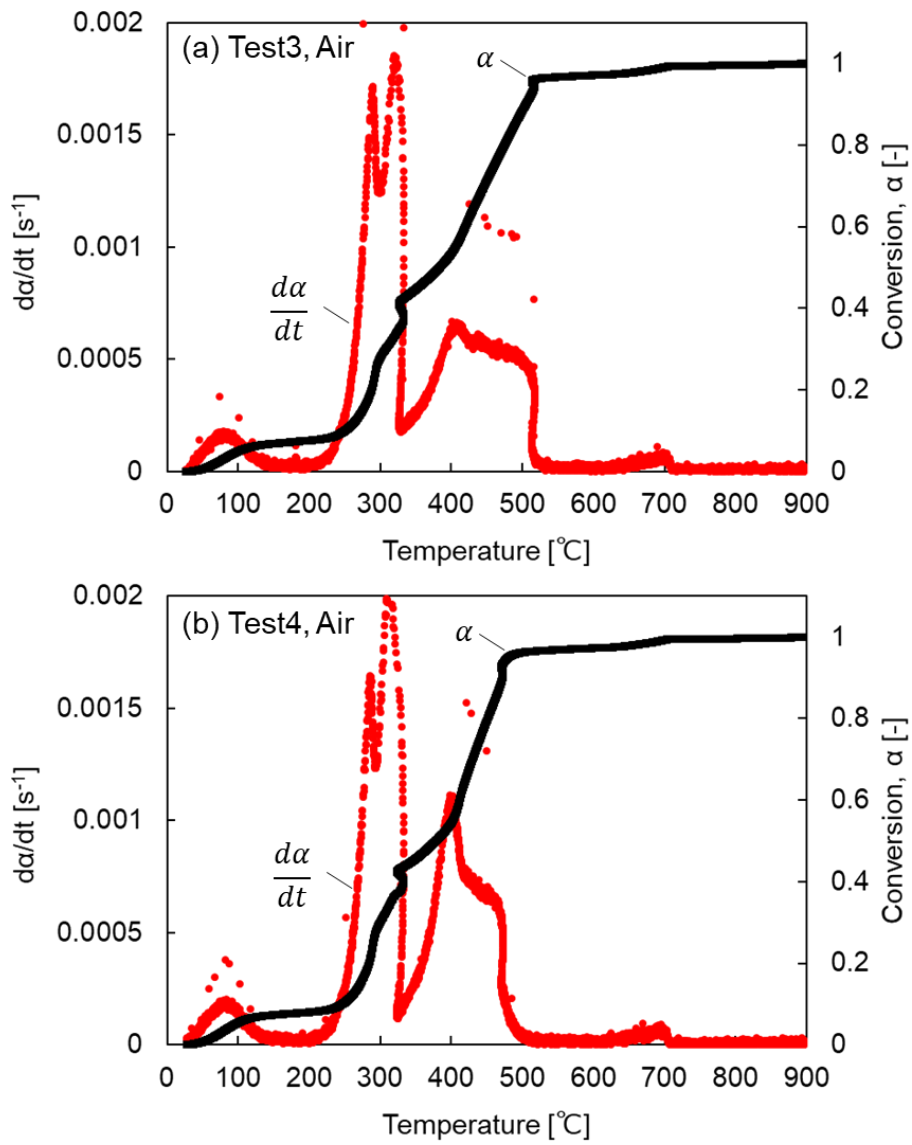
Fig. A.2. The conversion and the conversion rate of the incense stick in the air. The heating rate is 10 K/min.

B) Instruction How to Make a Thermocouple

This Appendix C explains how to make a thermocouple. The next page starts the instruction manual for the methods to make thermocouples.

HOW TO MAKE TEHRMOCOUPLES

Kazunari Hamaue, Takuya Yamazaki

Last modified：March/5/2020

B.1 About Thermocouples

What is a thermocouple?

A thermocouple is a measurement instrument for measuring temperature directly. The instrument consists of two dissimilar electrical conductors. A thermocouple produces electromotive force at its junction in high temperature. Then temperature is inferred from the voltage level. The following list shows advantages in contrast with mercury thermometers or thermistors.

- Quickly respond.

- Enable to measure temperature with wide range -200℃~+1700℃.

- Enable to measure temperature at specific point.

- Easily handle data of measured temperature because output is voltage signal.

- Available in in low cost.

Principle of a thermocouple

Electromotivative force is generated in the circuit which consists of two dissimilar materials with jointed each end when the joints have different temperature (Fig.B1). This phenomenon is called "Seebeck effect" after Thomas J. Seebeck, a German physicist and discovered that in 1821. The electromotive force is called Thermoelectromotive force. The generated voltage and its polarity depend on the only the temperature difference between two joints of the circuit.

Measuring temperature by a thermocouple is based on the *Seebeck effect*. The configuration for measuring temperature is shown in Fig.B2. Thermoelectromotive force is generated when the sensing junction in the thermocouple is in the temperature,

T_1. In the connected points of the measurement device, the temperature is defined as the reference temperature, T_{ref}. The generated voltage is a function of the temperature difference. We can convert the generated voltage to the temperature at the sensing junction using the relationship between the generated voltage and the temperature difference.
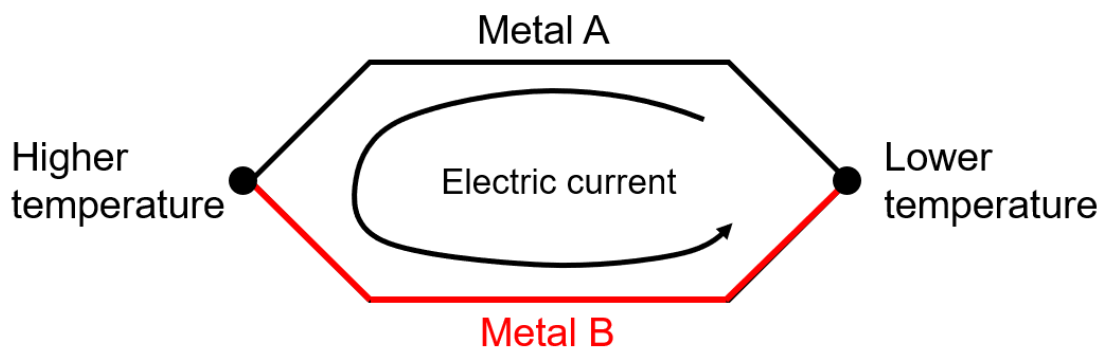
Fig.B1 Seebeck effect [C1].
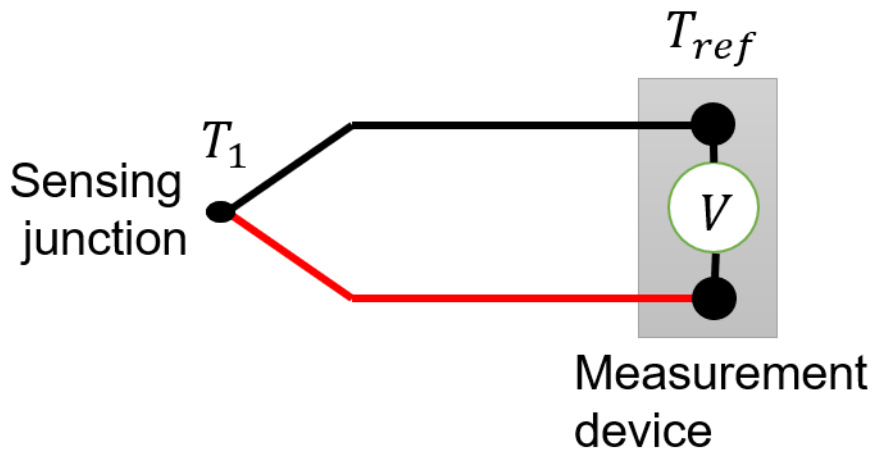
Fig.B2 Configuration for using a thermocouple [B1].

Three laws for thermocouples

There are three essential laws for using a thermocouple correctly. [B2, B3, B7]

Low of homogenous materials

The circuit is shown in Fig.B3(a) which consists of a homogeneous wire, physically and chemically the same throughout. In this circuit Thermoelectromotive force does not occur when each joint has different temperature. The sum of thermoelectromotive force in this circuit, E [V], can be written as

$$E = E_{AA}(T_1) + E_{AA}(T_2) + E_{AA}(T_3) = 0,$$

where $E_{AA}(T_1)$ [V] is electromotive force at the joint with the temperature T_1, $E_{AA}(T_2)$ [V] is electromotive force at the joint with the temperature T_2 and $E_{AA}(T_3)$ [V] is electromotive force at the joint with the temperature T_3. The other circuit which consists of two dissimilar materials as a thermocouple is shown in Fig.B3 (b). When four joints exist and each joint has different temperature, the sum of thermoelectromotive force in this circuit, E [V], can be written as

$$E = E_{AB}(T_1) + E_{BA}(T_2) + E_{AA}(T_3) + E_{AA}(T_4) = E_{AB}(T_1) + E_{BA}(T_2),$$

where $E_{AB}(T_1)$ [V] is electromotive force (from wire A to wire B) at the joint with the temperature T_1, $E_{BA}(T_2)$ [V] is electromotive force (from wire B to wire A) at the joint with the temperature T_2, $E_{AA}(T_3)$ [V] is electromotive force at the joint with the temperature T_3, and $E_{BB}(T_4)$ [V] is electromotive force at the joint with temperature

T_4. Namely, thermoelectromotive force occurs at joint between A wire and B wire or B wire and A wire because of the temperature difference, while thermoelectromotive force does not occur at joints with the temperature T_3 or T_4 because of homogeneous material.

(a) Single material   (b) Different materials

A, B : Wire materials
T_i : Temperature at node i
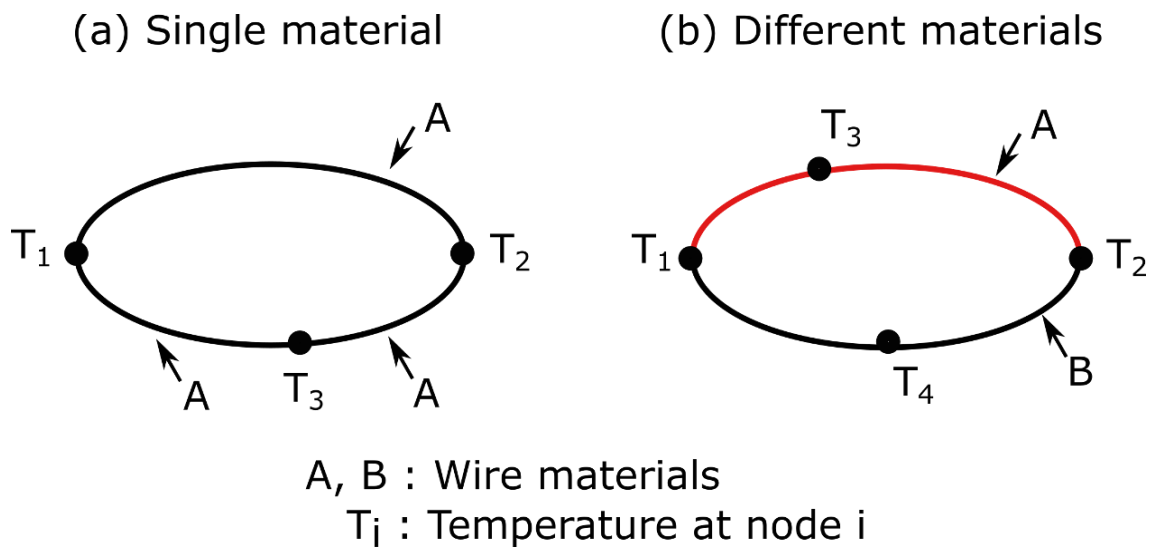
Fig.B3 Schematic diagram for law of homogeneous circuits.

Low of intermediate

In Fig.B4, the circuit consists of two materials for a thermocouple and the other material (called intermediate material). In case of Fig.B4 (a), no thermoelectromotive force is occurred at the joints connected with intermediate material when the temperatures at these joints are the same. The sum of thermoelectromotive force in this circuit, E [V], can be written as

$$E = E_{AB}(T_1) + E_{BA}(T_2) + \{E_{CA}(T_3) + E_{AC}(T_3) + E_{BC}(T_3) + E_{CB}(T_3)\}$$
$$= E_{AB}(T_1) + E_{BA}(T_2)$$

$$E_{CA}(T_3) + E_{AC}(T_3) + E_{BC}(T_3) + E_{CB}(T_3)$$
$$= E_{CA}(T_3) - E_{CA}(T_3) + E_{BC}(T_3) - E_{BC}(T_3) = 0,$$

where $E_{AB}(T_1)$ [V] is electromotive force at the joint with the temperature T_1, $E_{BA}(T_2)$ [V] is electromotive force at the joint with the temperature T_2, $E_{CA}(T_3)$ [V] is electromotive force at Node1 with temperature T_3, $E_{AC}(T_3)$ [V] is electromotive force at Node2 with the temperature T_3, $E_{BC}(T_3)$ [V] is electromotive force at Node3 with the temperature T_3 and $E_{CB}(T_3)$ [V] is electromotive force at Node4 with the temperature T_3. For the other case, Fig.C4 (b) shows that thermoelectromotive force is occurred at joints connected with intermediate material when these joints have different temperature. The sum of thermoelectromotive force in this circuit, E [V], can be written as

$$E = E_{AB}(T_1) + E_{BA}(T_2) + E_{CA}(T_3) + E_{AC}(T_4) + E_{BC}(T_3) + E_{CB}(T_4),$$

where $E_{CA}(T_3)$ [V] is electromotive force at Node1 with the temperature T_3, $E_{AC}(T_4)$ [V] is electromotive force at Node2 with the temperature T_4, $E_{BC}(T_3)$ [V] is electromotive force at Node3 with the temperature T_3 and $E_{CB}(T_4)$ [V] is electromotive force at Node4 with the temperature T_4.

(a) Same temperature
between ends of C wire

(b) Different temperature
between ends of C wire

A, B, C : Wire materials
T_i : Temperature at node i
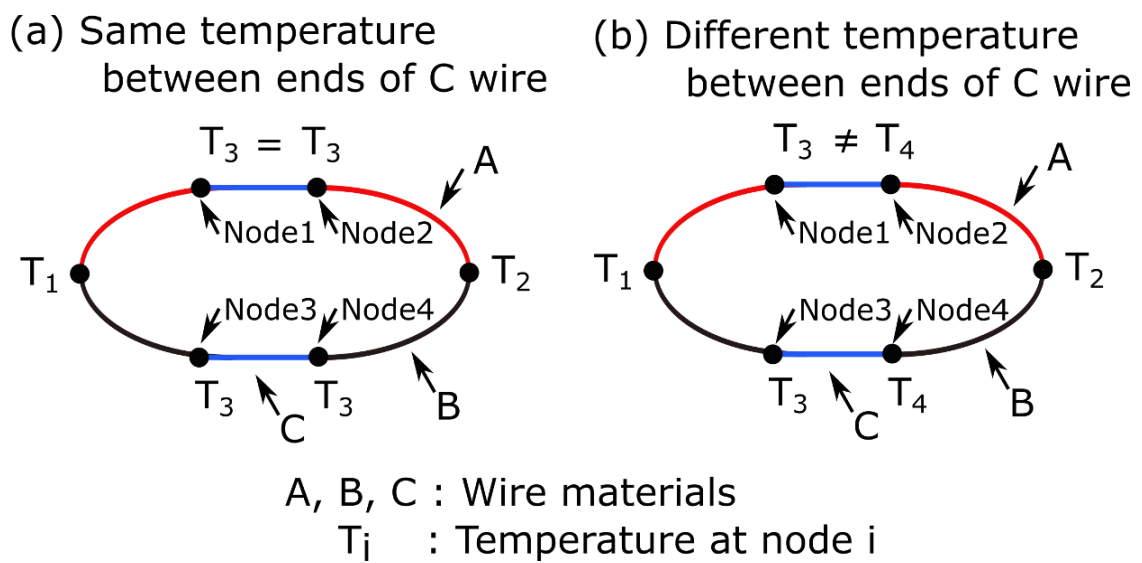
Fig.B4 Schematic diagram for law of intermediate metals.

The circuit is shown in Fig.B5 in which ends of thermocouple wire are connected with the other material. The material C can be considered as circuits of a measurement device or a filter circuit. When these joints have same temperature no thermoelectromotive force occurs at the joints connected with material C based on the law of intermediate materials. It seems that other circuits (for example, inside circuit of data logger) does not influence on electromotive force of a thermocouple.
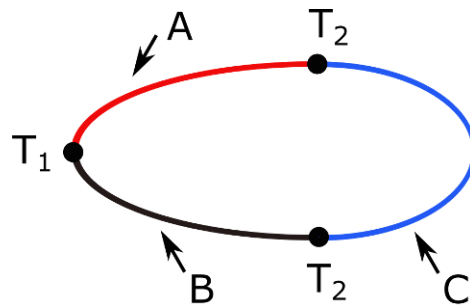
A, B, C : Wire materials
T_i : Temperature at node i

Fig.B5 Influence of electrical circuit on electromotive force.

Law of successive or intermediate temperatures

Three circuits including a thermocouple are shown in Fig.B6. Each joint in a thermocouple has different temperature. On the assumption that $T_1 > T_2 > T_3$, sum of thermoelectromotive forces in the circuit X and the circuit Y equals to that in the circuit Z. Electromotive force in each circuit can be written as

$$E_X = E_{AB}(T_1) + E_{BA}(T_2)$$

$$E_Y = E_{AB}(T_2) + E_{BA}(T_3) = -E_{BA}(T_2) + E_{BA}(T_3)$$

$$E_Z = E_{AB}(T_1) + E_{BA}(T_3) = E_X + E_Y.$$
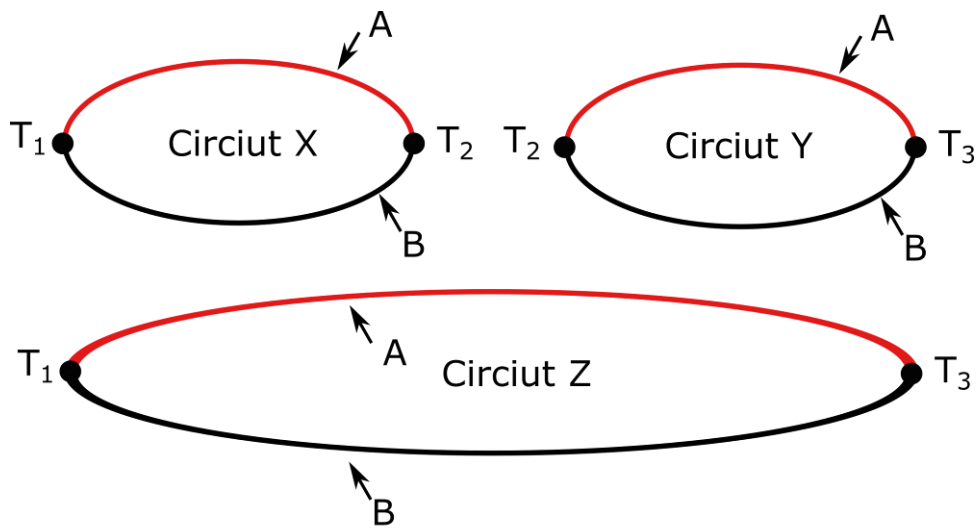
A, B : Wire materials
T_i : Temperature at node i

Fig.B6 Schematic diagram for law of intermediate temperatures.

B.2 How to Select Type of a Thermocouple
Selection for a range of temperature or reliability

There are eight types of thermocouples in some industrial standard. User must select

suitable type of a thermocouple. The list of types and characteristics of thermocouples

is shown in Table B1.

Table B1 Types and characteristics of thermocouple [B4, B8, B9]

Type	Material (positive terminal)	Material (negative terminal)	Temperature range [°C] ([°F])	Note
K	Chromel (90% Ni, 10% Cr)	Alumel (95% Ni, 2% Mn, 2% Al)	-270 – 1260 (-454 – 2300)	Inexpensive, accurate, reliable and a wide temp. range
J	Iron (100% Fe)	Constantan (55% Cu, 45% Ni)	-210 – 760 (-346 – 1400)	Equivalent to the K type in terms of expense and reliability, shorter lifespan at high temp.
T	Copper (100% Cu)	Constantan (55% Cu, 45% Ni)	-270 – 370 (-454 – 700)	Very stable, used in extremely low temp.
E	Chromel (90% Ni, 10% Cr)	Constantan (55% Cu, 45% Ni)	-270 – 870 (-454 – 1600)	Stronger signal and higher accuracy than K type
N	Nicrosil (84.6% Ni, 14.2% Cr, 1.4 % Si)	Nisil (95.5% Ni, 4.4% Si, 1% Mg)	-270 – 1260 (-454 – 2300)	Same accuracy and temp. limit as the K type, slightly more expensive
S	Platinum 10% Rhodium	Pure Platinum	-50 – 1480 (-58 – 2700)	Used in very high temp. applications
R	Platinum 13% Rhodium	Pure Platinum	-50 – 1480 (-58 – 2700)	Used in very high temp. applications
B	Platinum 30% Rhodium	Platinum 6% Rhodium	0 – 1700 (32 – 3100)	Used in extremely high temp. applications, high accuracy and stable at very high temp.

Selection for durability or responsivity

Exposed junction can be used when temperature is measured by a thermocouple. In this manual, exposed-junction type in thermocouples is of interest to make one. On the other hand, many manufacture thermocouple probes are type of undergrounded thermocouples, reinforced by the sheath made of metal. Characteristics for both type of thermocouples are shown in Table B2.

Table B2 Characteristics of thermocouple with or without sheath [9]

Type	Characteristics
Exposed Thermocouple	Quick response time
	Easy to make and to repair one
Undergrounded Thermocouple	Good durability, high flexural strength, shock resistant
	Good resistance to corrosion and pressure

Extension wire
What is extension wire?

It is used to extend from the thermocouple probe to the data logger or other circuit. The material of extension wire is more inexpensive than the thermocouple grade wire. That why extension grade wire is used to save cost due to the length requirements. It is noted that extension grade wire does not play as critical a role when it experiences temperature extremes and temperature cycling.

Selection for extension wires

Selection for extension wires depend on which type of thermocouple is used. Table B3 shows color code and material of extension wires.

Table B3 Color code and material of extension wires [B9]

ANSI/ASTM	Symbol Single	Generic Names	Color Coding		Magnetic Yes/No	Environment (Bare Wire)
			Individual Conductor	Overall Jacket Extension Grade Wire		
T	TP / TN	Copper / Constantan, Nominal Composition: 55% Cu, 45% Ni	●Blue ●Red	●Blue	X X	Mild Oxidizing, Reducing. Vacuum or Inert. Good where moisture is present.
J	JP / JN	Iron / Constantan, Nominal Composition: 55% Cu, 45% Ni	○White ●Red	●Black	X X	Reducing Vacuum, Inert. Limited use in oxidizing at High Temperatures. Not recommended for low temps.
E	EP / EN	Chromel®, Nominal Composition: 90% Ni, 10% Cr / Constantan, Nominal Composition: 55% Cu, 45% Ni	●Purple ●Red	●Purple	X X	Oxidizing or Inert. Limited use in Vacuum or Reducing.
K	KP / KN	Chromel, Nominal Composition: 90% Ni, 10% Cr / Alumel®, Nominal Composition: 95% Ni, 2% Mn, 2% Al	●Yellow ●Red	●Yellow	X X	Clean Oxidizing and Inert. Limited use in Vacuum or Reducing
N	NP / NN	Nicrosil®, Nominal Compositions: 84.6% Ni, 14.2% Cr, 1.4% Si / Nisil®, Nominal Composition: 95.5% Ni, 4.4% Si, 1% Mg	●Orange ●Red	●Orange	X X	Clean Oxidizing and Inert. Limited use in Vacuum or Reducing
S	SP / SN	Platinum 10% Rhodium / Pure Platinum	●Black ●Red	●Green	X X	Oxidizing or Inert Atmospheres. Do not insert in metal tubes. Beware of contamination.
R	RP / RN	Platinum 13% Rhodium / Pure Platinum	●Black ●Red	●Green	X X	Oxidizing or Inert Atmospheres. Do not insert in metal tubes. Beware of contamination.
B	BP / BN	Platinum 30% Rhodium / Platinum 6% Rhodium	●Gray ●Red	●Gray	X X	Oxidizing or Inert Atmospheres. Do not insert in metal tubes. Beware of contamination.

THERMOCOUPLE CHARACTERISTICS TABLE

Note of using extension wire

When an extension grade wire is used to extend from the thermocouple probe to the measurement device or the other circuit, joints of the extension wire must be far away from the high temperature object. If extension wire experiences high temperature (over 100 °C), an unexpectable thermoelectromotive force occurs in the extension wires. In that case, accurate temperature at the sensing junction will be no longer measured due to the unexpected thermoelectromotive force.
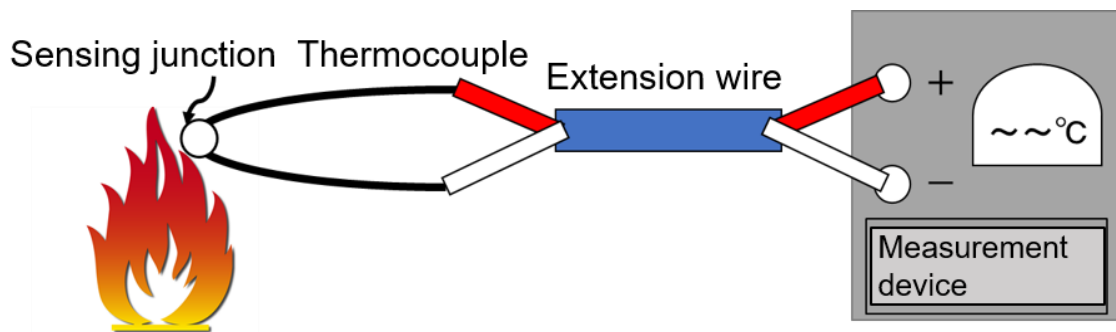
Fig. B7 Suitable use for extension wires.

B3 How to Make Thermocouples

In this manual, there are two ways to make a thermocouple; one is "welding with a micro burner" and another is "welding with electronic spark". Former is for thermocouple wire more than 50 μm and latter is for one less than 50 μm.

Welding with a micro burner
Preparing a micro burner

In this manual the burner, O2 Torch OT-3000 manufactured by Shinfuji Burner co., is used (Fig.B8). The flame of the torch is premixed flame with LPG gas as fuel and Oxygen gas as oxidizer.

Fig.B8 O2 Torch OT-3000 [B5].

Preparation for the burner

1. Confirm whether valves of fuel and oxidizer close.

    It is noted that an explosion may occur resulting from mixing a gas in the air when

    a user ignites.
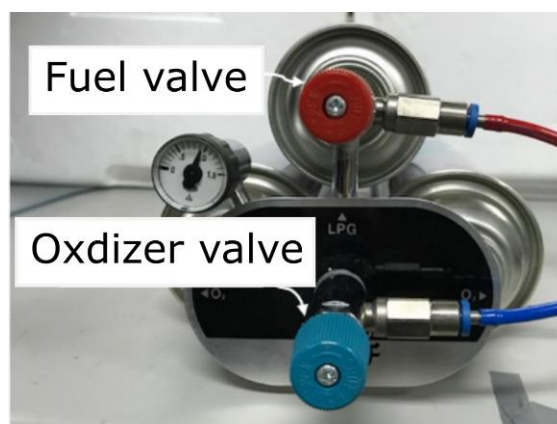
2. Put the supporter on a flat desk and then set the burner on the supporter.

    Confirm whether the burner is set the supporter surely due to avoid fire incidents

    or getting burned. It is noted that gas tubes are set far away from the outlet of burner.
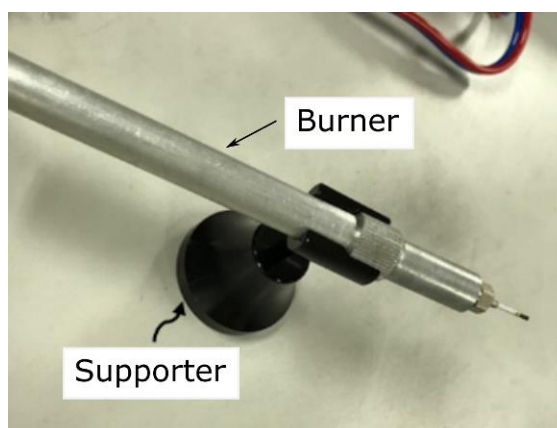
3. Ignite with a lighter. Before opening fuel valve, keep flame of the lighter close to the outlet of the burner. The flame length is set 15 mm by adjusting the fuel valve.

---
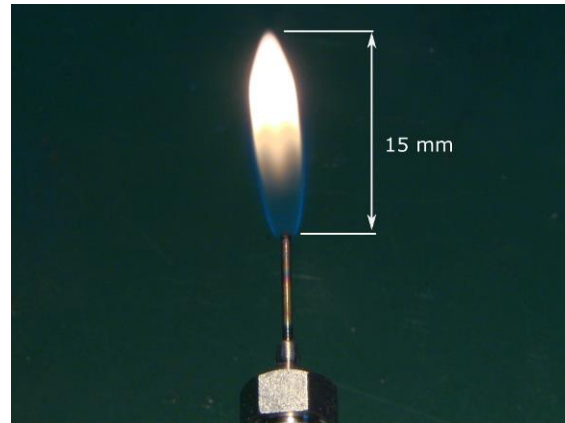
4. Open the oxidizer valve gradually to form premixed flame．This photo shows suitable flame. If oxidizer is supplied too much or too less, the flame temperature is too low to weld wires.

---

5. Stop gases supply after welding. When gases are stopped, the oxidizer valve must be closed at first to prevent back fire. Finally close the fuel valve.
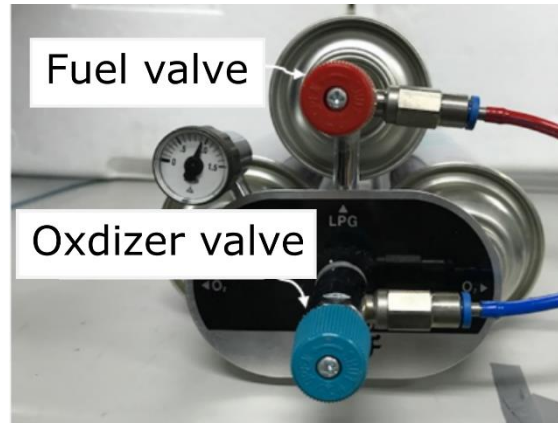
Welding thermocouple wires

1. Prepare wires of a thermocouple.

    Do not cut wires with desired length from the rolls of wire material. Just draw
    wires with length enough to handle them easily.

2. Pinch wires by each hand.

    The length of the wire is 15 – 25 mm from the pinching finger. Make wires
    straightened as possible as you can.
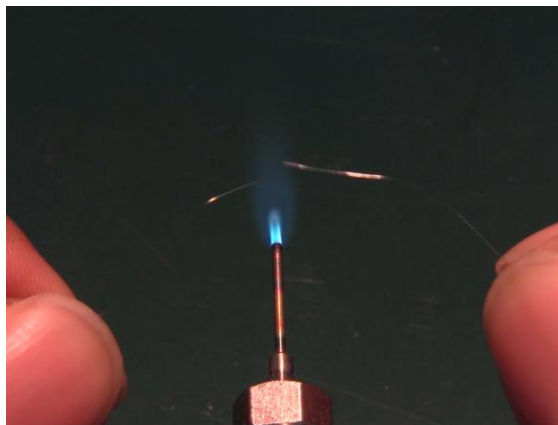
3. Weld wires by flame.

   Keep two ends of wires crossed. The crossing point is put 4 mm above the surface of inner cone and the same height as the tip of inner cone. From the position the crossing point is moved toward the flame surface by 2 mm above to weld wires and make a junction. And then the crossing point is returned to starting position. In case of welding 0.1 mm wires, for example, the time is about 0.8 seconds to finish the process.

   Tips: Pull both wires a little to avoid enlarging the junction spherically.
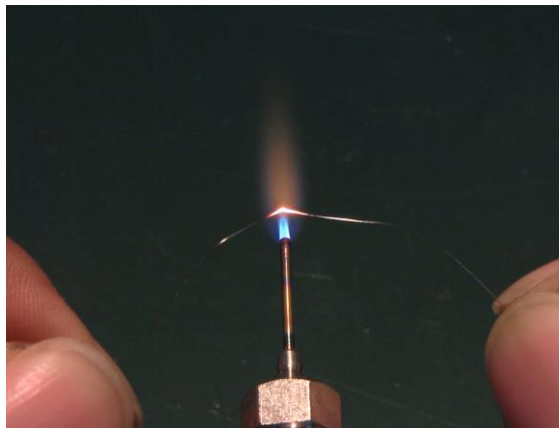
   Tips: Excess length of the wire have to be within 0.5 mm when wires crossing.
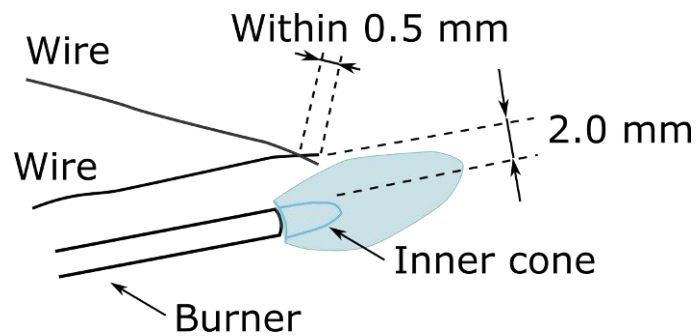
The crossing point of wires is moved 2 mm above the inner cone surface when welding the junction. From 4 mm to 2 mm the crossing point is moved, and then the point is moved 4 mm away from the flame surface again within 0.8 seconds (in welding wires of 0.1 mm in diameter).
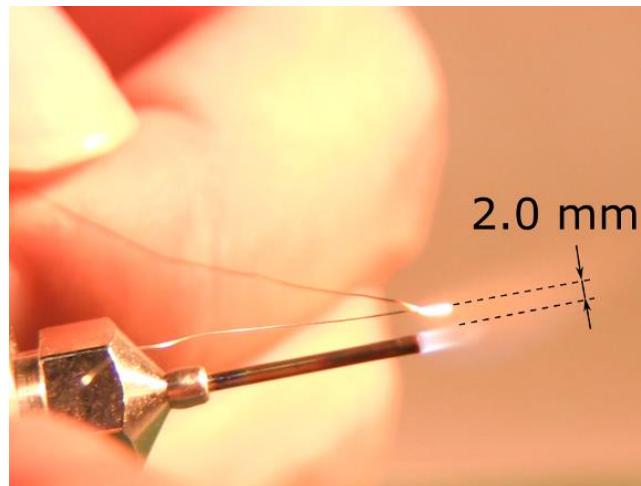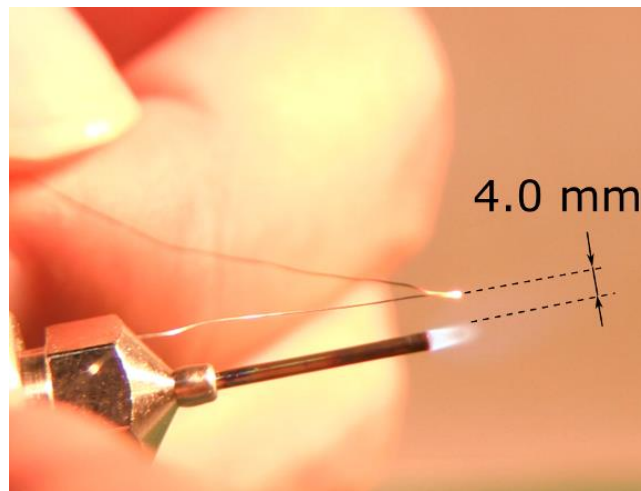
4. Confirm whether the junction is successful or not.

   Pull wires softly to check successful welding.
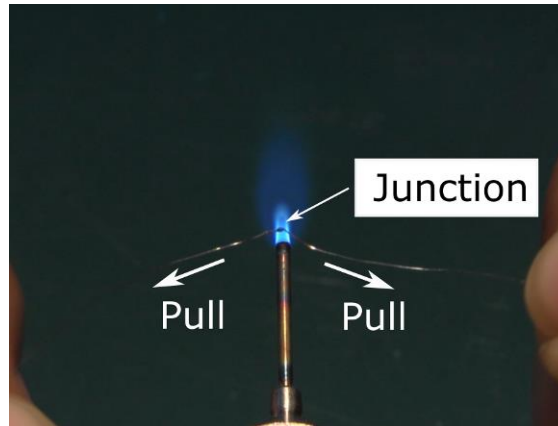
5. In case of failure to weld, tips of wires are burnt out. So, adjust the length of pinching wire

   Cut off the end of wire if spherical tip is formed.
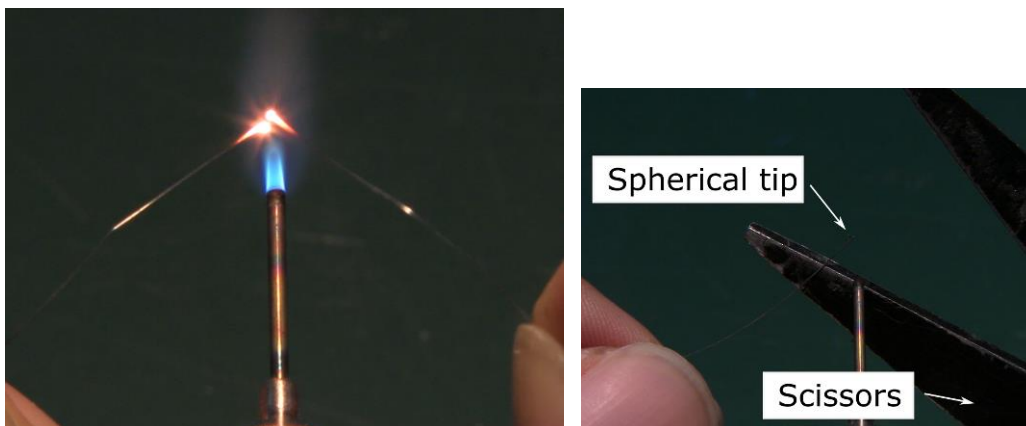
6. Cut wires with desired length from the roll of wire.

It is difficult to judge which wire is positive terminal (or negative terminal). It is recommended that marking label is stuck on the wire of positive terminal.
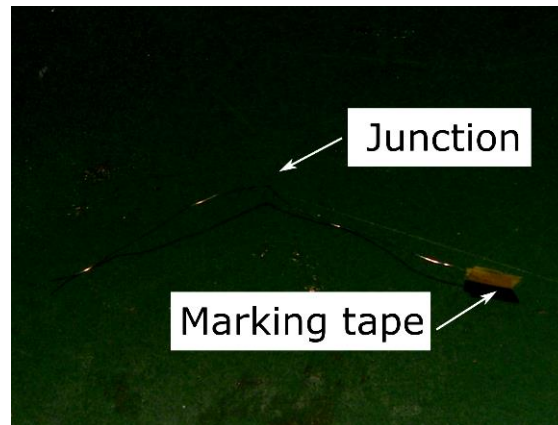
C4 Welding with electronic spark
The electronic spark tools

In this manual, Metronix BPA-351 Bipolar Power Supply is used as a DC power supply. Aluminum plate is connected with negative terminal of the power supply, and a pencil is connected with positive terminal of it. The configuration of the electronic spark tools is shown in Fig.B9. The schematic diagram of the electronic circuit is shown in Fig.B10. In electronic spark tools it is a capacitor in the filter circuit that plays an important role for electronic spark. For electronic spark electric charge stored in the capacitor is discharged when the pencil gets adjacent to the aluminum plate. Thus, the minimum and essential circuit is that in Fig.B11 for electronic spark to weld.
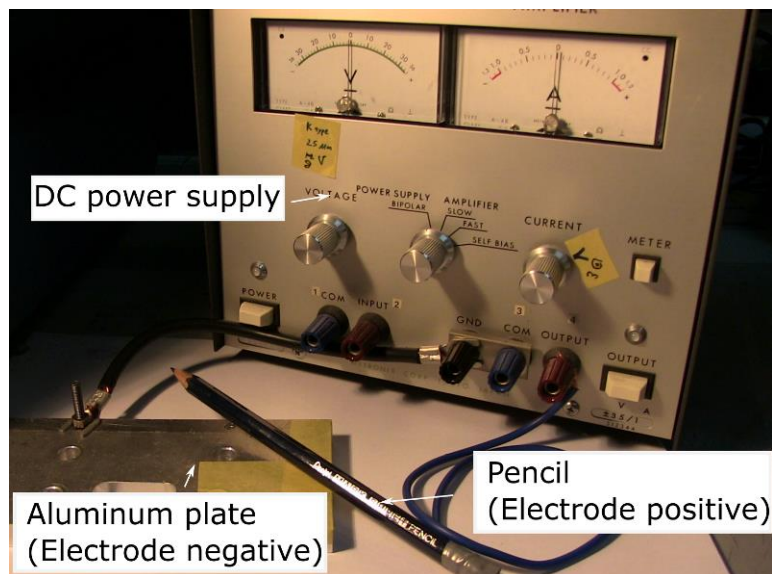
Fig.B9 Configuration of the electronic spark tools.
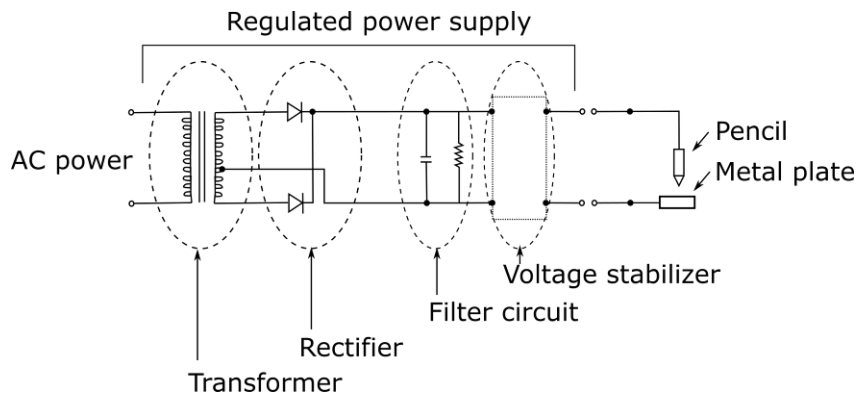
Fig.B10 Schematic electrical diagram of the electronic spark tool.
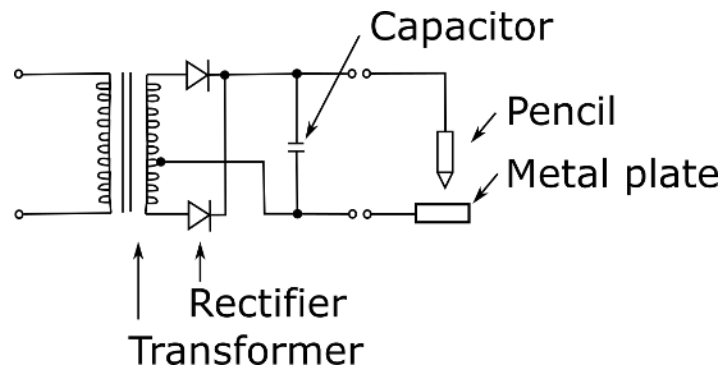
Fig.B11 Simpler electrical circuit for the electronic spark tool.

Welding thermocouple wires

1. Prepare wires of a thermocouple.

    Do not cut wires with desired length from roll, just draw wires with length enough

    to handle these easily.

2. Set wires on the base plate of aluminum.

    Wires are fixed like the right photo as these wires touching on the base plate is less

    than 10 mm in length. In order to insulate a part of wires a masking tape is used.
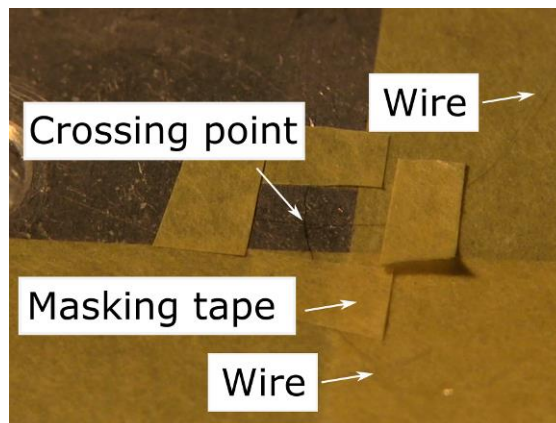
3.   Sharpen the tip of the pensile to spark stably.

The sharpened tip can spark controllably to crossing wires.
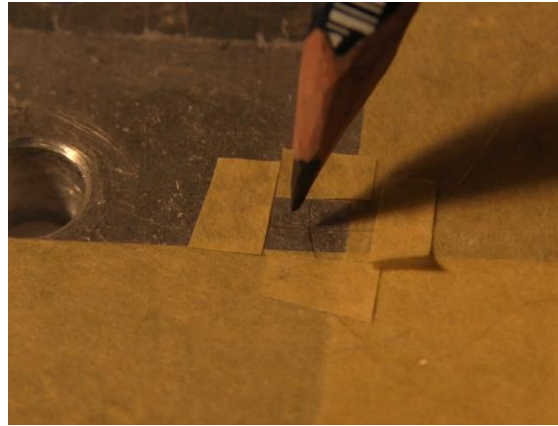
4. Weld wires by the electronic spark.

    The voltage of the DC power supply is set to 9 V. The tip of the pencil is moved to
    crossing point of wires slowly and vertically. The upper wire is pushed to the lower
    wire by the tips. The wire is glowing when the electronic spark occurs
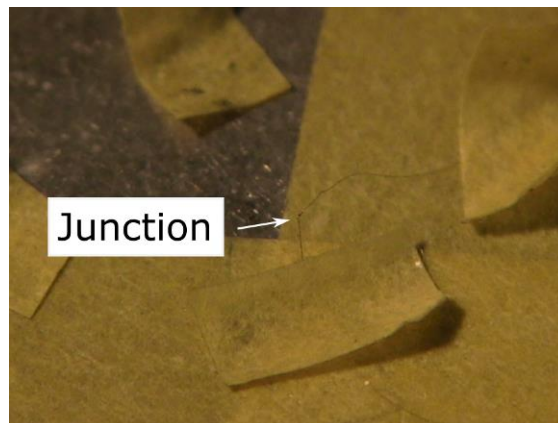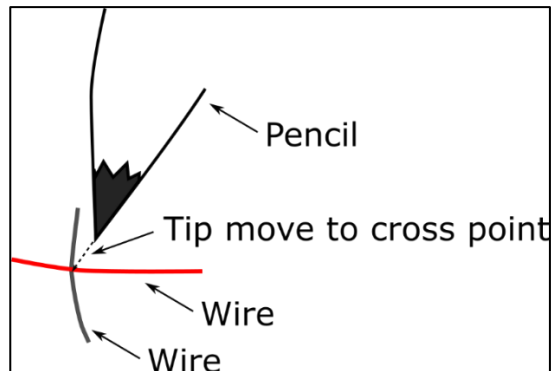
5. Adjust voltage in the case of failure to weld.

   The voltage is needed to decrease 1 V when the electronic spark does not occur or wires are not welded well. The voltage is needed to increase 1 V when wires are busted or burnt out.
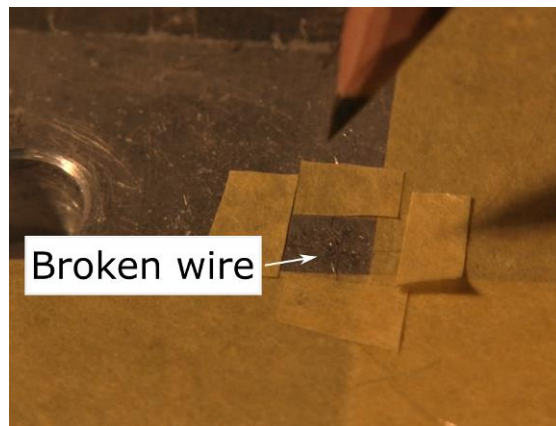
6. Cut off the excess of wires near the junction. And then Cut wires with desired length from the roll of wire.

   It is recommended that marking label is stuck on the wire of positive terminal.
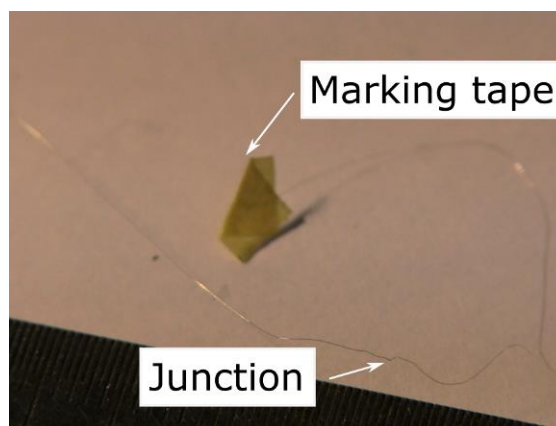
Confirmation of a thermocouple

Confirm whether a thermocouple works or not by following procedure.

1. Confirm electronic conductivity of a thermocouple by a digital tester.

    Even though the junction seems successful, sometimes it fails to be welded due to containing oxide film or weld defects. To check electronic conductivity, measure resistance of the thermocouple by a digital tester.

2. Confirm shape of the junction.

Observe the junction shape by using a microscope. In the way of welding with a micro burner, the junction shape is spherical. The size of the junction should be within three times of wire diameter. The more similar the size is to wire diameter, the more suitable the size is for accurate temperature measurement. The junction shape is needed to remake in which there is excess wire or the size is too large. In the way of welding with electronic spark, a little excess of wire on the junction can be ignored if the case for measuring temperature is not extreme one (the excess length is about 2 or 3 times of wire diameter). In fact it is so difficult to make perfect junction shape in use of small wires less than 25µm.
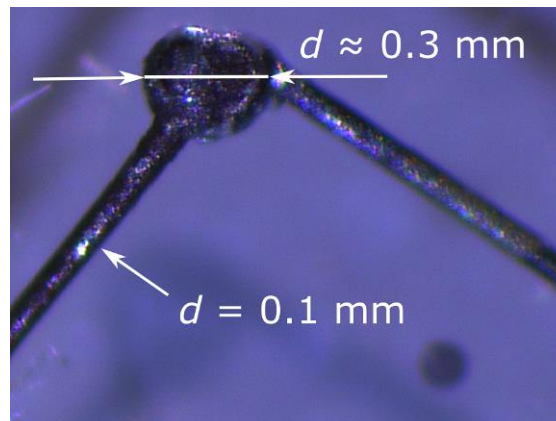
Good junction

Bad junction
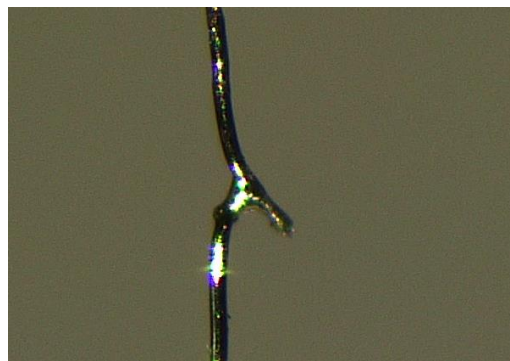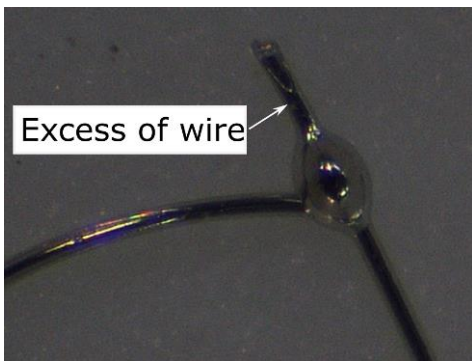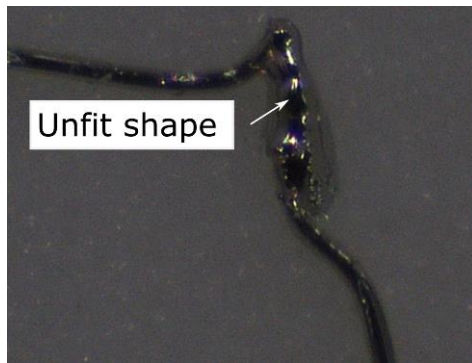
3. Confirm measuring temperature.

The thermocouple is connected with a data logger with copper wire or extension wire. In this manual Graphtech GL900 is used as a data logger. Check whether the displayed temperature increases or not, when flame of a lighter or a small burner is approached near the junction of the thermocouple.
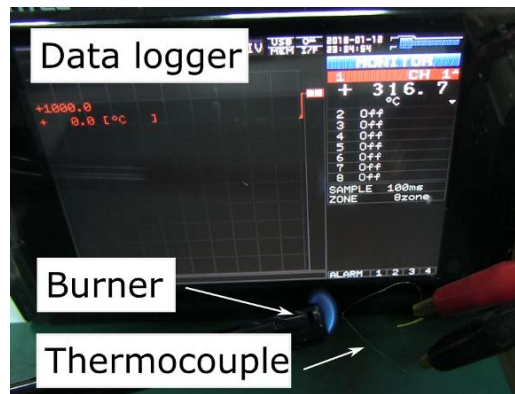
Caution：

  The data logger shows negative temperature when the wires of thermocouple is connected with opposite terminals. If the displayed temperature does not change while flame approached near the junction, it is expected that connection failure occurs or both of wire materials are the same.
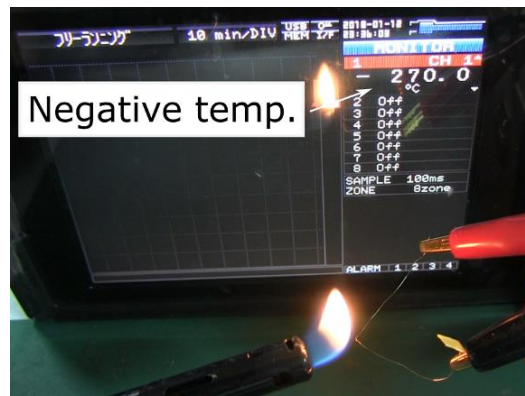
B5 Coating for R, S and B types
Purpose of coating

R type thermocouples are often used in combustion experiments. The range of flame temperature is generally from 700 °C to 1700 °C. Thus, the catalytic effect influences on measuring accurate temperature because materials of a R type thermocouple are platinum and platinum alloy. To prevent the catalytic effect SiO_2 coating is needed. [B6]

Coating method by SiO₂

An alcohol burner is used to coat the R type thermocouple with SiO_2. The fuel is a solution made by mixing ethanol (C_2H_5OH) and Hexamethyldislioxane ($C_6H_{18}OSi_2$), its ratio is 9 to 1. SiO_2 is produced by burning the vapor of that solution. The thermocouple is put near the flame for a few minutes and then SiO_2 coating results from the chemical vapor deposition. The procedures for coating are folloings.

Procedure
1. Burn the solution with an alcohol burner.

2. Set the thermocouple on tips of tweezers with a tape.
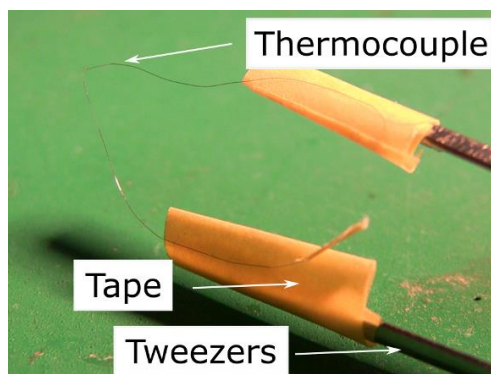
3. Set the thermocouple above the surface of the flame.

The setting position is 10 – 20 mm in height from end of the alcohol burner and 2 – 3 mm above the surface of the blue flame. The surface position of flame may fluctuate by external disturbance. Therefore, the distance between the thermocouple and the flame surface is kept constant (2 – 3 mm) by moving the alcohol burner. The coating time is 5 – 8 minutes.
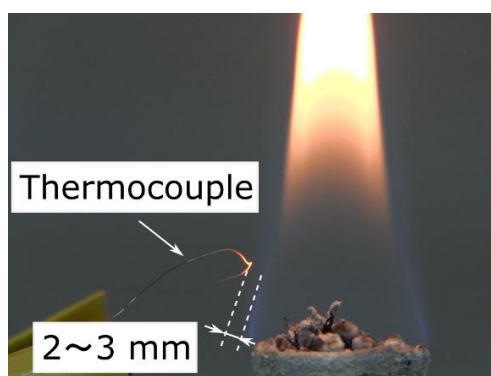
4. Turn over the thermocouple to coat the opposite surface at the same position and for the same time.
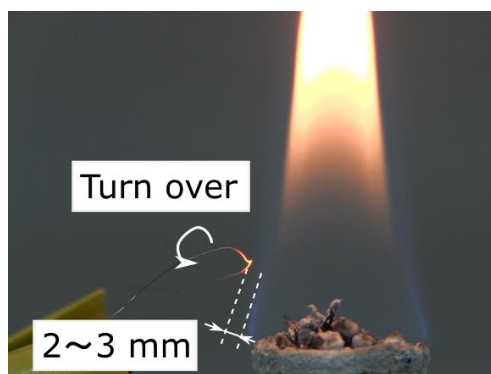
5. Confirm whether the thermocouple is coated with SiO_2 correctly.

    To check the coating, flame temperature is measured with thermocouples with or without coating. The measurement should be done at the highest temperature on flame. It is not in the blue flame but slightly above the flame that the highest flame temperature is. The blue region in flame means that many chemical species, for example CH, OH and so on, is produced.
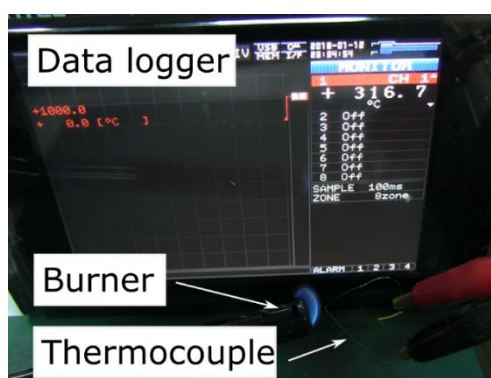
Reference

[B1]   Keyence, "Fundamentals of thermocouples", (Accessed on October 16, 2017) https://www.keyence.co.jp/ss/products/recorder/lab/thermometry/thermocouple.jsp

[B2]   RKC Instrument Inc., "Tips of thermocouples 1", (Accessed on January 19, 2018) http://www.rkcinst.co.jp/yougo/tc.htm

[B3]   RKC Instrument Inc., "Explanation about tips of thermocouples 1", (Accessed on January 19, 2018) http://www.rkcinst.co.jp/techno/18/techno_18.htm

[B4]   Kyoden, "Selection for extension wires" (Accessed on October 16, 2017) http://www.kyouden.co.jp/sub14/hosyou-sentei.htm

[B5]   Shinfuji Burner Co., "O2 Torch OT-3000", (Accessed on October 16, 2017) http://www.shinfuji.co.jp/sfb/products/ot-3000/

[B6]   R.M. Fristrom, Flame Structure and Processes, Oxford Univ Press on Demand, Oxford, 1995, p.510.

[B7]   Kim Lewis, "Thermocouple Laws", SCIENCING, April 24, 2017, (Accessed on January 22, 2018) https://sciencing.com/thermocouple-laws-5517216.html

[B8]   REOTEMP Instrument Corporation, "Types of Thermocouples", (Accessed on January 22, 2018) https://www.thermocoupleinfo.com/

[B9]   THERMOMETRICS, "TYPE K THERMOCOUPLE", (Accessed on January 22, 2018) http://www.thermometricscorp.com/thertypk.html